Computer simulations of core-softened attractive disks: Phase behaviour and inverse melting

by

©Ahmad Mustafa Almudallal

A thesis submitted to the School of Graduate Studies in partial fulfillment of the requirements for the degree of

PhD

Department of Physics and Physical Oceanography
Memorial University of Newfoundland

Memorial University of Newfoundland

May 2014

ST. JOHN'S NEWFOUNDLAND

Abstract

We use several Monte Carlo computer (MC) simulation techniques to calculate the phase diagram of a system of hard disks interacting through a discrete square-shoulder square-well potential. The phase diagram shows the gas, liquid and five crystal phases, and we find that all the melting lines are first-order phase transitions, despite the system being two dimensional. The melting line of the square crystal exhibits a temperature maximum, meaning that above a certain pressure P the density of liquid becomes higher than that of a crystal. The same melting line also exhibits a pressure maximum that implies inverse melting, meaning that at constant pressure the liquid crystallizes by heating.

To increase the range of pressure over which inverse melting occurs, we vary the potential parameters systematically and determine that the extent of the shoulder is the parameter that has the greatest impact. We calculate the new melting curve for the new potential parameter set, and we check the accuracy of the calculations by several methods including the calculation of the Gibbs free energy as a function of density at conditions of constant P and temperature T. The melting transition is first order and to a liquid rather than to a hexatic or to a quasicrystal.

Finally, we perform MC simulations at constant P, T and number of particles N, to study the high pressure phase behaviour of a model with parameters that produce pronounced inverse melting. We detect three fascinating behaviours. First,

the high pressure triple point present in the original model disappears, leaving behind a "liquid corridor" in the phase diagram for which the liquid appears to retain its position as the thermodynamically stable phase down to low temperature. However we find a new crystal that likely usurps the liquid as the stable phase. Second, we find a particular state point, which we name the "funny point", at which the free energy barrier between the liquid and the high density triangular crystal vanishes along their coexistence line. Although the explanation of this funny point remains a mystery, it appears to be connected to the third discovery: a transition between low and high temperature forms of the high density triangular crystal.

The potential studied in this thesis was previously developed to help understand anomalous behaviour in systems such as water and liquid metals. Moreover similar potentials have been used to model lipids interacting within bilayer membranes. Thus, it is possible that some of the phenomenology we observe for the model is relevant in these or related real systems.

Co-Authorship

The thesis author (Ahmad M. Almudallal) was the main contributor to all of the proceeding manuscripts, sharing authorship with Dr. Ivan Saika-Voivod, the supervisor for this graduate project, and Dr. Sergey V. Buldyrev from Yeshiva University. This work resulted in two manuscripts and an on-going work: one entitled *Phase diagram of a two-dimensional system with anomalous liquid properties* published in the Journal of Chemical Physics, another entitled *Inverse melting in a two-dimensional off-lattice model* published in the same journal, and the third work entitled *High-pressure phases in a system with inverse melting*. In all three works, Dr. Saika-Voivod assisted with checking the computer codes, analyzing data and writing the manuscripts. Dr. Buldyrev initially suggested studying the particular model and provided his computer code for event-driven simulations. He produced some of the event-driven data reported in Ch. 4 (the data that is described only in the text, and not represented in a figure). Additionally, he provided feedback on drafts of manuscripts. As a main contributor, Ahmad M. Almudallal wrote the Monte Carlo code, performed 90% or more of the calculations, carried out literature reviews and wrote first drafts of the manuscripts.

Acknowledgements

First of all, I would like to express my thankfulness and appreciation from the deep of my heart to my parents, Mustafa Almudallal and Amneh Almashny for their unconditional help and support. I wish I could show them how much I love them and how much I appreciate what they have done for me. Besides my parents, I would like to thank my brothers and my sister for their continuous assistance and encouragement.

A very special thanks to my supervisor Dr. Ivan Saika-Voivod for his support, patience, motivation, enthusiasm and advice during my PhD program. I sincerely wish I could find better words to express my deep appreciation to him; a huge "thank you".

My sincere thanks to my supervisory committee, Dr. Anand Yethiraj and Dr. Martin Plumer, for their comments and suggestions during the supervisory committee meetings and for critically reading my thesis. I am grateful to Dr. John Whitehead for teaching me the course on phase transitions, which provided much of the theoretical background needed for my research. I would also like to acknowledge Dr. Sergey Buldyrev for his collaboration during my PhD program.

I would also like to thank my best friends ever Dr. Suliman Barhoum, Awab Hamodat, Rabie Matarneh, Wisam AlObaidy, Kassem Abu-Chehade, Bassel Al-Kadour, Pasha Majidi and Hashem Abu-Shahrour for their help and support on educational and personal levels.

I would also like to thank my research group fellows, Mohammad Hasan Khatami, Shahrazad Malek, Payam Bagheri and his wife Leila, Somayeh Khajehpour Tadavani, Swomitra Palit, Edward Hayden, and Suhad Sbeih for their collective encouragement and advice. I would also like to thank Jason Mercer and Martin Leblanc for helping me in writing my computer codes and scripts.

Thanks also to the Department of Physics and Physical Oceanography and Memorial University of Newfoundland for giving me all the chances and experiences that I need to establish my future.

Twenty five continuous years passed of being a student. Finally, I am not a student anymore.

Table of Contents

Abstract **ii**

Co-Authorship **iv**

Acknowledgments **v**

Table of Contents **x**

List of Tables **xi**

List of Figures **xiv**

1 Introduction **1**

1.1 The Model 1

1.2 Computer Simulation 7

1.2.1 Computer Simulation: applications and motivations 9

1.3 Some Considerations for Phase Transitions 10

1.3.1 Preliminaries from Statistical Mechanics 10

1.3.2 Radial Distribution Function 12

1.3.3 Structure Factor 14

1.3.4 Identification of Crystal-like and Liquid-like Particles 15

1.3.5 Melting in 2D Systems 16

1.3.6 Translational Correlation Function 17
1.3.7 Orientational Correlation Function 18
1.4 Outline 19
Bibliography 20

2 Methodology **26**
2.1 Basics of Monte Carlo Method 26
2.1.1 Reduced Units 26
2.1.2 Periodic Boundary Conditions 27
2.1.3 Minimum Image Convention 30
2.1.4 Potential Truncation 32
2.1.5 Metropolis MC 34
2.2 Free Energy Techniques 37
2.2.1 Thermodynamic Integration 37
2.2.2 Frenkel-Ladd Method 38
2.2.3 Gibbs Ensemble 41
2.2.4 Gibbs-Duhem Integration 43
2.2.5 Hamiltonian Gibbs-Duhem Integration 44
2.2.6 Umbrella Sampling 46
Bibliography 48

3 Phase diagram of a two-dimensional system with anomalous liquid properties **50**
3.1 Abstract 50
3.2 Introduction 51
3.3 Methods 54
3.3.1 Model and simulations 54

3.3.2 Solid-liquid and solid-solid coexistence 55
3.3.3 L-HDT coexistence 64
3.3.4 G-L coexistence 67
3.4 Results 69
3.5 Discussion 75
3.6 Conclusions 78
Bibliography 79

4 Inverse melting in a two-dimensional off-lattice model 85
4.1 Abstract 85
4.2 Introduction 86
4.3 Methods 89
4.3.1 Model and simulations 89
4.3.2 Square crystal-liquid coexistence 92
4.3.3 Hamiltonian Gibbs-Duhem integration 96
4.3.4 Biased Monte Carlo simulations 98
4.3.5 Analysis of long range correlations 99
4.4 Results 101
4.4.1 Expanding the range in inverse melting 101
4.4.2 Interfacial tension between S and L 103
4.4.3 Direct simulation of freezing and melting 107
4.4.4 Ruling out hexatic and quasicrystal phases 112
4.5 Discussion and conclusions 116
Bibliography 119

5 High-Pressure Phases in a System with Inverse Melting 125
5.1 Abstract 125

5.2 Introduction 126
5.3 Results and Discussion 127
5.3.1 New phase diagram 127
5.3.2 The liquid corridor 129
5.3.3 The two HDT phases 131
5.3.4 Solving the riddles partially 139
5.4 Discussion and Conclusions 144
Bibliography 147

6 Summary and Future Work **148**
Bibliography 153

List of Tables

1.1 Thermodynamic quantities extracted from the partition function given in Eq. 1.1 [50]. 11

2.1 Reduced units of some physical and thermodynamic quantities. 27

List of Figures

1.1 Single and double minima pair potentials. 4

1.2 Square-shoulder square-well potential. 4

1.3 Square and low-density triangular crystals. 6

1.4 The $P-T$ phase diagram for the SSSW model as depicted from Ref. [37]. 6

2.1 An example of a 2D boundary system as adapted from [1]. 28

2.2 The minimum image convention for a 2D system, as adapted from [1]. 31

3.1 Square-shoulder square-well potential. 52

3.2 Illustration of the phases modelled for the SSSW potential. 56

3.3 Equations of state of the liquid and S crystal at $k_BT/\epsilon = 0.55$ 58

3.4 The mean-squared displacement as a function of coupling parameter λ. 60

3.5 Determination of a coexistence P between the L and S phases at $k_BT/\epsilon = 0.55$ 62

3.6 Snapshot configuration obtained from an NVT simulation for 10,000 particles at $k_BT/\epsilon = 0.55$ 63

3.7 Enthalpy per particle for the liquid and LDT crystal along $P\sigma^2/\epsilon = 0.05$, and chemical potential difference between the L and LDT phases. 65

3.8 Sample time series of the density near the L-HDT coexistence curve. . 66

3.9 Conditional Gibbs free energy as a function of ρ. 67

3.10 Phase diagram of the 2D SSSW model in the P-T plane. 70
3.11 Phase diagram of the 2D SSSW model in the ρ-T plane. 71
3.12 P-T phase diagram at high pressure, near the L-S-HDT triple point. . 72
3.13 Comparison of our phase diagram with previously reported system properties. 75

4.1 Square-shoulder square-well potential. 90
4.2 Phase diagram of the 2D SSSW model in the $P - T$ plane. 91
4.3 The absolute value of the integrand $(h_{HD}(T) - h(T))$. 93
4.4 Differences in the thermodynamic quantities: chemical potential, entropy, enthalpy and potential energy, between L and S phases. 95
4.5 The slope M between two S-L coexistence points as a function of potential parameters. 102
4.6 The S-L coexistence curve for b/σ ranges from 1.40 to 1.50 in P-T and ρ-T planes. 104
4.7 Conditional Gibbs free energy as a function of ρ at $k_BT/\epsilon = 0.340345$. 105
4.8 Snapshot of configurations taken from different windows of umbrella sampling for $N = 2082$ particles. 106
4.9 Close-up of the S-L melting line near inverse melting and state of points to show the range of metastability. 108
4.10 Density as a function of time from EDMD simulations at $P\sigma^2/\epsilon = 5.6$. 109
4.11 Snapshot configurations from EDMD simulations. 111
4.12 Orientational and translational correlation functions as well as the peaks of pair correlation function for the N = 65536. 113
4.13 Structure factors for the $N = 65536$ system at $P\sigma^2/\epsilon = 5.6$. 116

5.1 Panel (a) shows the P-T phase diagram for the original SSSW model with $b = \sqrt{2}$, while panels (b) and (c) show the phase diagram for the $b = 1.46\sigma$ model in the P-T and ρ-T planes. 128

5.2 A snapshot configuration of the liquid phase taken at $k_BT/\epsilon = 0.30$ and $P\sigma^2/\epsilon = 4.60$. 130

5.3 Panels (a) and (b) show ideal configurations of the I and O crystals. Panel (c) shows the phase diagram presented in Fig. 5.1(b) with symbols indicating the extent of metastability of each. 132

5.4 Evidence for a transition between high and low T forms of HDT. . . . 133

5.5 Snapshots configurations taken along the isobar $P\sigma^2/\epsilon = 9.8$. 135

5.6 Pair distribution and orientational correlation functions to study structural differences between the configurations presented in Fig. 5.5. . . 136

5.7 Tests for a second order transition from the specific heat (C_p) 138

5.8 Binder cumulants indicates a first-order transition between low-T and high-T forms of HDT. 139

5.9 MC simulations with anisotropic pressure control showing abrupt change in the potential energy per particle indicating a first-order transition. 141

5.10 The candidate structure for the low-T HDT crystal that has potential energy per particle -2.5ϵ 142

5.11 Conditional Gibbs free energy as a function of ρ obtained from umbrella sampling MC simulations along the HDT-L coexistence line. At $k_BT/\epsilon = 0.50$ a barrier is not distinguished from the noise. 143

Chapter 1

Introduction

1.1 The Model

In this thesis, we study the phase behaviour of a system of particles interacting through a square-shoulder square-well interaction potential (SSSW). This interaction belongs to the family of so-called core-softened (CS) potentials, which mainly consist of a hard core at short separation and a penetrable core at larger separation. The motivation of using CS potentials arises from the desire of having a simple isotropic (radially symmetric) potential that is able to describe complicated features of systems with anisotropic interactions, e.g., those with an angular dependence. This can be understood from the example of water, where orientation-dependent hydrogen bonds introduce a favoured interaction at a particular separation between molecules but orienting the molecules differently allows them to interpenetrate. The history of these deceptively simple potentials goes back to the 1970s. The first use of a CS potential was by Stell, Hemmer and co-workers in a lattice gas system to study the isostructural solid-solid phase transition that ends in a (second) critical point [1–3], which was reported previously in some experimental studies, see for example [4]. CS po-

tentials were also used in liquid metal systems [5–12] to explain the deviation of the structure factor from simpler central force models such as those with a pair interaction potential that varies as $u(r) \sim r^{-4}$. In the 1990s, CS potentials were used to study liquid anomalies, such as density, diffusion, and entropy anomalies for water, in 1D [13–15], 2D [16–19] and 3D [16,17,20]. Stillinger *et. al.* used a statistical mechanical perturbation theory to show that a CS potential can be considered as a realistic first-order approximation for the real interaction between water molecules resulting from averaging over relative orientations [21,22], i.e., that the anisotropic interaction of water molecules can by approximated by a simpler isotropic interaction.

Pioneering experimental work on compressed water at very low temperature reported a first order-like transition from low density amorphous ice (LDA) to a higher density amorphous one (HDA) [23]. One possible explanation for this behaviour of the glassy state of water is an underlying first-order transition between two liquids differing in density that is obscured by glassy dynamics. Indeed, a simulation study for the ST2 model of water [24] (a five-site model where charges representing protons and lone electron pairs are placed tetrahedrally around an oxygen atom) suggested that the anomalies in stable and supercooled water are caused by a second critical point at temperature (T'_C) [25], and that this critical point terminates the transition between two metastable liquids, HDL and LDL [26, 27]. Above T'_C, HDL and LDL become indistinguishable in an analogous way to what happens to the liquid and gas above their critical temperature (T_C). Proposing T'_C in the supercooled liquid was the starting point for a new research area focusing on the transition between two liquids of different densities in a single component system. Some of these studies used the two-liquid model to explain the liquid-liquid (L-L) transition [28–30]. According to this model the liquid is considered to be a mixture of two different liquids in which the concentration is altered by changing some external parameters such as temperature

or pressure.

Mishima and Stanley suggested that CS potentials can explain the L-L transition in the supercooled liquid [31]. To explain the relationship between CS and L-L phase transition, we follow the discussion presented in Ref. [31]. The minimum in the generic potential shown in Fig. 1.1(a) is necessary to have a critical point, where at low temperature (T), and relatively high pressure (P), the system will be influenced by the potential minimum, and therefore molecules will condense to form a liquid. At high T, the kinetic energy is large and the system will not be influenced by the potential minimum, giving rise to a gas.

Suppose now that the potential minimum changes to have a deeper narrow outer well and a shallower inner well as in Fig. 1.1(b). This two-minima potential is responsible for the occurrence of the second critical point at low temperature. At high T, the kinetic energy is large enough so that the two minima do not influence the system. At low temperature $T < T'_C$ and comparatively low pressure, the system explores the outer well, and a low density liquid (LDL) forms. At higher pressure, the system probes the inner well and a high density liquid (HDL) forms. According to this picture, there is a L-L phase transition that occurs at low T between the HDL and LDL phases.

A few years later, Franzese *et. al.* used three-dimensional MD simulations with a more simplified, shoulder like potential, with two characteristic distances (hard-core and soft-core). They showed that such a potential can produce a L-L phase transition, and they located the position of T'_C, but no density anomalies were observed [32]. Another study of a 2D system reproduced the density anomaly, but neither L-L transition nor T'_C were observed [14]. More studies have been done later focusing on density anomalies and L-L transitions. For example. Ryzhov *et. al.* tracked the change of the L-L transition line as a function of the shoulder width in a square-shoulder po-

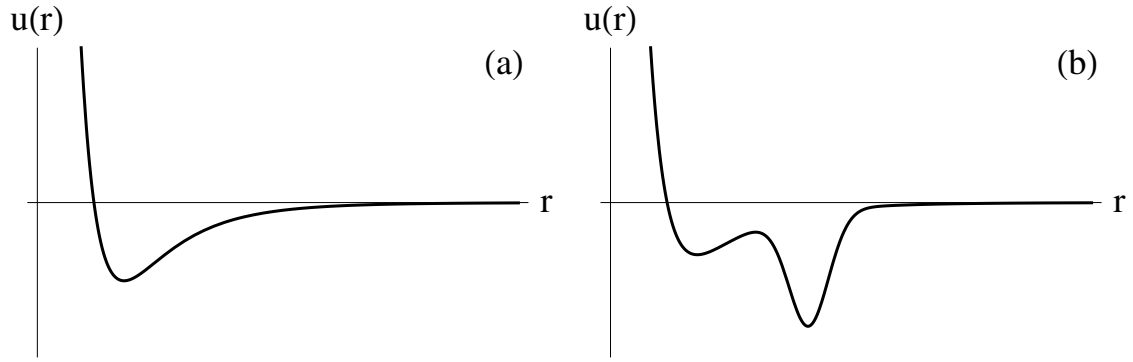

Figure 1.1: Panel (a) shows a single minimum pair potential used to produce the liquid-gas critical potential, while in panel (b), the minimum is modified to contain two sub-wells to allow for the existence of a second critical temperature.

tential [33]. Gibson *et. al.* studied a family of ramp potentials, and they found that T_C' moves systematically from a stable position in the phase diagram to a metastable one [34]. Other studies used lattice models to gain more insight into the mechanism of the L-L transition and associated liquid-state anomalies [35, 36].

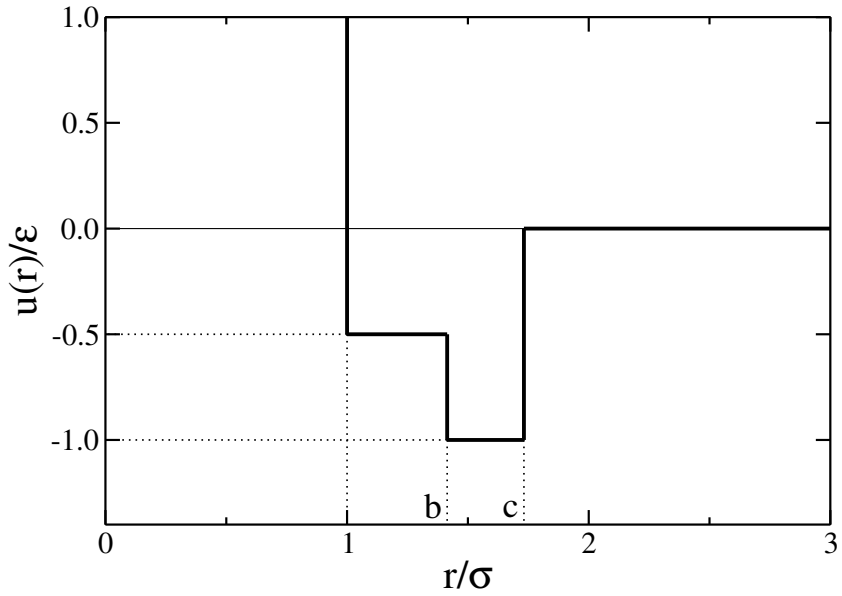

Figure 1.2: A square-shoulder square-well potential with a hard-core diameter σ. $b = \sqrt{2}\sigma$ is the soft-core distance, and $c = \sqrt{3}\sigma$ is the attractive distance limit. r is the distance between two particles and ϵ is the bond energy.

Scala *et. al.* performed MD simulations in 2D of the square-shoulder square-well

(SSSW) model, shown in Fig. 1.2, to test whether a water-inspired CS model can generate liquid anomalies [19, 37]. While the 2D case can be motivated by a desire to understand phenomena at interfaces, in membranes or systems under confinement, it also provides a way of more easily visualizing the structures and processes in the system. It is this potential that is studied in this thesis. In 2D, this potential describes disks with a hard-core diameter σ and an attractive well extending out to a radial distance $c = \sqrt{3}\sigma$. The attractive well itself contains a shoulder, with a pair interaction energy of $-\epsilon/2$ for $\sigma < r < b$ and energy of $-\epsilon$ for $b < r < c$. Making $b = \sqrt{2}\sigma$ allows for the existence of two crystals, a low density triangular (LDT) and a higher density square crystal (S), with the same potential energy per particle of -3ϵ, see Fig. 1.3. This value of b is not unique, but is the smallest value which yields the same crystal energies when the disks are touching. A solid line in the graphs corresponds to an interaction energy of $-\epsilon$ between two particles, while a dashed line corresponds to a -0.5ϵ energy. With these parameters values, the two crystal-like environments based on LDT and S will survive locally in the liquid, providing the basis for the idea for two liquids of different density coexisting.

This study was continued by Buldyrev *et. al.* with the same SSSW model in 2D and 3D to study L-L transitions [37]. For the 2D system, they produced a phase diagram showing liquid anomalies in relation to approximate crystallization lines for a range in P and T near a potential second critical point, as shown in Fig. 1.4.

The phase diagram shows the gas-liquid coexistence line (h) terminated by a critical point (C) at high T, and a hypothetical position of a second critical point (f). This point coincides with the crossing of the two crystallization lines (d and e). These two lines were determined from examining the behaviour of the pressure, structure, and dynamics along isochores. Therefore, they are estimates of the limit of liquid stability, or more technically of metastability, with respect to the square and

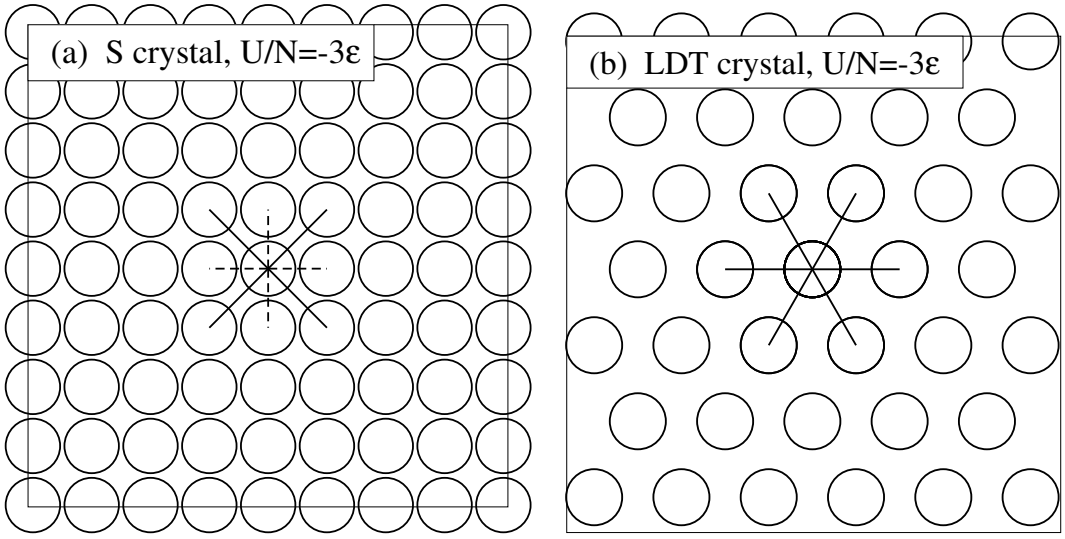

Figure 1.3: Fig. 1.3(a) shows square crystal and Fig. 1.3(b) shows low-density triangular crystal, both with the same energy per particle (-3ϵ), where the solid line is a bond between two particles with energy $-\epsilon$ and the dashed line is a bond with energy -0.5ϵ.

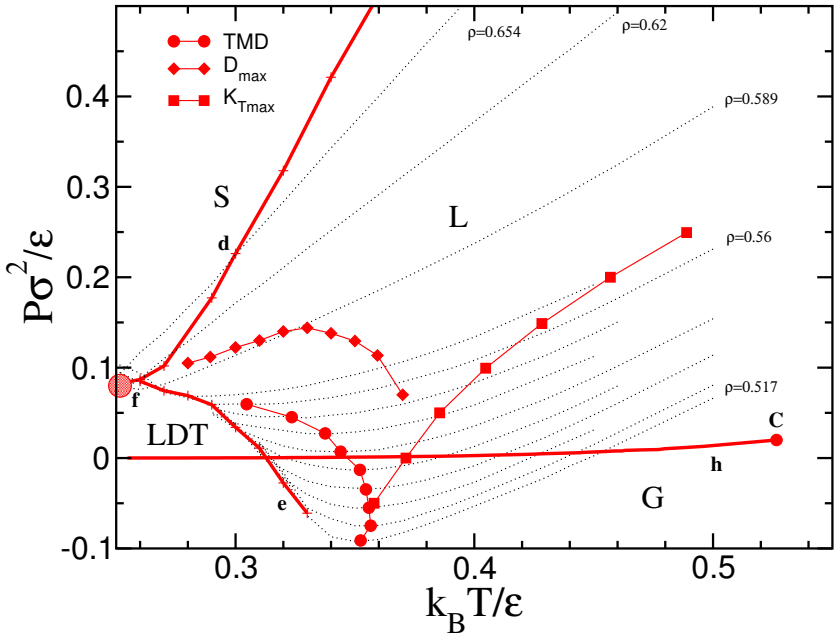

Figure 1.4: The $P-T$ phase diagram for the SSSW model as depicted from Ref. [37]. The h-line is the liquid-gas coexistence curve terminated by a critical point (C). The two thick curves, d and e, are crystallization lines, where their crossing is what thought to be the hypothetical position of a second critical point (f).

triangular crystals [37].

Initially, our motivation to further study this model was to present the whole phase diagram for a wide range of T and P, and report new features or phases that the model might have. This is the work presented in Ch. 3. We find two new low-density crystal phases not previously reported for the model. We find that all the transitions are at least weakly first order. The crystallization lines reported in Ref. [37] are below our calculated melting lines, as ought to be the case. Additionally, the S crystal shows a maximum temperature in its melting curve, as well as a maximum in pressure. Thus, the present model is a useful one for studying the rare phenomenon of inverse melting [38], in which the liquid may freeze to the crystal upon heating, and this is our motivation to do the research reported in Ch. 4.

1.2 Computer Simulation

The history of computer simulation started during and after the Second World War when electronic computing machines performed extensive calculations to help in the development of nuclear weapons [39, 40]. The electronic computing machines were simple and large compared to the machines of today, and using these machines was restricted to the military. In 1952, the electronic computing machines spread to nonmilitary usage to start a new era of research based on computer algorithms. In 1953, Metropolis *et. al.* performed the first computer simulation study at Los Alamos National Laboratory in the United States using the MANIAC computer to study the equation of state of liquids [39–42]. In this first simulation, Metropolis *et. al.* introduced the Monte Carlo (MC) simulation method [41], which later became a primary research technique in many fields of science and engineering. This method was given this name because the calculations are based heavily on the use of pseudo

random numbers generated by the computer. The name connects the dependence of MC on random numbers to one of the great gambling capitals of the world, the city of Monte Carlo [39, 40, 43, 44]. While today MC refers broadly to techniques based on the acceptance and rejection of randomly generated states, we employ in this thesis the original Metropolis algorithm to generate an ensemble of states in the canonical and isothermal-isobaric ensembles of our model.

In early work, MC simulation was only used to study ideal models such as treating molecules as hard spheres [41]. Periodic boundary conditions were introduced in Ref. [41] for the first time, which later became an essential part of simulation when studying bulk materials. A few years later, Wood and Parker carried out computer simulations for the Lennard-Jones potential and they obtained results comparable to experiments for systems such as liquid argon [45].

MC is a powerful technique for obtaining structural and thermal properties of model systems interacting through some potential, but it is not as useful in terms of studying dynamic properties, such as the diffusion coefficient. To address this, Alder and Wainwright developed a new technique, called Molecular Dynamics (MD) simulations. This method is based on solving the classical equations of motion (Newton's equations) for a system of molecules [39, 40, 42]. Within MD, molecule positions and velocities change according to the intermolecular forces between individual molecules. The first MD study was done in 1956 by Alder and Wainwright to study the dynamics of hard spheres [46]. Two years later, Gibson *et al* used MD simulation for the first time to study a more realistic materials problem, radiation damage in crystalline Cu [47]. In 1964, Rahman was the first to use MD simulation for a real liquid (argon) [48]. Although many developments have refined MC and MD simulations since those pioneering times, the same basic ideas are still behind today's simulations of simple fluids, biological molecules and other materials of varying degrees of

complexity [39].

One of the differences between MC and MD simulations is that MC does not depend on generating physically realistic particle trajectories from a consideration of forces, but rather samples configurations in a random way. It thus offers the possibility of reaching equilibrium states in a computationally more efficient manner if an appropriate algorithm can be found. As an example for spin systems, the Wolff algorithm allows for clusters of particles to change their states at once, rather than just particles one at a time, resulting in a faster exploration of system configurations [49].

1.2.1 Computer Simulation: applications and motivations

In our context, computer simulation is a tool whereby a computer program evolves a model of a system according to often simple rules based on how constituents of the system interact. Simulation is necessary when it is difficult to determine otherwise, e.g., through some analytical theory, how the behaviour of the system as a whole emerges from a consideration of the interaction of its parts. Computer simulation has become a useful tool to study many systems in physics, chemistry, biochemistry, biology, drug design, engineering and so on. In physics, a few systems have exact solutions, such as the ideal gas, Einstein crystal and two-dimensional Ising model. Other systems require employing some approximations to make the problem analytically tractable. But most problems in physics can not be solved exactly even after employing reasonable approximations. Often, the behaviour of systems that have many interacting particles is difficult to predict. Therefore, computer simulation is needed to solve problems that involve many particles [39].

For models that are amenable to at least approximate theoretical treatment, computer simulations, which give essentially exact results, provide a check on the accuracy of the theoretical results and can provide a systematic framework for determining the

range of validity of the assumption inherent in the theory. The line of inquiry can then proceed to more "realistic" models, i.e., possibly more complex models that aim to give a more quantitatively accurate description of a physical system. Such models may be more difficult to treat analytically, but just as easy to simulate. Thus, by quantitatively validating the theory for a simpler model and validating finer implementations of the model against experiment, simulation can provide a bridge between theory and experiment.

1.3 Some Considerations for Phase Transitions

1.3.1 Preliminaries from Statistical Mechanics

Statistical mechanics is a branch of physics that uses some mathematical tools for dealing with a large number of particles to study the macroscopic properties of a material. In statistical mechanics, an ensemble is a conceptual collection of many instances of a system, i.e., imaginary copies of a system where the bulk properties of each satisfy certain constraints or follow a specified distribution, while the microscopic arrangement of constituent particles is different. Different types of ensembles are defined by what bulk variables are held fixed. For example, by fixing the number of particles N, the volume V, and the energy E, we define the microcanonical ensemble; fixing N, V, and T, we define the canonical ensemble; and finally, if V, T, and the chemical potential μ are fixed, we are working within the grand canonical ensemble. Each ensemble is associated with a partition function which can be used to extract thermodynamic information about the system. For the canonical ensemble, the partition function $Q(N, V, T)$ is given by [50],

$$Q(N, V, T) = \sum_r \exp(-\beta E_r), \tag{1.1}$$

Internal energy	$U = -\frac{\partial \ln(Q(N,V,T))}{\partial \beta}$
Helmholtz free energy	$A = -k_B T \ln(Q(N,V,T))$
pressure	$P = -\left(\frac{\partial A}{\partial V}\right)_T$
Gibbs free energy	$G = A + PV$
Enthalpy	$H = U + PV$
Entropy	$S = -\left(\frac{\partial A}{\partial T}\right)_V$
Specific heat at constant V	$C_V = \left(\frac{\partial U}{\partial T}\right)_V$
Specific heat at constant P	$C_P = \left(\frac{\partial H}{\partial T}\right)_P$
Isothermal compressibility	$\kappa_T = -\frac{1}{V}\left(\frac{\partial V}{\partial P}\right)_T$

Table 1.1: Thermodynamic quantities extracted from the partition function given in Eq. 1.1 [50].

where the sum is over all microstates with the given V and N, E_r is a microstate energy and $\beta = (k_B T)^{-1}$, where k_B is Boltzmann's constant. Table 1.3.1 shows a list of thermodynamic quantities that can be extracted from the partition function [50,51]. The derivations of these quantities, for the canonical ensemble and other ensembles, are available in most statistical mechanics books, e.g., Ref [50].

Phase transitions occur when we encounter a discontinuity or a singularity in one or more of the thermodynamic functions. Some examples of phase transitions are condensation of gases, evaporation of liquids, melting of solids, crystallization of liquids, super-fluid transition from He I to He II, transition from ferromagnetic to paramagnetic, and transition from normal to superconducting materials [50].

In general, phase transitions come in one of two classes, first-order and continuous. A first order transition exhibits a discontinuity in the first derivative of the free energy with respect to a thermodynamic variable. For example, in boiling a liquid by increasing temperature at fixed pressure, there is a discontinuity in the volume, entropy and energy. Familiar phase changes between solid, liquid, and gas are common

examples of first-order transitions. Such a transition involves latent heat, where the system either absorbs or releases energy at constant temperature. This will drive the system to form coexisting phases before completely transforming to the second phase. Continuous phase transitions exhibit a discontinuity or singularity in higher-order derivatives of the free energy, while all first derivatives are continuous. Transitions with a discontinuous second derivative, such as the divergence of the heat capacity in a ferromagnet, are often termed second order.

In addition to discontinuities in bulk thermodynamic quantities, phase transitions are accompanied by a qualitative change in an order parameter. Broadly speaking, an order parameter is a quantity that vanishes in one phase, i.e., has a value of zero, and has a non-zero value in the other phase. Examples of order parameters include the magnetization in a paramagnetic to ferromagnetic transition and the height of a peak in the structure factor for a structural change in a material.

Various MC simulation algorithms exist to evolve the system from a non-equilibrium state to the equilibrium state under different statistical ensembles. At equilibrium we save many independent configurations, i.e., coordinates of all the particles in the system, to use in calculating quantities that are useful in describing the phase transition of interest. Structural quantities such as the radial distribution function, structure factor, measures of local crystallinity, orientational correlational function and translational correlational function are useful for determining the type of phase and the degree ordering present in the system. The last two quantities are particularly useful when considering transitions in two dimensions.

1.3.2 Radial Distribution Function

The radial distribution function $g(r)$ is defined as the probability of finding a particle at distance r away from a reference particle relative to the probability expected for

a completely random distribution (ideal gas state) at the same density. According to this definition, $g(r)$ will be equal to unity for an ideal gas (strictly speaking, $1-1/N$), and any deviation of $g(r)$ from unity reflects correlations between particles [52]. The formula of $g(r)$ for the canonical ensemble can be determined by integrating the configurational distribution function over the positions of all particles in the system except two [39],

$$g(\vec{r_1}, \vec{r_2}) = \frac{N(N-1)}{\rho^2 Z_{NVT}} \int d\vec{r_3}\ d\vec{r_4}\ ...\ d\vec{r_N} \exp(-\beta\ U(\vec{r_1}, \vec{r_2}, ...\ \vec{r_N})), \tag{1.2}$$

where N is the total number of particles, ρ is the number density, U is the potential energy of the system, and

$$Z_{NVT} = \int d\vec{r_1}\ d\vec{r_2}\ ...\ d\vec{r_N} \exp(-\beta\ U(\vec{r_1}, \vec{r_2}, ...\ \vec{r_N})), \tag{1.3}$$

is the configurational integral (similar to the canonical partition function, except that velocities are not considered). For a system of spherically symmetric interactions, $g(\vec{r_1}, \vec{r_2})$ depends only on the distance between particles $r = |\vec{r_1} - \vec{r_2}|$, and hence the definition in Eq. 1.2 can be expressed as,

$$g(r) = \frac{1}{\rho^2} \left\langle \sum_i \sum_{j \neq i} \delta(\vec{r_i})\ \delta(\vec{r_j} - \vec{r}) \right\rangle = \frac{V}{N^2} \left\langle \sum_i \sum_{j \neq i} \delta(\vec{r} - \vec{r}_{ij}) \right\rangle. \tag{1.4}$$

where $\langle . \rangle$ denote an ensemble average (an average over all possible states), and $\vec{r}_{ij}$ is the displacement vector pointing from particle i to particle j.

The regular distribution of particles in a crystal gives the characteristic pattern of the $g(r)$ with high, sharp peaks. For liquids, $g(r)$ has regions of high and low intensity but no sharp peaks. $g(r)$ can be measured experimentally or calculated by computer simulation to distinguish the liquid from the crystal. It also can be used for

calculating some thermodynamic quantities, such as energy and pressure for a system of interacting particles from the general relation,

$$\langle \mathcal{A} \rangle = \left\langle \sum_i \sum_{j>i} a(r_{ij}) \right\rangle = \frac{1}{2} N\rho \int_0^\infty a(r) g(r) 4\pi r^2 dr, \tag{1.5}$$

where $a(r)$ is a quantity that depends only on the distance between two particles, and $\langle \mathcal{A} \rangle$ is the expectation value of $a(r)$. For example, the total internal energy (potential and kinetic) of the system can be expressed as [39],

$$E = \frac{3}{2} N k_B T + 2\pi N\rho \int_0^\infty r^2 u(r) g(r) dr, \tag{1.6}$$

where $u(r)$ is the pair interaction energy and the first term is the ideal gas contribution. The pressure can be calculated by [39],

$$P = \rho k_B T - \frac{2\pi}{3} \rho^2 \int_0^\infty r^3 \frac{du(r)}{dr} g(r) dr, \tag{1.7}$$

where the integral is related to the average of the pair virial function $r\frac{du(r)}{dr}$.

1.3.3 Structure Factor

The structure factor $S(\vec{q})$ is a quantity that describes how the material scatters incident waves, where the argument $\vec{q}$ is a vector in reciprocal space which is equal to the difference between the scattered and the incident wave vectors. $S(\vec{q})$ is commonly obtained in neutron and X-ray scattering experiments to study the structure of materials. $S(\vec{q})$ is derived by using both Bragg and Laue conditions, and the final formula is [39, 53],

$$S(\vec{q}) = \frac{1}{N} \left\langle \sum_{i,j=1}^{N} \exp(i\vec{q} \cdot (\vec{r_j} - \vec{r_i})) \right\rangle. \tag{1.8}$$

In case of isotropic liquids, the system does not have long range-order and after averaging over directions in Eq. 1.8, the structure factor becomes a function of $q = |\vec{q}|$ rather than $\vec{q}$ [54]. $S(q)$ is directly related to $g(r)$ and it can be obtained simply by taking the Fourier transform of $g(r)$ as in the following for a 2D liquid system [39],

$$S(q) = 1 + 2\pi\rho \int_0^\infty r \frac{\sin kr}{kr} g(r) dr. \tag{1.9}$$

One restriction that must be taken into account when calculating $S(q)$ for a square system with periodic boundaries is that $\vec{q}$ must equal $2\pi(n_x, n_y)/L$, where L is the simulation box length and $n_{x,y}$ are integers [39, 55, 56].

1.3.4 Identification of Crystal-like and Liquid-like Particles

When performing a simulation, the results sometimes show a crystal with some defects or a liquid with some crystalline local environments. Therefore, to distinguish the crystal and liquid phases, it becomes important to identify each particle in the system individually as being in a crystal-like or liquid-like environment. To do so, we follow the approach developed by Frenkel and co-workers [57], based on the local bond-order analysis that was originally introduced in Ref. [58]. According to this method, we calculate a complex quantity q_{lm} for each particle as,

$$q_{lm}(i) = \frac{1}{N_b(i)} \sum_{j=1}^{N_b(i)} Y_{lm}(\hat{r}_{ij}), \tag{1.10}$$

where $N_b(i)$ is the number of neighbours of particle i within a specific distance, and $Y_{lm}(\hat{r}_{ij})$ is the spherical harmonic function calculated for angles defined by the unit vector $\hat{r}_{ij}$ pointing from particle i to neighbour j. The unit vector $\hat{r}_{ij}$ determines the polar angle $\theta_{ij} (\equiv \pi/2$ in 2D) and azimuthal angle ϕ_{ij}. The integer l is chosen to be equal to 4 for crystals with square symmetry and 6 for triangular symmetry, and

the integer m takes values in the range $\in [-l, l]$. We then calculate the correlation between each pair of neighbouring particles i and j as,

$$c_{ij} = \sum_{m=-l}^{l} \hat{q}_{lm}(i)\hat{q}^{*}_{lm}(j), \tag{1.11}$$

where

$$\hat{q}_{lm}(i) = \frac{q_{lm}(i)}{[\sum_{m=-l}^{l} |q_{lm}(i)|^2]^{1/2}}, \tag{1.12}$$

and q^* is the complex conjugate of q. The correlation between two neighbours is high if their bonding environments are aligned. If the correlation between the two neighbours i and j is greater than a threshold value, then the two particles are considered to be connected. A particle i is considered to be a solid-like particle if it has at least three connected particles for the square crystal and five connected particles for the triangular crystal.

1.3.5 Melting in 2D Systems

Crystals in 3D have long range translational order, while crystals in 2D have quasi-long range translational order meaning that the translational order decays as a power law with distance. This is because long wavelength fluctuations in 2D are low in energy, i.e., the energy of a fluctuation does not diverge as its wavelength increases, and therefore it is easy to destroy the long range translational order [59, 60]. The dependence of the translational order on the system dimensionality introduces different scenarios of crystal melting. In 3D systems, melting occurs through a first order phase transition, while for 2D systems, the prevailing thought is that melting occurs continuously and follows KTHNY theory [61, 62] developed in 1970s by Kosterlitz, Thouless, Halperin, Nelson, and Young.

According to this theory, bound pairs of dislocations appearing spontaneously

in the crystal near melting undergo unbinding at the melting transition. The unbinding of dislocations produces the hexatic phase, for which translational order is reduced from quasi-long-range to short range (decaying exponentially with distance) and reduces long range orientational order to quasi-long range [55, 56, 60]. Further disordering, e.g., by heating or decompression, results in the unbinding of the two particles identified with a single dislocation to form disclinations. This produces the liquid, which is characterized by short range orientational and translational order. Thus, KTHNY-theory predicts three distinct equilibrium phases in 2D: crystal, liquid and hexatic, each with its own characteristics. The transitions from crystal to hexatic and then from hexatic to liquid are both continuous transitions, which means the two phases do not coexist under any condition.

Several experimental and computer simulation studies validated KTHNY theory, see for example Ref. [63–65]. In contrast, a recent study of hard disks showed that the transition between the liquid and the hexatic phase is a first order transition [66]. In our work in Ref. [67], we see that melting in the 2D SSSW model is consistent with a conventional first order transition. This picture of the 2D transition was also reported in other studies as in Refs. [68–71]. In Ch. 4 we perturb the SSSW model by changing the potential parameters to increase the range of inverse melting, and we find that melting remains first order, at least for the square crystal near the region of inverse melting.

1.3.6 Translational Correlation Function

In 2D, fluctuations with long wavelength destroy the long range translational order of the crystal [60, 72]. The usual measure of translational correlation within KTHNY

theory is the correlation function defined as [55, 60, 73, 74],

$$G_{\vec{g}}(r) = \left\langle \sum_j \exp(i\vec{g} \cdot \vec{r}_j)) \right\rangle, \tag{1.13}$$

where $\vec{g}$ is a reciprocal lattice vector, $\vec{r}_j$ is the position of particle j relative to an origin taken to be one of the particle positions, and the sum is over all particles j with $|\vec{r}_j| = r$, and $< . >$ indicates an ensemble average over origins and configurations. For 2D crystals, $G_{\vec{g}}(r)$ is expected to decay algebraically with distance, $G_{\vec{g}}(r) \sim r^{-\eta_T}$, with $\eta_T < 1/3$, while for hexatic and isotropic liquid phases, $G_{\vec{g}}(r)$ decays exponentially. It is expected that as the transition to the hexatic phase is approached from within the crystal phase, η_T approaches 1/3 from below.

1.3.7 Orientational Correlation Function

The orientational correlation function for 2D systems with hexagonal symmetry is measured by [55, 60, 66, 73, 74],

$$G_6(r) = \left\langle q_6(\vec{r}) q_6^*(\vec{0}) \right\rangle \tag{1.14}$$

$$q_6(\vec{r}_j) = \frac{1}{N_j} \sum_{k=1}^{N_j} \exp(6i\theta_{jk}), \tag{1.15}$$

where N_j is the number of nearest neighbours of particle j, θ_{jk} is the angle made by the bond with respect to an arbitrary but fixed axis between particle j and neighbour k, and q_6^* is the complex conjugate of q_6. KTHNY theory suggests that $G_6(r)$ for a crystal does not decay with distance. Instead, it saturates to a constant value. For the hexatic phase, $G_6(r)$ decays as a power law with distance, $G_6 \sim r^{-\eta_6}$, with $\eta_6 < 1/4$, while $G_6(r)$ decays exponentially in the liquid. For the square crystal, we use $G_4(r)$ with $q_4(\vec{r}) = \frac{1}{N_j} \sum_{k=1}^{N_j} \exp(4i\theta_{jk})$, where for the hexatic phase, we expect that $G_4(r)$

also decays as a power law with an exponent $\eta_4 < 1/4$.

1.4 Outline

The remainder of this thesis is organized as follows. In Ch. 2 we give a brief history of computer simulations and provide an overview of the simulation techniques used in subsequent chapters. In Ch. 3 we calculate and present the phase diagram for the SSSW model for a wide range of T and P and equivalently in the T-ρ plane. The phase diagram includes five crystals in addition to the liquid and gas. We also report in this chapter our findings for inverse melting, in which the liquid freezes to the crystal upon heating. In Ch. 4 we optimize the parameters of the SSSW potential to increase the range of pressures over which inverse melting is observed, and we find that melting remains first order, at least for the square crystal near the region of inverse melting. We further explore and find new behaviour for the optimized SSSW model at high pressure in Ch. 5. In Ch. 6 we summarize our results and discuss future work.

Bibliography

[1] P. C. Hemmer and G. Stell, Phys. Rev. Lett. **24**, 1284 (1970).

[2] G. Stell and P. C. Hemmer, J. Chem. Phys. **56**, 4274 (1972).

[3] J. S. Hoye and P. C. Hemmer, Physica Norvegica **7**, 1 (1973).

[4] A. Jayaraman, Phys. Rev. **137A**, 179 (1965).

[5] K. K. Mon, N. W. Ashcroft, and G. V. Chester, Phys. Rev. B **19**, 5103 (1979).

[6] M. Selbert and W. H. Young, Phys. Lett. **58** A, 469 (1976).

[7] D. Levesque and J. J. Weis, Phys. Lett. **60** A, 473 (1977).

[8] J. M. Kincaid and G. Stell, Phys. Lett. **65** A, 131 (1978).

[9] P. T. Cummings and G. Stell, Mol. Phys. **43**, 1267 (1981).

[10] A. Voronel, I. Paperno, S. Rabinovich, and E. Lapina, Phys. Rev. Lett. **50**, 247 (1983).

[11] K. K. Mon, N. W. Ashcroft, and G. V. Chester, J. Phys. F **15**, 1215 (1985).

[12] E. Velasco, L. Mederos, G. Navascues, P. C. Hemmer, and G. Stell, Phys. Rev. Lett. **85**, 122 (2000).

[13] C. H. Cho, S. Singh, and G. W. Robinson, Phys. Rev. Lett. **76**, 1651 (1996).

[14] M. R. Sadr-Lahijany, A. Scala, S. V. Buldyrev, and H. E. Stanley, Phys. Rev. Lett. **81**, 4895 (1998).

[15] M. R. Sadr-Lahijany, A. Scala, S. V. Buldyrev, and H. E. Stanley, Phys. Rev. E **60**, 6714 (1999).

[16] E. A. Jagla, J. Chem. Phys. **111**, 8980 (1999).

[17] E. A. Jagla, Phys. Rev. E **63**, 061501 (2001).

[18] E. A. Jagla, Phys. Rev. E **63**, 061509 (2001).

[19] A. Scala, M. R. Sadr-Lahijany, N. Giovambattista, S. V. Buldyrev, and H. E. Stanley, Phys. Rev. E **63**, 041202 (2001).

[20] A. B. de Oliveira, P. A. Netz, T. Colla, and M. C. Barbosa, J. Chem. Phys. **124**, 084505 (2006).

[21] T. Head-Gordon and F. H. Stillinger, J. Chem. Phys. **98**, 3313 (1993).

[22] F. H. Stillinger and T. Head-Gordon, Phys. Rev. E **47**, 2484 (1993).

[23] O. Mishima, Proc. Jpn. Acad., Ser. B **86**, (2010).

[24] F. H. Stillinger and A. Rahman, J. Chem. Phys. **60**, 1545 (1974).

[25] P. H. Poole, F. Sciortino, U. Essmann, and H. E. Stanley, Nature (London) **360**, 324 (1992).

[26] O. Mishima, L. D. Calvert, and E. Whalley, Nature **310**, 393 (1984).

[27] O. Mishima, L. D. Calvert, and E. Whalley, Nature **314**, 76 (1985).

[28] E. Rapoport, J. Chem. Phys. **46**, 2891 (1967).

[29] V. V. Brazhkin, S. V. Popova, and R. N. Voloshin, High Press. Res. **15**, 267 (1997).

[30] M. J. Cuthbertson and P. H. Poole, Phys. Rev. Lett. **106**, 115706 (2011).

[31] O. Mishima and H. E. Stanley, Nature **396**, 329 (1998).

[32] G. Franzese, G. Malescio, A. Skibinsky, S. V. Buldyrev, and H. E. Stanley, Nature (London) **409**, 692 (2001).

[33] V. N. Ryzhov and S. M. Stishov, Phys. Rev. E **67**, 010201(R) (2003).

[34] H. M. Gibson and N. B. Wilding, Phys. Rev. E **73**, 061507 (2006).

[35] C. J. Roberts and P. G. Debenedetti, J. Chem. Phys. **105**, 658 (1996).

[36] C. Buzano and M. Pretti, J. Chem. Phys. **119**, 3791 (2003).

[37] S. V. Buldyrev, G. Franzese, N. Giovambattista, G. Malescio, M. R. SadrLahijany, A. Scala, A. Skibinsky, and H. E. Stanley, Physica A **304**, 23 (2002).

[38] F. H. Stillinger and P. G. Debenedetti, Biophys. Chem. **105**, 211 (2003).

[39] M. P. Allen and D. J. Tildesley, *Computer Simulation of Liquids*. Oxford Science Publications, 1987.

[40] D. Frenkel and B. Smit, *Understanding Molecular Simulation: From algorithms to Applications*. San Diego, Academic Press, 1996.

[41] N. Metropolis, A. W. Rosenbluth, M. N. Rosenbluth, A. N. Teller, and E. Teller, J. Chem. Phys. **21**, 1087 (1953).

[42] R. A. Sadus, *Molecular simulation of fluids: Theory Algorithms and Object-Orientation*. Elsevier, Amsterdam, 1999.

[43] N. Metropolis, *Los Alamos Science.* **12**, 125 (1987).

[44] A. Qing, *Differential Evolution: Fundamentals and Applications in Electrical Engineering*. Wiley, (2009).

[45] W. W. Wood and F. R. Parker, J. Chem. Phys. **27**, 720 (1957).

[46] B. J. Alder and T. E. Wainwright, Molecular dynamics by electronic computers. In I. Progigine, editor, *Proc. of the Int. Symp. on Statistical Mechanical Theory of Transport Processes (Brussels, 1956)*. Interscience, Wiley, New York, 1958.

[47] J. B. Gibson, A. N. Goland, M. Milgram, and G. H. Vineyard, Phys. Rev. **120**, 1229 (1960).

[48] A. Rahman, Phys. Rev. **136**, A405 (1964).

[49] U. Wolff, Phys. Rev. Lett. **62**, 361 (1988).

[50] R. K. Pathria, *Statistical Mechanics*. Butterworth-Heinemann, 1996.

[51] J. M. Yeomans, *Statistical Mechanics of Phase Transitions*. Oxford Science Publications, 1992.

[52] J. P. Hansen and L. R. Mcdonald, Theory of Simple Liquids. Elsevier, London, 2006.

[53] N. Ashcroft and N. Mermin, *Solid State Physics*. Holt, Rinehart and Winston, 1976.

[54] D. Chandler, *Introduction to Modern Statistical Mechanics*. Oxford University Press, 1987.

[55] A. Brodin, A. Nych, U. Ognysta, B. Lev, V. Nazarenko, M. Skarabot, and I. Musevic, Condens. Matter Phys. **13**, 33601 (2010).

[56] P. Keim, G. Maret, and H. H. von Grunberg, Phys. Rev. E **75**, 031402 (2007).

[57] P. R. ten Wolde, M. J. Ruiz-Montero, and D. Frenkel, J. Chem. Phys. **104**, 9932 (1996).

[58] P. J. Steinhardt, D. R. Nelson, and M. Ronchetti, Phys. Rev. B **28**, 784 (1983).

[59] U. Gasser, C. Eisenmann, G. Maret, and P. Keim, Chem. Phys. Chem. **11**, 963 (2010).

[60] U. Gasser, J. Phys.: Condens. Matter **21**, 203101 (2009).

[61] A. P. Young, Phys. Rev. B **19**, 1855 (1979).

[62] D. R. Nelson and B. I. Halperin Phys. Rev. B **19**, 2457 (1979).

[63] C. H. Mak, Phys. Rev. E **73**, 065104 (2006).

[64] S. Z. Lin, B. Zheng, and S. Trimper, Phys. Rev. E **73**, 066106 (2006).

[65] K. Zahn and G. Maret, Phys. Rev. Lett. **85**, 3656 (2000).

[66] E. P. Bernard and W. Krauth, Phys. Rev. Lett. **107**, 155704 (2011).

[67] A. M. Almudallal, S. V. Buldyrev, and I. Saika-Voivod, J. Chem. Phys. **137**, 034507 (2012).

[68] S. T. Chui, Phys. Rev. B **28**, 178 (1983).

[69] W. Janke and H. Kleinert, Phys. Rev. B **41**, 6848 (1990).

[70] V. N. Ryzhov, Theor. Math. Phys. **88**, 990 (1991).

[71] V. N. Ryzhov, Zh. Eksp. Teor. Fiz. **100**, 1627 (1991).

[72] R. Peierls, Ann. Inst. Henri Poincare **5**, 177 (1935).

[73] J. Schockmel, E. Mersch, N. Vandewalle, and G. Lumay, Phys. Rev. E **87**, 062201 (2013).

[74] S. Prestipino, F. Saija, and P. V. Giaquinta, J. Chem. Phys. **137**, 104503 (2012).

Chapter 2

Methodology

2.1 Basics of Monte Carlo Method

We perform MC simulations to model a 2D system of interacting particles. With MC simulations, we start from an initial, often random, state which usually happens to be a non-equilibrium state, and then we follow a Markov process, where the generation of a new state depends only on the current state, i.e., does not depend on previous states. Different MC algorithms exist to produce different random walks, but the goal is to reach a steady state in which states are sampled according to a statistical mechanical ensemble. For example, to generate states in the grand canonical ensemble the random walk is generated not only by displacing particles, but by their insertion and deletion. Although the method seems to be simple, there are several details that we would like to discuss in the following subsections.

2.1.1 Reduced Units

It is very convenient in simulation studies to report all quantities in terms of reduced units. The basic units in simulations are mass (m), length (σ) and energy (ϵ), and

quantity	quantity in reduced units
Density	$\rho^* = \rho\sigma^3$ (3D), $\rho^* = \rho\sigma^2$ (2D)
Temperature	$T^* = k_B T/\epsilon$
Energy	$E^* = E/\epsilon$
Pressure	$P^* = P\sigma^3/\epsilon$ (3D), $P^* = P\sigma^2/\epsilon$ (2D)
Time	$t^* = (\epsilon/m\sigma^2)^{1/2}t$
Surface tension	$\gamma^* = \gamma\sigma^2/\epsilon$ (3D), $\gamma^* = \gamma\sigma/\epsilon$ (2D)

Table 2.1: Reduced units of some physical and thermodynamic quantities.

then all the other quantities can be expressed in terms of these basic units as explained in the following table [1, 2].

By working with reduced units we simplify the equations of motion and interaction potentials since the basic units are not written explicitly. If we work with the SI system, some quantities will be either very small or very large, and if we have a multiplication operation between such quantities, we might end up with a numerical overflow. With reduced units, all quantities will be typically in the range of $(10^{-3}, 10^3)$ [2]. Errors in this case will be easier to detect because if we obtain a very small or a very large number, most probably it will be due to an error. Using reduced units underlines the idea that we can simulate a single model to study different systems; the simulation results can be rescaled to different sets of physical units through the law of corresponding states, where different sets belong to different systems with qualitatively identical interactions, such as Ne, Ar and Kr [2].

2.1.2 Periodic Boundary Conditions

The aim of many computer simulation studies is to provide information about bulk properties of materials. With today's best computers, we can run simulations for

system sizes of up to a billion particles, but this number is still very far from the thermodynamic limit, and therefore surface effects can not be neglected. The problem of surface effects can be eliminated by implementing periodic boundary conditions. In periodic boundary conditions, the cubic simulation box is replicated in all directions to create a conceptually infinite lattice of identical boxes. When a particle moves in the original box, its image in each box, and particularly in each of the neighbouring boxes, moves in exactly the same way. Therefore, when a particle leaves the original box, an image will enter the original box from the opposite face. In this way, the walls are removed, and there are no surface objects [1, 2].

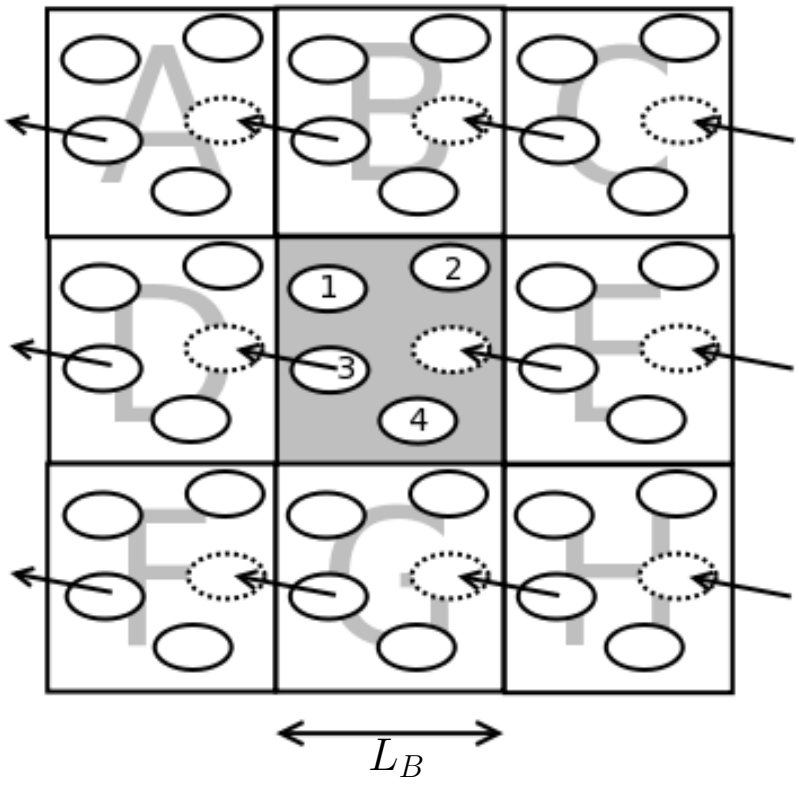

Figure 2.1: An example of a 2D boundary system as adapted from [1]. Each object can enter and leave any box across one of the four walls.

In Fig. 2.1 the grey box is the original box of length L_B, while the white boxes are the duplicated images for the grey box in all directions. As the dashed particle leaves

the original box, its images move across their corresponding boundaries. Hence, the number of particles in each box will be conserved. Practically speaking, using periodic boundary conditions does not require storing the coordinates of all images during the simulation [1, 2]; they can be reconstructed if need be. It is also worth mentioning that periodic boundary conditions can be applied to any box shape, but it would not be as direct as in the case of a cubic box. For example, in Chs. 3 and 5 we start with a square box and we implement anisotropic MC simulations, where we allow for each box edge to change independently and the angle to change as well. During the simulation, the square box becomes a parallelogram. Before we apply periodic boundary conditions, we rescale particle coordinates $\vec{r} = (R_x, R_y)$ in the parallelogram to fill a square box of unit length with scaled coordinates $\vec{S} = (S_x, S_y)$ using the following matrix representation,

$$\begin{pmatrix} S_x \\ S_y \end{pmatrix} = \begin{pmatrix} A_x & B_x \\ A_y & B_y \end{pmatrix}^{-1} \begin{pmatrix} x \\ y \end{pmatrix}.$$

This can be implemented with the following pseudocode,

$$\begin{aligned} det &= A_x * B_y - A_y * B_x \\ T_{11} &= B_y/det \\ T_{12} &= -B_x/det \\ T_{21} &= -A_y/det \\ T_{22} &= A_x/det \\ do\ I &= 1, N \\ S_x(I) &= T_{11} * R_x(I) + T_{12} * R_y(I) \\ S_y(I) &= T_{21} * R_x(I) + T_{22} * R_y(I) \\ enddo & \end{aligned}$$

where A_x and A_y are the x and y components of one of the vectors defining the simulation cells, and B_x and B_y are the components of the other vector. *det* is the determinant of the matrix formed from A_x, A_y, B_x, and B_y. The inverse of this matrix has elements T_{11}, T_{12}, T_{21} and T_{22}. R_x and R_y are particle coordinates in real space, S_x and S_y are the scaled coordinates in the square box of unit length, and N is the number of particles. After we apply the periodic boundary conditions, we can rescale the particles back to fill the parallelogram box.

2.1.3 Minimum Image Convention

In MC simulations, calculating the contribution to the potential energy due to a specific particle requires including the interactions between this particle and all other particles in the simulation box. In principle, we also must add the interaction between the particle and all other particles in the surrounding images. Since we have an infinite array of images, then we are talking about an infinite number of interactions and the calculation is impossible in practice. The minimum image convention was introduced to solve this problem, and in the following we will explain how this can be implemented. For particle 1 in Fig. 2.2, we construct an imaginary box, the dashed square box in the figure, which is centered on particle 1 and has the same size and shape as the original box. Particle 1 is then allowed to interact with all other particles located inside the imaginary box, 5_B, 2_E, 4_E, and 3. In this case particle 1 interacts with only $N-1$ particles instead of an infinite number of particles, and by applying this method to all other particles in the original box we will have $\frac{1}{2}N(N-1)$ terms due to pairwise interactions [1, 2].

To obtain the distance r between particle i and j in the minimum image convention for non-cubic boxes, we rescale the particles as in the previous section and we then use the following pseudocode, where *nint(x)* returns the nearest integer to x.

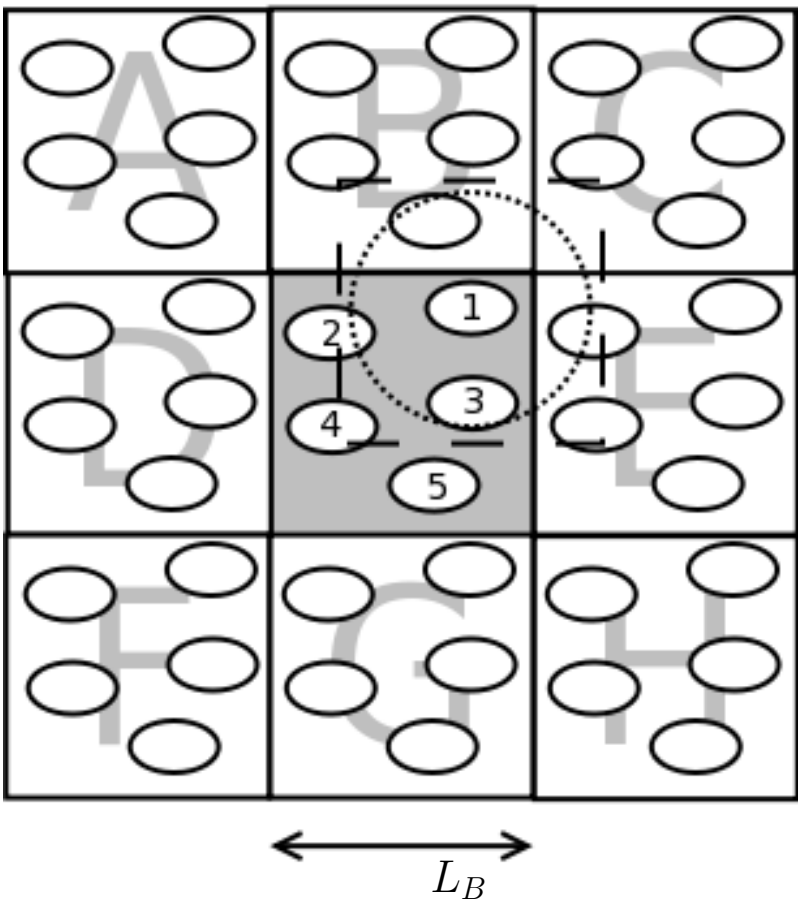

Figure 2.2: The minimum image convention for a 2D system, as adapted from [1]. The dashed square is the new box constructed for particle 1 using the minimum image convention. The new box contains the same number of particles as the original box. The dashed circle represents a potential cutoff.

$$dS_x = S_x(J) - S_x(I) - nint(S_x(J) - S_x(I))$$

$$dS_y = S_y(J) - S_y(I) - nint(S_y(J) - S_y(I))$$

$$dx = A_x\ dS_x + B_x\ dS_y$$

$$dy = A_y\ dS_x + B_y\ dS_y$$

$$r = \sqrt{(dx)^2 + (dy)^2}$$

2.1.4 Potential Truncation

Although our potential is zero beyond the attractive well, in general truncating potentials has an effect on the quantities calculated. The necessity of truncating potentials arises from the fact that with the minimum image convention, the total number of interactions is reduced from an infinite number to $\frac{1}{2}N(N-1)$, but this number is still too large for a system of number of particle > 1000. For short range interactions, the total potential energy is dominated by the interaction between the particle of interest and neighbouring particles. Hence, to reduce the number of interactions, we apply a spherical cutoff (r_c) and we only consider the interactions between the particle of interest and other particles within r_c. In this case we are making an error by neglecting the interactions with the particles outside r_c. We can reduce the error by applying a bigger r_c, but we should restrict r_c to be less than half the box length to prevent interactions with duplicate images [1, 2].

To illustrate this point, the dashed circle in Fig. 2.2 is the cutoff circle for particle 1. According to the cutoff criteria, only particles 3 and 5_B are interacting with particle 1, while particles 2_E and 4_E do not contribute because their centres are located outside the circle.

The potential energy contribution that is neglected for $r > r_c$ is (for 2D system) [2,3],

$$U_{tail} = N\pi\rho \int_{r_c}^{\infty} ru(r)g(r)dr, \tag{2.1}$$

where ρ is the number density, $u(r)$ is the interaction potential and $g(r)$ is the radial distribution function. In practice, for a liquid there is very little correlation between particles at long distances, i.e., to a good approximation $g(r) = 1$ for $r > r_c$. We also

can calculate the pressure tail correction for the 2D system via [2, 3],

$$P_{tail} = \frac{\pi\rho^2}{2}\int_{r_c}^{\infty} r^2 \frac{du}{dr} g(r) dr. \tag{2.2}$$

It is obvious from Eqs. 2.1 and 2.2 that the tail corrections diverge unless $u(r)$ decays more rapidly than r^{-2} in 2D (or r^{-3} in 3D). However, Coulomb and dipolar interactions decay as r^{-1} and r^{-3}, respectively, and hence are problematic. In this case, a common approach to make the energy calculation tractable is to apply Ewald summation techniques, which involve calculating contributions from long range interactions in reciprocal space [4–7].

Although the cutoff radius reduces the number of interactions contributing to the system energy, we still need to compute all the $\frac{1}{2}N(N-1)$ pair distances to decide which pairs interact. For big systems ($N > 1000$), truncation by itself is not efficient, and therefore we need to adopt tricks to speed up the calculations, such as Verlet neighbour list and cell list [2, 8, 9]. In the Verlet neighbour list method, a second cutoff radius $r_v > r_c$ is introduced, and a list is made for each particle to include all particles within a radius r_v. We calculate only the distances between a particle and those in its own list, and once a particle is displaced a distance greater than $(r_v - r_c)/2$ we update the lists of all particles. This method is expected to reduce the time needed to finish the simulations from $\sim N^2$ to $\sim N$. However, constructing the list is still of order $\sim N^2$ and therefore r_v should not be so small that the neighbour list is updated frequently.

In the cell list method, the simulation box is divided into cells of size slightly bigger than r_c. Each particle is allowed to interact only with those particles in its own or neighbouring cells. This method also reduces the simulation time from $\sim N^2$ to $\sim N$.

2.1.5 Metropolis MC

The Metropolis algorithm is the original algorithm used in the first MC simulations. The dynamics of generating a new configuration stems from considering an ensemble of particle configurations or microstates in equilibrium. In equilibrium, the number of ensemble members $N(x)$ in a given microstate x is stationary: the distribution is in balance. Let $K(o \to n)$ be the flow of ensemble members from microstate o to microstate n, i.e., the number of ensemble members in state o that convert to state n in one step of the evolution algorithm. Balance can be achieved globally through,

$$\sum_x K(o \to x) = \sum_x K(x \to o), \tag{2.3}$$

that is, the flow out of state o (to all other possible states) is balanced by the flow into state o from all other states.

The Metropolis algorithm is based on maintaining equilibrium through *detailed* balance,

$$K(o \to n) = K(n \to o) \tag{2.4}$$

that is, the flow between every pair of states is balanced. This more restrictive condition is more straightforward to use in generating an algorithm. We continue by writing $K(o \to n)$ as a product $N(o)\,\alpha(o \to n)\,acc(o \to n)$, where $\alpha(o \to n)$ is the probability of attempting to generate state n given the current state o, and $acc(o \to n)$ is the probability of accepting the proposed move from o to n. Thus we arrive at,

$$N(o)\,\alpha(o \to n)\,acc(o \to n) = N(n)\,\alpha(n \to o)\,acc(n \to o). \tag{2.5}$$

By choosing the condition

$$\alpha(o \to n) = \alpha(n \to o), \tag{2.6}$$

which is achieved by generating new random states in a non-biased way (and which can be broken inadvertently by subtle effects when implementing the code), the detailed balance condition then reduces to,

$$N(o)acc(o \to n) = N(n)acc(n \to o). \tag{2.7}$$

At this point enters statistical mechanics. For the canonical ensemble, the distribution of states follows the Boltzmann distribution,

$$N(o) \propto \exp(-\beta U(o)), \tag{2.8}$$

where $U(o)$ is the potential energy of microstate o (assuming independence of velocities and spatial coordinates), and we arrive at a condition on the acceptance probabilities,

$$\frac{acc(o \to n)}{acc(n \to o)} = \frac{N(n)}{N(o)} = \exp(-\beta(U(n) - U(o))). \tag{2.9}$$

A definition of the acceptance probability that satisfies this relation is,

$$acc(o \to n) = \begin{cases} 1 & \text{for } U(o) > U(n) \\ \exp(-\beta(U(n) - U(o))) & \text{otherwise} \end{cases} \tag{2.10}$$

For other statistical ensembles, the acceptance probability is determined by the distribution function appropriate to that ensemble, but the idea is the same.

The Metropolis algorithm can be implemented practically in the following way. We start by moving a randomly chosen particle a uniform random displacement along each of the coordinate axes. In passing we note that selecting particles sequentially breaks the detailed balance condition explicit in Eq. 2.6. The maximum displacement that the particle can move is δr_{max} in either x and y. The new position of the particle

(ζ_{new}) is determined by Eq. 2.11 [1, 2],

$$\zeta_{new} = \zeta_{old} + (2.0 * rand - 1.0) * \delta r_{max}, \tag{2.11}$$

where $\zeta = x$, y and z and *rand* is a uniform random number on (0,1). We then calculate the total interaction energy of the system for both cases, before moving the particle (V_i) and after moving the particle (V_f). If ($\delta V_{fi} = V_f - V_i \leq 0$), we accept the first particle move. But if ($\delta V_{fi} > 0$), the move is accepted with a probability $\exp(-\beta\ \delta V_{fi})$. The $\exp(-\beta\ \delta V_{fi})$ quantity is the Boltzmann factor of the energy difference, which has a value in the range (0, 1). We simply compare the Boltzmann factor with *rand*, and then we accept the move if $\exp(-\beta\ \delta V_{fi}) > rand$, otherwise we reject the move.

If the particle move is accepted, we then update the particle configuration to include the new position of the particle ($x_i = o$, $x_{i+1} = n$), but if the move is rejected we recover the previous configuration ($x_i = o$, $x_{i+1} = o$). In the SSSW model, we deal with a system of hard particles, thus any attempted move that generates an overlap will be rejected and no energy criterion need be tested. By repeating this method millions of times on average per particle, the system is driven from the initial non-equilibrium state to steady state where it samples states according to an equilibrium distribution, i.e., it achieves the equilibrium macrostate.

The parameter δr_{max}, which determines the maximum displacement of particle moves, should be an adjustable parameter during the simulation. If this parameter is too small, phase space will be explored slowly, even if most particle moves are accepted. Alternatively, if δr_{max} is too large, most of the moves will be rejected and again the phase space will be explored slowly. Therefore, δr_{max} is typically adjusted during the simulation so that about half the moves are accepted. In principle, allowing

δr_{max} to fluctuate breaks detailed balance by violating Eq. 2.6 and so it is better to fix δr_{max} once equilibrium is reached. In practice, this is not a large concern since δr_{max} itself equilibrates to a (nearly) constant value.

2.2 Free Energy Techniques

Several computer simulation techniques can be used to study phase behaviour of a particular system. Determining which technique is required to be used depends on the character of the phase transition. For example, techniques used to study first order transitions are different from those used to study second order transitions. In this section, we will focus on the techniques required to study a first order transition and to determine the coexistence curve between two different phases. These techniques are mainly based on free energy calculations. The necessity of developing these techniques is that the free energy can not be measured directly from simulation, because it is not an average of functions of the phase space coordinates. Instead it is related to the volume of the phase space and therefore related directly to the partition function [2].

2.2.1 Thermodynamic Integration

To compute the free energy for a particular system at a given T and V, we should link the system by a reversible path at constant T and V to a system of known free energy. The change in the free energy along the path can be calculated by generalized thermodynamic integration [2]. Some examples on systems with known free energies are the ideal gas and Einstein crystal.

To find the free energy for a liquid, we link the liquid to the ideal gas by the fact that above the liquid-gas critical point the free energy of the liquid (fluid, technically) approaches that of the ideal gas as density approaches zero. Once this identification

is made, we can use the relation,

$$P = -\left(\frac{\partial F}{\partial V}\right)_{NT}, \tag{2.12}$$

to find Helmholtz free energy difference between state points along an isotherm. In other words, we can integrate the equation of state $P(\rho)$ from very low density, where the system behaves as an ideal gas, to arbitrary density, in order to find the Helmholtz free energy per particle of the liquid [2],

$$\beta f(\rho) = \beta f_{id}(\rho) + \beta \int_0^\rho d\rho' \left(\frac{P(\rho') - \rho' k_B T}{\rho'^2}\right), \tag{2.13}$$

where f_{id} is the Helmholtz free energy of the ideal gas per particle and the numerator in the integrand represents the excess pressure. When performing this integration, it is important that the integration path does not cross a first order transition. If the starting and ending points of the integration are separated by a first order transition, the integration is done in two steps along a path that avoids the transition by passing beyond the critical point. First we integrate at T well above the critical temperature, and second the system is cooled at constant density to the desired temperature. The change in free energy in the second step is [2],

$$\beta_2 f(T_2) = \beta_1 f(T_1) + \frac{1}{N} \int_{T_1}^{T_2} d(1/T) E(V, T), \tag{2.14}$$

where $\beta_\alpha = 1/(k_B T_\alpha)$ and $E(V, T)$ is the total energy.

2.2.2 Frenkel-Ladd Method

For the solid phase, we link the solid to the Einstein crystal, where all atoms are coupled harmonically to their lattice sites. Calculating the free energy of a solid is

not as simple as the case of a liquid. A few techniques can be used to calculate the free energy for a solid, but in this thesis we will discuss only one technique, which is the Frenkel-Ladd Method.

This technique is well-explained in Chs. 7 and 10 of Ref [2], and the steps of the algorithm are detailed in Ch. 3 of this thesis. Here, we simply recount a few background ideas, primarily related to the generalization of thermodynamic integration, where state points differ not in their pressure or temperature, but in the value of a parameter that controls the interaction potential governing the system.

For example, we can define a potential energy,

$$U_\lambda = U_{\text{ref}} + \lambda \left(U_{\text{target}} - U_{\text{ref}} \right), \tag{2.15}$$

where λ is a parameter that continuously transforms the system from a reference system ($\lambda = 0$), for which the free energy is known, to the target system ($\lambda = 1$) for which the free energy is being calculated. Through the fundamental theorem of calculus, the Helmholtz free energy difference between target and reference systems can be written as,

$$\Delta F = F_{\text{target}} - F_{\text{ref}} = F(\lambda = 1) - F(\lambda = 0) = \int_0^1 d\lambda \left(\frac{\partial F(\lambda)}{\partial \lambda} \right)_{N,V,T}. \tag{2.16}$$

The trick is to write the derivative of F with respect to λ in terms of quantities one can obtain in simulation. This can be accomplished by first writing down an extended partition function based on $U(\lambda)$,

$$Q(N, V, T, \lambda) = \frac{1}{\Lambda^{3N} N!} \int d\vec{r}^N \exp\left[-\beta U(\lambda) \right], \tag{2.17}$$

where Λ is the thermal wavelength, and hence $F(\lambda) = -\beta^{-1} \ln Q(N, V, T, \lambda)$. The

desired derivative then follows via,

$$\begin{aligned}\left(\frac{\partial F(\lambda)}{\partial \lambda}\right)_{N,V,T} &= -\frac{1}{\beta Q(N,V,T,\lambda)}\frac{\partial Q(N,V,T,\lambda)}{\partial \lambda} \\ &= \frac{\int d\vec{r}^N \frac{\partial U(\lambda)}{\partial \lambda}\exp\left[-\beta U(\lambda)\right]}{\int d\vec{r}^N \exp\left[-\beta U(\lambda)\right]} \\ &= \left\langle \frac{\partial U(\lambda)}{\partial \lambda}\right\rangle_\lambda \\ &= \left\langle U_{\text{target}} - U_{\text{ref}}\right\rangle_\lambda .\end{aligned} \tag{2.18}$$

To calculate the last quantity, one first generates an ensemble of configurations using the interaction potential implicit in Eq. 2.15 at a particular value of λ. Then for each configuration, one calculates the potential energy according to the target interaction and again according to the reference interaction. The average of this difference is equal to the integrand in Eq. 2.16 and one obtains,

$$F_{\text{target}}(N,V,T) = F_{\text{ref}}(N,V,T) + \int_0^1 d\lambda \left\langle U_{\text{target}} - U_{\text{ref}}\right\rangle_\lambda . \tag{2.19}$$

While the above provides a general framework for this type of free energy calculation, hard particles present an added difficulty in that it is problematic to continuously switch off the infinite hard core repulsion. Instead of using a potential as in Eq. 2.15, one defines,

$$U_\lambda = U(\vec{r}^N) + \lambda \sum_{i=1}^{N} (\vec{r}_i - \vec{r}_{0,i})^2, \tag{2.20}$$

where $\vec{r}_i$ is the position of particle i and $\vec{r}_{0,i}$ is its ideal lattice position, and $U(\vec{r}^N)$ is the original (SSSW) potential. This $U(\lambda)$ results in a method based on tracking the average value of the mean-square displacement as a function of λ. Instead of integrating from $\lambda = 0$ to 1 (there is nothing special about $\lambda = 1$), one needs to obtain data until the system exhibits ideal harmonic behaviour at sufficiently high λ.

2.2.3 Gibbs Ensemble

One way to locate the coexistence point between two phases is to perform a direct NVT simulation at the right value of V and T. At equilibrium, the system will separate into two regions, one for each phase. To obtain an accurate location of the coexistence point, we should consider a big system to decrease the ratio of interface particles, but this way will be computationally expensive. In the case of liquid-gas or liquid-liquid equilibria, we can apply the Gibbs Ensemble method, devised by Panagiotopoulos [10], to study the coexistence.

As mentioned before, the conditions of coexistence are that the T, P, and μ of the two phases should be the same. In the Gibbs ensemble method, we initialize the system in two separated boxes (without the presence of an interface), where the total number of particles and the total volume of the two subsystems are fixed. To achieve the coexistence conditions, we perform three different kinds of trial MC moves. First, particle displacement within each subsystem, second, volume fluctuations of the two subsystems, and third, transferring particles between the two subsystems. As the system evolves, the two subsystems will each tend to a single phase. The free exchange of V and N between subsystems results in mechanical and chemical equilibration, i.e., both subsystems will have the same P and μ, although neither of them are known. The phases will be at the same (specified) T and will exist at the different (coexistence) densities.

Having determined the coexistence densities as a function of T with the Gibbs ensemble, we can determine the coexistence pressure using the virtual volume method of Haresmiadis *et al* [11]. In this method, we simulate the gas and liquid in two independent MC NVT simulations at a given T and at their respective coexistence

densities. The pressure can be derived from,

$$P = -\left(\frac{\partial F}{\partial V}\right)_{N,T}. \tag{2.21}$$

For a small volume change from V to V', P can be written as,

$$P \approx -\left(\frac{\Delta F}{\Delta V}\right) = \frac{k_B T}{\Delta V} \ln\left(\frac{Q_{V'}}{Q_V}\right) \tag{2.22}$$

where we have used the relation $F = -k_B T \ln Q_V$, $\Delta V = V' - V$, and Q is the partition function for the canonical ensemble given by,

$$Q = \int \frac{V^N}{\Lambda^{3N} N!} \exp\left(-\beta U_V\right) d\mathbf{r}^N, \tag{2.23}$$

where the integration is over dimensionless particle coordinates that have been rescaled by the box length, and this accounts for the "extra" factor of V^N. The pressure can then be expressed as,

$$\begin{aligned} P &= \frac{k_B T}{\Delta V} \ln\left(\frac{\int \frac{V'^N}{\Lambda^{3N} N!} \exp(-\beta U_{V'}) d\mathbf{r}}{\int \frac{V^N}{\Lambda^{3N} N!} \exp(-\beta U_V) d\mathbf{r}}\right) \\ &= \frac{k_B T}{\Delta V} \ln\left[\left\langle \left(\frac{V'}{V}\right)^N \exp\left(-\beta \Delta U\right)\right\rangle\right], \end{aligned} \tag{2.24}$$

where ΔU is the potential energy difference between a configuration with particle coordinates isotropically rescaled to accommodate the virtual volume V' and the unaltered configuration with original volume V and $\langle \dots \rangle$ indicates an ensemble average.

Close to the critical temperature (T_C), coexistence is no longer clearly observed in the simulations because the free energy associated with the formation of the liquid-vapor interface becomes vanishingly small [12]. To determine the critical temperature,

we fit the density difference of the two coexisting phases to a scaling law [2, 13, 14],

$$\rho_l - \rho_g = A|T - T_C|^{\beta_c}, \tag{2.25}$$

where ρ_l and ρ_g are the coexistence liquid and gas densities respectively. β_C is a critical exponent and for 2D systems $\beta_C = 0.125$ and A is a fit constant. The critical density (ρ_C) is determined by fitting our results to the law of rectilinear diameters [2, 13, 14],

$$\frac{\rho_l + \rho_g}{2} = \rho_C + B|T - T_C|, \tag{2.26}$$

where B is a fit constant, and T_C is used from the fit in Eq. 2.25. The critical pressure P_C is determined by fitting the gas pressure curve to the Clausius-Clapeyron equation [14, 15],

$$\ln P = C + \frac{D}{T}, \tag{2.27}$$

where C and D are fit constants.

2.2.4 Gibbs-Duhem Integration

After locating a single coexistence point between two phases at specific T and P, we then can trace the rest of the coexistence curve without any further free energy calculations. The method for achieving this goal was developed by Kofke, who refers to his method as Gibbs-Duhem integration [12, 16, 17]. To illustrate the derivation and the usage of this method, we start by the following relation,

$$d\mu = -sdT + vdP, \tag{2.28}$$

where s and v are the entropy per particle and volume per particle, respectively. Two phases I and II can coexist when their T, P, and μ are the same. If we give both T and P a small deviation, then the difference in the chemical potential can be written as,

$$d\mu_{II} - d\mu_I = -(s_{II} - s_I)dT + (v_{II} - v_I)dP. \tag{2.29}$$

At any point on the coexistence curve, $d\mu_{II} - d\mu_I = 0$ must be satisfied, and therefore we can write Eq. 2.29 as the well-known Clausius-Clapeyron relation,

$$\frac{dP}{dT} = \frac{s_{II} - s_I}{v_{II} - v_I} = \frac{\Delta s}{\Delta v} = \frac{\Delta h}{T\Delta v}, \tag{2.30}$$

where h is the enthalpy per particle, and here we have used the relation $dh = Tds$, because enthalpy is much easier to calculate than entropy. To implement this method, we run two independent simulations, one for phase I and another for phase II, at coexistence T and P. From the output of the two simulations, we can calculate the right hand side of Eq. 2.30, and by integration we can locate another coexistence point on the curve. We carry out the integration using a second-order predictor-corrector method [18, 19].

2.2.5 Hamiltonian Gibbs-Duhem Integration

When applying a small perturbation to the interaction potential, the location of a coexistence point will change slightly. To determine the new location of the coexistence point, we implement Hamiltonian Gibbs-Duhem integration. This type of integration is also a thermodynamic integration, and therefore we have to use a coupling parameter λ to switch between the original potential (U_A) and the perturbed one (U_B) [20, 21],

$$U(\lambda) = (1 - \lambda)U_A + \lambda U_B. \tag{2.31}$$

When $\lambda = 0$, we recover U_A and when $\lambda = 1$ we switch the potential to U_B. To explain the theory and the implementation of this method, we start by relation 2.28 for two phases I and II,

$$d\mu_{II} - d\mu_I = -(s_{II} - s_I)dT + (v_{II} - v_I)dP + \left(\frac{\delta U_{II}}{\delta\lambda} - \frac{\delta U_I}{\delta\lambda}\right)d\lambda. \tag{2.32}$$

The last term represents the change in the chemical potential due to the change in the potential energy. To simplify the method, we fix either T or P. In the following, we assume T is fixed and we take into consideration that $d\mu_{II} - d\mu_I = 0$ at coexistence [20, 21],

$$\left.\frac{dP}{d\lambda}\right|_T = -\frac{\langle \delta U_{II}/\delta\lambda\rangle_{NPT\lambda} - \langle \delta U_I/\delta\lambda\rangle_{NPT\lambda}}{v_{II} - v_I} \tag{2.33}$$

$$= -\frac{\langle U_B - U_A\rangle^{II}_{NPT\lambda} - \langle U_B - U_A\rangle^{I}_{NPT\lambda}}{v_{II} - v_I} \tag{2.34}$$

where $\langle \dots \rangle_{NPT\lambda}$ indicates an average in the NPT ensemble when the system is governed by $U(\lambda)$. In a similar way, the differential equation when P is constant will be [20, 21],

$$\left.\frac{dT}{d\lambda}\right|_P = T\frac{\langle U_B - U_A\rangle^{II}_{NPT\lambda} - \langle U_B - U_A\rangle^{I}_{NPT\lambda}}{h_{II} - h_I}. \tag{2.35}$$

To implement the method, we start by two independent simulations, one for each phase, at $\lambda = 0$. We then calculate the R.H.S of Eq. 2.34 or Eq. 2.35 from the output of the two simulations. By integration we can determine the new coexistence point for the potential U_B at $\lambda = 1$. In this thesis, we switch from $\lambda = 0$ to $\lambda = 1$ gradually by choosing $\delta\lambda = 0.1$. Here also, we carry out the integration using a second-order predictor-corrector method [18, 19].

2.2.6 Umbrella Sampling

Umbrella sampling is a method used in simulation to improve sampling of systems that suffer from poor sampling [2, 22]. In particular, we use umbrella sampling in systems that have a large energy barrier that separates two regions of configurational space. This gives a low probability to overcoming the energy barrier and to sample the two configurational spaces. With umbrella sampling we add a constraint potential U_c,

$$U_c = \frac{k}{2}(\rho - \rho_0)^2 \tag{2.36}$$

to the pair potential energy U. The biasing potential will force a given simulation to sample densities in the vicinity of ρ_0. k is a constant that controls the range of sampled densities. We implement umbrella sampling within NPT simulations in different windows with equally spaced values of ρ_0. We obtain the probability distribution $P_r(\rho)$ by converting the constrained ensemble $P_{rc}(\rho)$ via $\exp[\beta U_c(\rho)]P_{rc}(\rho)$. We determine the pieces of conditional Gibbs free energy ($\Delta G(T, P; \rho)$) for each window via,

$$\Delta G(T, P; \rho) = -k_B T \ln[P_r(\rho)]. \tag{2.37}$$

We combine and shift all the pieces to produce a smooth $\Delta G(T, P; \rho)$ for the entire density range. The values of P and T chosen to perform the umbrella sampling might be not exactly at the coexistence conditions, which produces a free energy curve with unequal weight. To precisely locate the coexistence pressure (P'), we apply a pressure shift ΔP to reweight the $\Delta G(T, P; \rho)$,

$$\beta\Delta G(T, P'; \rho) = \beta\Delta G(T, P_0; \rho) + \frac{N\beta\Delta P}{\rho} + c, \tag{2.38}$$

where c is a constant related to normalization, and $P' = P_0 + \Delta P$, where P_0 is the

original coexistence pressure at which the constrained simulations are performed.

Bibliography

[1] M. P. Allen and D. J. Tildesley, *Computer Simulation of Liquids*. Oxford Science Publications, 1987.

[2] D. Frenkel and Berend Smit, *Understanding Molecular Simulation: From algorithms to Applications*. San Diego, Academic Press, 1996.

[3] J. P. Hansen and J. R. Mcdonald, Theory of Simple Liquids. Elsevier, London, 2006.

[4] P. P. Ewald, Ann. Phys. **64**, 253 (1921).

[5] S. W. de Leeuw, J. W. Perram, and E. R. Smith, Proc. R. Soc. London A **373**, 27 (1980).

[6] S. W. de Leeuw, J. W. Perram, and E. R. Smith, Proc. R. Soc. London A **373**, 56 (1980).

[7] S. W. de Leeuw, J. W. Perram, and E. R. Smith, Proc. R. Soc. London A **388**, 177 (1983).

[8] L. Verlet, Phys. Rev. **159**, 98 (1967).

[9] R. W. Hockney and J. W. Eastwood, *Computer Simulations Using Particles*, McGraw-Hill, New York, 1981.

[10] A. Z. Panagiotopoulos, Mol. Phys. **61**, 813 (1987).

[11] V. I. Harismiadis, J. Vorholz, and A. Z. Panagiotopoulos, J. Chem. Phys. **105**, 8469 (1996).

[12] A. M. Almudallal, S. V. Buldyrev, and I. Saika-Voivod, J. Chem. Phys. **137**, 034507 (2012).

[13] M. G. Noro and D. Frenkel, J. Chem. Phys. **114**, 2477 (2001).

[14] L. Vega, E. de Miguel, L. F. Rull, G. Jackson, and I. A. Mclure, J. Chem. Phys. **96**, 2296 (1992).

[15] B. Garzck, S. Lago, and Carlos Vega, J. Chem. Phys. **101**, 4166 (1994).

[16] D. A. Kofke, Mol. Phys. **78**, 1331 (1993).

[17] D. A. Kofke, J. Chem. Phys. **98**, 4149 (1993).

[18] M. H. Lamm and C. K. Hall, AIChE J. **50**, 215 (2004).

[19] The algorithm used is $P_{i+1} = P_i + \Delta T(f_i + f_{i+1})/2$, where f_i is the right hand side of Eq. 2.1, the evaluation of which requires one NPT MC simulation for each phase at temperature T_i and pressure P_i. Alternatively, we iterate $T_i + 1 = T_i + \Delta P(1/f_i + 1/f_{i+1})/2$. This is especially useful in the vicinity of the melting temperature maximum of the S-L coexistence curve.

[20] C. Vega, E. Sanz, J. L. F. Abascal, and E. G. Noya, J. Phys.: Condens Matter **20**, 153101 (2008).

[21] F. Romano, E. Sanz, and F. Sciortino, J. Chem. Phys. **132**, 184501 (2010).

[22] G. M. Torrie and J. P. Valleau, J. Comp. Phys. **23**, 187 (1977).

Chapter 3

Phase diagram of a two-dimensional system with anomalous liquid properties

3.1 Abstract

Using Monte Carlo simulation techniques, we calculate the phase diagram for a square shoulder-square well potential in two dimensions that has been previously shown to exhibit liquid anomalies consistent with a metastable liquid-liquid critical point. We consider the liquid, gas and five crystal phases, and find that all the melting lines are first order, despite a small range of metastability. One melting line exhibits a temperature maximum, as well as a pressure maximum that implies inverse melting

over a small range in pressure.

3.2 Introduction

Core-softened potentials were first used by Stell, Hemmer and coworkers in a lattice gas system to discuss the isostructural solid-solid phase transition that ends in a second critical point [1–3]. Core-softened potentials were also used to study single-component systems in a liquid state, such as liquid metals [4–11]. They have been also used to study liquid anomalies in 1D [12–14] and 2D [15–18]. Calculations in Ref. [19, 20] show that a core-softened potential can be considered as a realistic first-order approximation for the real interaction between water molecules resulting from averaging over the angular part.

Interest in the study of liquid-liquid (L-L) phase transitions in single component systems grew dramatically after such a transition and accompanying critical point were proposed for water as an explanation for its anomalous properties [21]. Various studies have been done to understand the L-L phase transition and associated phenomena. Some of these studies focussed on the "two-liquid" model to explain liquid properties [22–24]. Other studies were based on using anisotropic potentials [25, 26]. Franzese *et al.* showed that the liquid-liquid phase transition and accompanying critical point can also arise from a shoulder-like potential with two characteristic distances (hard-core and soft-core) [27]. In this work, the authors reported in 3D molecular dynamics (MD) simulations the existence of two liquid phases, the low-density liquid phase and the high-density liquid phase, and showed that these two phases can occur in the system with no density anomaly. On the other hand, 2D simulation studies reproduce the density anomaly but no second critical point [13]. For a review of unusual behavior of isotropic potentials with two energy scales in 2D, see Ref. [28]. In

general, the phase behavior of 2D systems is richer than that of 3D systems, with crystallization able to proceed through a hexatic phase [29], or even through a less well understood way when long-range repulsions are present [30].

Gibson and Wilding [31] studied a family of ramp potentials [16] for which the L-L critical point systematically moved from a stable position in the phase diagram to a metastable one. Ryzhov and Stishov [32] tracked the change of the L-L transition line as a function of the width of the shoulder in a square shoulder potential. A fuller examination of the phase behavior of the square shoulder potential [33, 34] placed the liquid anomalies in the context of the crystal phases and gave emphasis to the "quasi binary mixture" nature of the system at low temperature (which allows for an "amorphous gap" of increased liquid stability between crystal structures as a function of density). Lattice models have also played a role in gaining basic insight into the mechanism of the L-L transition and associated liquid state anomalies [35, 36], and are more amenable to analytic treatments [37, 38].

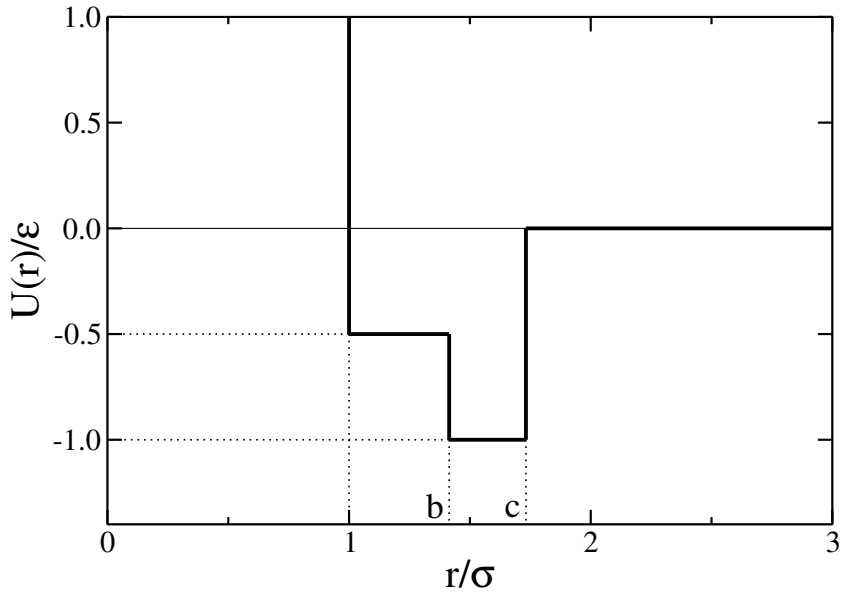

Figure 3.1: The pair potential used in this study is an isotropic step potential with hard-core diameter σ. $b = \sqrt{2}\sigma$ is the soft-core distance, and $c = \sqrt{3}\sigma$ is the attractive distance limit. r is the distance between two particles and ϵ is the bond energy.

Scala and coworkers [18] carried out MD simulations in 2D of the square-shoulder square-well (SSSW) potential shown in Fig. 3.1 to study liquid anomalies. Buldyrev *et al* [39] continued with the SSSW model in 2D and 3D in order to study liquid-liquid phase transitions. For the 2D system, they produced a phase diagram showing liquid anomalies in relation to approximate crystallization lines for a range in pressure P and temperature T near a potential L-L critical point. Their phase diagram shows the gas-liquid coexistence curve and crystallization lines for a low density triangular and higher density square crystal. It also shows the first critical point and the hypothetical position of the second critical point, which coincides with the crossing of the two crystallization lines. Thus, unavoidable crystallization renders the L-L critical point not directly observable, or obscured. Their crystallization lines were determined from examining the behavior of the pressure, structure and dynamics along isochores. They are estimates of the limit of liquid stability, or rather the limit of metastability, with respect to the crystal, rather than thermodynamically determined coexistence lines. As the system is two-dimensional, the nature of the crystallization transition is also under question, in so far that in two dimensions, crystallization can proceed in a continuous way via a hexatic phase rather than through a first-order phase transition.

In the present work, we carry out free energy calculations, based primarily on Monte Carlo (MC) simulation, to determine the coexistence conditions between the liquid and crystal phases for a wide range of P and T, including the smaller range presented in Ref. [39]. In doing so, we find two low density crystal phases not previously reported for the model. We find that all the transitions are at least weakly first-order. The crystallization lines reported in Ref. [39] are below our calculated melting lines. Additionally, the square crystal shows a maximum temperature in its melting curve, as well as a maximum in pressure. Thus, the present model is a useful one for studying the rare phenomenon of inverse melting, in which the liquid may

freeze to the crystal upon heating.

This paper is organized as follows. In Section II, we discuss all the free energy and computer simulation techniques used in carrying out this work. In section III, we show our results. In Section IV we present a discussion and we give our conclusions in Section V.

3.3 Methods

3.3.1 Model and simulations

The model we study is the step pair potential shown in Fig. 3.1. As we are carrying out our studies in two dimensions, the model describes disks with a hard-core diameter σ and an attractive well extending out to a radial distance of $c = \sqrt{3}\sigma$. The attractive well itself contains a shoulder, with a pair interaction energy of $-\epsilon/2$ for $\sigma < r < b$ and energy of $-\epsilon$ for $b < r < c$. The parameter b was originally chosen to be $\sqrt{2}\sigma$ so that there would exist a low density triangular (LDT) phase and a higher density square (S) phase with the same potential energy per particle of -3ϵ, i.e. two energetically degenerate phases of well separated densities [39]. The idea behind this was to allow for distinct liquid states, one based on square packing and the other on the more open triangular packing, in analogy to what is thought to be the case for water. At high pressure the system ultimately must form the close-packed triangular phase (HDT), with potential energy per particle of -1.5ϵ. We find two additional crystals, phases A and Z, with per particle energies -3.25ϵ and -3.5ϵ, respectively. The various crystal phases are depicted in Fig. 3.2. Our goal is to calculate coexistence lines between the five crystal phases, the liquid (L) and the gas (G).

The liquid-state properties of the model were extensively studied in Ref. [39] using discrete MD simulation. The S and LDT crystallization lines were determined in that

work from pressure isochores and from direct observation of crystal-like structural and dynamical behavior. Here, we calculate the crystal coexistence lines using free energy techniques that employ for the most part MC simulations performed at constant particle number N, P and T, i.e., in the NPT ensemble [40]. Depending on the phase, the pressure is kept constant by changing the volume isotropically (for L, S, HDT and LDT), by allowing rectangular dimensions of the simulation cell to change length independently while maintaining a right angle (for A and Z), or by allowing the angle to change as well (as a check for all phases). The system sizes and box shapes are as follows: (L) $N = 1020$ and 986, square box; (S) $N = 1024$ square box, and $N = 992$ with rectangular box $L_y = 32L_x/31$; (HDT and LDT) $N = 986$, $L_y = 17\sqrt{3}L_x/29$; (A) $N = 952$, $L_y = 28(\sin 12^\circ + 1)L_x/(34\cos 12^\circ)$ initially; (Z) $N = 968$, square box initially. The different box shapes (and hence number of particles) are used as consistency checks, and indeed we do not detect any difference in the results based on the particular choice used.

3.3.2 Solid-liquid and solid-solid coexistence

First-order transition lines can be determined using a method developed by Kofke to trace coexistence curves [41, 42]. Kofke refers to his method as Gibbs-Duhem integration, and it is based on the Clapeyron equation which describes the temperature dependence of the pressure at which two phases coexist,

$$\frac{dP}{dT} = \frac{\Delta s}{\Delta v} = \frac{\Delta h}{T\Delta v}, \tag{3.1}$$

where Δs is the molar entropy difference, Δh is the molar enthalpy difference and Δv is the molar volume difference between the two coexisting phases. Tracing the coexistence curve requires that one point on the coexistence curve be known and

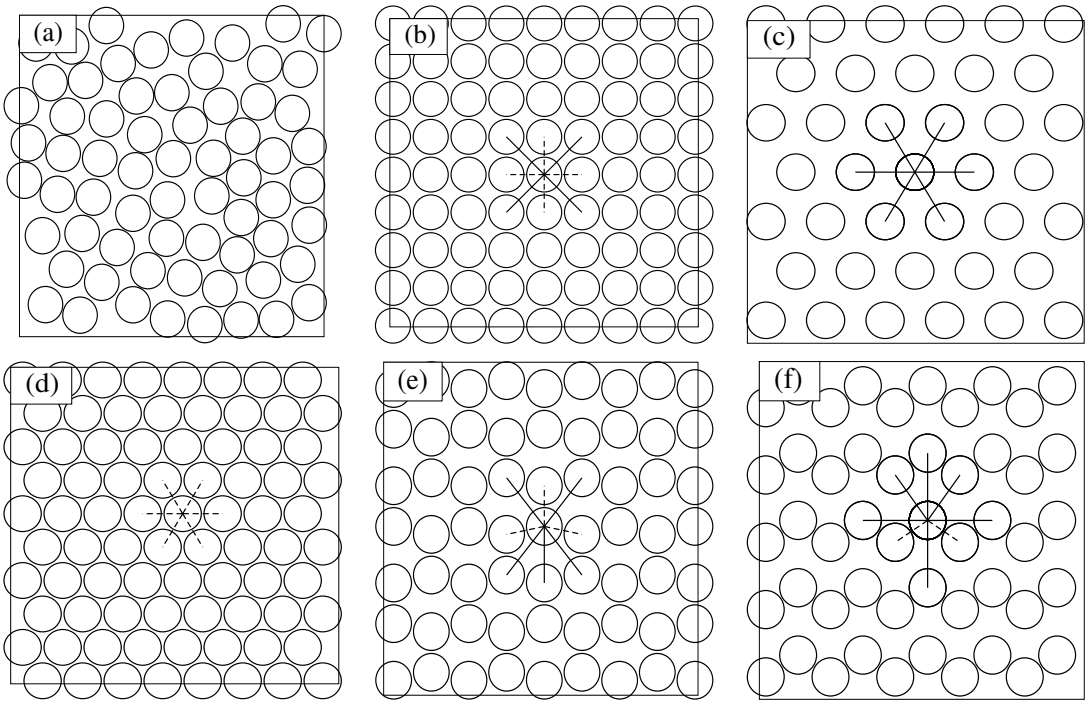

Figure 3.2: Illustration of the phases modelled: (a) the liquid (L), here shown as a small portion of a simulation in which distinct local packing environments are visible, (b) the square crystal (S), (c) the low-density triangular crystal (LDT), (d) the high-density triangular crystal (HDT), (e) the A crystal and (f) the Z crystal. Line segments for the crystal phases indicate a bond with energy $-\epsilon$ and a dashed line segment one with energy $-\epsilon/2$.

then the rest of the curve can be found by integration of Eq. 3.1, in particular using the enthalpy since it is much easier to calculate than the entropy. We carry out the integration using a second-order predictor-corrector method [43, 44].

To obtain the first coexistence point between the liquid and the S crystal, we first determine the respective equations of state along an isotherm by carrying out several NPT simulations. We choose $k_BT/\epsilon = 0.55$ so that we are above the L-G critical temperature, where k_B is the Boltzmann constant. Once the equations of state are known, we calculate the chemical potential μ for each phase as a function of number

density ρ by integrating the pressure via [40, 45],

$$\beta\mu(\rho) = \beta f(\rho^*) + \beta \int_{\rho^*}^{\rho} \frac{P(\rho')}{\rho'^2} d\rho' + \frac{\beta P}{\rho}, \tag{3.2}$$

where $\beta = (k_B T)^{-1}$ and f is the Helmholtz free energy per particle calculated at a reference number density ρ^*.

To carry out the integration, we fit the liquid isotherm to Eq. 3.3 and the solid isotherm to Eq. 3.4 [46, 47],

$$\begin{aligned} \beta P &= \frac{\rho}{1 - a_l\rho} + b_l \left(\frac{\rho}{1 - a_l\rho}\right)^2 + c_l \left(\frac{\rho}{1 - a_l\rho}\right)^3, & (3.3) \\ \beta P &= a_s\rho^2 + b_s\rho + c_s, & (3.4) \end{aligned}$$

where $a_{l,s}$, $b_{l,s}$, and $c_{l,s}$ are the fit parameters. Integration of Eq. 3.3 from zero to a density of interest yields the chemical potential of liquid, as given in Eq. 3.5. Similarly, integration of Eq. 3.4 from a reference density to the density of interest yields the chemical potential of solid, as given in Eq. 3.6 [46, 47],

$$\begin{aligned} \beta\mu_l(\rho) &= \ln\left(\frac{\rho\Lambda^2}{1 - a_l\rho}\right) + \frac{b_l/a_l - c_l/a_l^2 + 1}{1 - a_l\rho} \\ &+ \frac{c_l/2a_l^2 + b_l\rho}{(1 - a_l\rho)^2} + \frac{c_l\rho^2}{(1 - a_l\rho)^3} \\ &- (b_l/a_l - c_l/2a_l^2 + 1), & (3.5) \end{aligned}$$

$$\begin{aligned} \beta\mu_s(\rho) &= 2a_s\rho + b_s[\ln(\rho) + 1] \\ &- [a_s\rho^* + b_s \ln(\rho^*) - c_s/\rho^*] \\ &+ \beta f^{\text{ex}}(\rho^*) + \ln(\Lambda^2\rho^*) - 1, & (3.6) \end{aligned}$$

where $\Lambda = h/\sqrt{(2\pi m k_B T)}$ is the de Broglie thermal wavelength, where it is assumed to equal unity since it plays no rule in locating the coexistence pressure (along an isotherm). $f^{\rm ex}(\rho^*)$ is the excess Helmholtz free energy per particle calculated at ρ^*.

For the liquid, Eq. 3.3 provides a good fit only up to $\rho \approx 0.1$, and so from $\rho = 0$ to $\rho_l^* = 0.09418$ we use Eq. 3.5, and then integrate Eq. 3.2 numerically, using different interpolation orders to estimate uncertainty. The equations of state for the liquid and the S crystal are shown in Fig. 3.3.

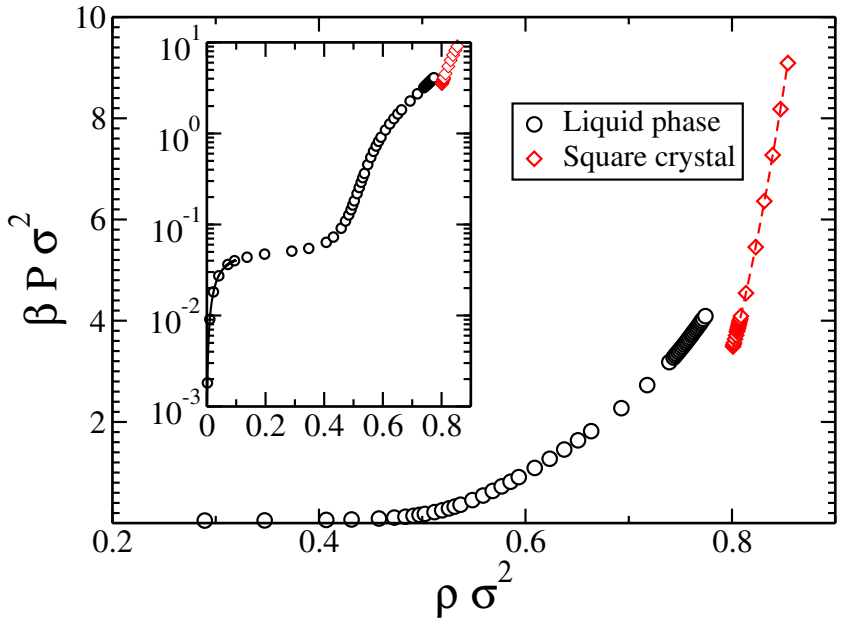

Figure 3.3: Equations of state of the liquid (circles) and S crystal (diamonds) at $k_B T/\epsilon = 0.55$. The curves show fits according to Eqs. 3.3 and 3.4, with $a_l = -0.457818$, $b_l = -9.18372$, and $c_l = 33.4007$ for the liquid (inset) and $a_s = 479.035$, $b_s = -686.583$, and $c_s = 246.067$ for the crystal.

We calculate the crystal reference Helmholtz free energy using the Frenkel-Ladd method [48]. In this method, a harmonic potential is added to the original system to define a new system potential energy,

$$U_\lambda = U(\vec{r}^N) + \lambda \sum_{i=1}^{N} (\vec{r}_i - \vec{r}_{0,i})^2, \tag{3.7}$$

where $\vec{r}_i$ is the position of particle i and $\vec{r}_{0,i}$ is its ideal lattice position, and $U(\vec{r}^N)$ is the unaltered system potential energy. U_λ is such that at coupling parameter $\lambda = 0$ the original model is recovered and for sufficiently large λ, the system behaves as an ideal Einstein crystal. A thermodynamic integration at a particular T and ρ is carried along λ to determine the Helmholtz free energy difference between the Einstein crystal and the original model. The excess free energy per particle for the model is then expressed as [40],

$$\begin{aligned} \beta f^{\text{ex}} &= \beta f_{\text{Ein}} + \frac{\beta \Delta F^{CM}}{N} + \frac{\ln(\rho^*)}{N} - \frac{d}{2N}\ln(N) \\ &- \frac{d}{2N}\ln\left(\frac{\beta\lambda_{\max} m}{2\pi}\right) - \beta f^{\text{id}}, \end{aligned} \tag{3.8}$$

where $d = 2$ is the dimensionality of the system, $m = 1$ is the mass of the particle. The first term in Eq. 3.8 represents the free energy of the ideal (non-interacting) Einstein crystal, which is equal to,

$$\beta f_{\text{Ein}} = \frac{\beta U(\vec{r}_0^N)}{N} - \frac{d}{2}\ln\left(\frac{\pi}{\beta\lambda_{\max}}\right), \tag{3.9}$$

where $U(\vec{r}_0^N)$ is the potential energy of the crystal when all the atoms are at their ideal lattice positions. $\lambda_{\max}$ is chosen such that, for λ larger than $\lambda_{\max}$, the mean-squared displacement $\langle \delta r^2 \rangle_\lambda \equiv \langle (\vec{r}_i - \vec{r}_{0,i})^2 \rangle_\lambda$, where $\langle \dots \rangle_\lambda$ indicates an ensemble average, for a system with fixed center of mass follows the following analytical expression,

$$\langle \delta r^2 \rangle_{\text{Eins},\lambda} = \frac{N-1}{N}\frac{1}{\beta\lambda}. \tag{3.10}$$

The second term in Eq. 3.8 represents the free energy difference between the solid and the Einstein crystal, and can be calculated by integrating the mean-squared displacement obtained from simulations carried out with a fixed center of mass as

follows [40, 49],

$$\frac{\Delta F^{\mathrm{CM}}}{N} = \int_0^{\lambda_{\max}} \langle \delta r^2 \rangle_\lambda d\lambda. \tag{3.11}$$

This integration can be understood as gradually switching on the coupling parameter to transform the solid into an Einstein crystal. For better accuracy, this integral can be transformed to [40],

$$\frac{\Delta F^{\mathrm{CM}}}{N} = \int_{\ln(c)}^{\ln(\lambda_{\max}+c)} d[\ln(\lambda + c)](\lambda + c)\langle \delta r^2 \rangle_\lambda, \tag{3.12}$$

where c is a constant chosen to be 1 in this work. The integrand is shown in Fig. 3.4, along with the curve for the ideal solid. We choose $\ln(\lambda_{\max} + 1) = 6.909$, checking that using higher values yields no appreciable change in the final result. The integration is carried out using interpolations of different order in order to estimate uncertainty.

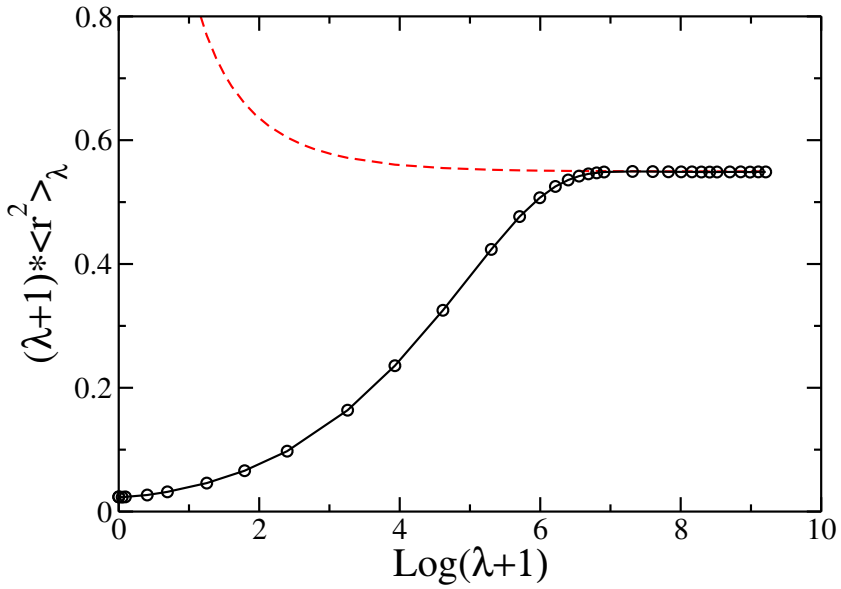

Figure 3.4: The mean-squared displacement transformed by Eq. 3.12 as a function of coupling parameter λ calculated by computer simulation (solid curve is a guide to the eye). Dashed line is the theoretical value given by Eq. 3.10.

The third, fourth and fifth terms in Eq. 3.8 correspond to the difference between the constrained (fixed center of mass) and unconstrained (non-fixed center of mass)

solids. The last term in Eq. 3.8 is the free energy of the ideal gas per particle, which is given by,

$$\beta f_{\mathrm{id}} = \ln(\rho) - 1 + \frac{\ln(2\pi N)}{2N}. \tag{3.13}$$

Once the chemical potentials of the two phases are known, the coexistence point can be obtained from the intersection of the two chemical potential curves [46, 47].

$\mu_l(\rho)$ and $\mu_s(\rho)$ are used together with the equations of state to plot the chemical potentials of the two phases as functions of pressure, as we do in Fig. 3.5. It is immediately apparent that $\mu(P)$ has nearly the same slope for both phases, and hence the location of the crossing is sensitive to errors in the various calculated quantities used to determine the curves. We note that the equations of state are determined only to the point where the metastable phase does not easily transform to the other phase. It is somewhat surprising that at the P for which either phase becomes unstable, $\beta P\sigma^2 \sim 3.49$ for S and $\beta P\sigma^2 \sim 4.09$ for L, the difference in chemical potential is very small, on the order of $|\beta\Delta\mu| \sim 0.01$. In the context of this work, we consider a phase as being unstable when the time to transformation is very short, i.e. the phase does not maintain metastability long enough to obtain precise average properties.

As a check on the L-S coexistence conditions at $k_BT/\epsilon = 0.55$, we perform an NVT (canonical ensemble) simulation with 10,000 particles initially placed on a square lattice with $\rho\sigma^2 = 0.786567$, the ρ at which the system is expected to phase separate into L and S with equal numbers of particles in each phase, based on liquid and S coexistence densities of $\rho_l = 0.7677$ and $\rho_x = 0.8064$, respectively. Fig. 3.6 shows a snapshot after running for 2×10^7 MC steps per particle, with dark symbols identifying particles belonging to the S phase [50–53]. Averaging over the last 5×10^6 MC steps per particle, the fraction of particles belonging to the S phase is 0.51.

The above procedure is repeated (at lower T) for the other crystal phases to determine crystal-crystal coexistence lines. For two crystals, the slopes of $\mu(P)$ are

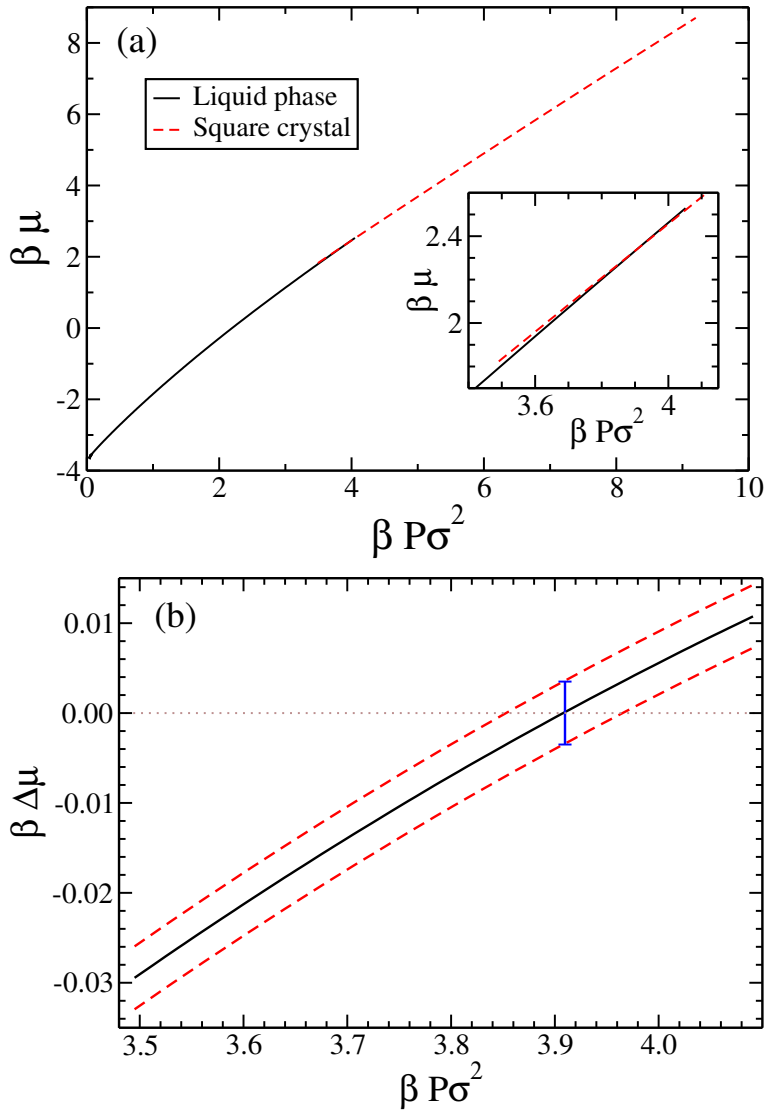

Figure 3.5: Determination of a coexistence P between the L and S phases at $k_BT/\epsilon = 0.55$. Panel (a) shows the chemical potential isotherms for the liquid (solid curve) and the square crystal (dashed curve). Inset shows a close-up of the crossing. In panel (b) we show the difference in chemical potential $\Delta\mu$ between the two phases over the entire range of P for which the equations of state overlap, with dashed lines indicating upper and lower uncertainty estimates.

generally quite different, which makes it easier to pinpoint the coexistence P. Similarly, at T less than the L-G critical temperature, the procedure is repeated to find crystal sublimation lines after determining the equation of state for the gas.

For the L-LDT melting line, we must additionally perform an integration of the

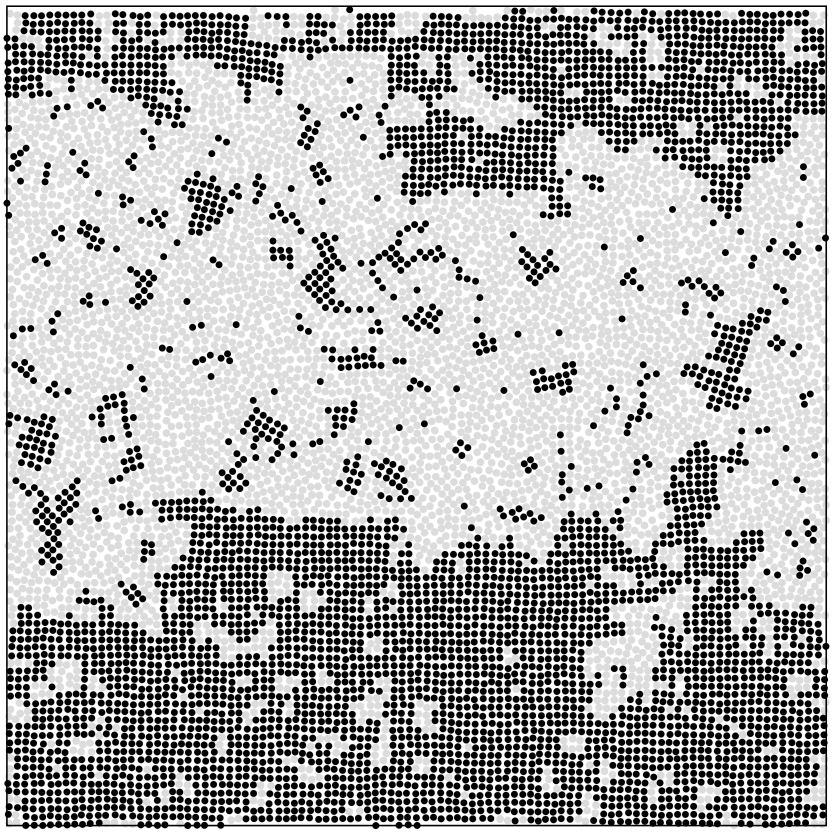

Figure 3.6: Snapshot configuration obtained from an NVT simulation for 10,000 particles at $k_BT/\epsilon = 0.55$ and $\rho = 0.786567$. Black symbols represent particles belonging to the S phase, while grey symbols represent the L phase.

enthalpy H to lower T at a P above the critical pressure in order to avoid the L-G critical point. Specifically, we first integrate the liquid equation of state at $k_BT/\epsilon = 0.70$ using Eq. 3.2 to $P\sigma^2/\epsilon = 0.05$, and then calculate $\mu(T)$ via [49],

$$\frac{\mu(T_2,P)}{k_BT_2} = \frac{\mu(T_1,P)}{k_BT_1} - \int_{T_1}^{T_2} \frac{H(T)}{Nk_BT^2} dT, \tag{3.14}$$

noting that here, the T dependence of Λ must be taken into account. Equivalently, this amounts to using the potential energy instead of the thermal energy in calculating H. For the LDT crystal, the reference free energy is calculated at $P\sigma^2/\epsilon = 0.05$ after determining the density at that pressure to be $\rho\sigma^2 = 0.4780 \pm 0.0015$. In Fig. 3.7 we

show $H(T)$ for L and LDT as well as the resulting difference in μ between the phases. We repeat the calculation using the liquid equation of state at $k_BT/\epsilon = 0.55$ as a check. Using the same procedure at $k_BT/\epsilon = 0.70$, we carry out an evaluation of the melting temperature of the S phase at $P\sigma^2/\epsilon = 0.15$ [Fig. 3.7(c)] and $P\sigma^2/\epsilon = 7.00$ as a check on the accuracy of the coexistence line. In the inset of Fig. 3.7(a), we plot H for L and LDT for a larger system of $\sim$ 4000 particles, detecting no appreciable difference in the value of H per particle or range of metastability from the $\sim$ 1000 particle system. We similarly detect no differences for the L-S transition when increasing the system size to 4000 particles (not shown).

3.3.3 L-HDT coexistence

Using the Gibbs-Duhem integration method is not necessary (or possible) for tracing out the L-HDT melting line at high T, as over a certain range in P the system can fairly easily sample both states. Thus, to determine the coexistence P along an isotherm, we first locate a pressure P_0 for which we can sample both states with reasonable statistics, as shown in Fig. 3.8, and determine the conditional Gibbs free energy from a histogram of the densities sampled during an NPT simulation,

$$\beta\Delta G(T, P_0; \rho) = -\ln\left[P_r(\rho)\right], \tag{3.15}$$

where $P_r(\rho)$ is the probability density of observing the system at a particular ρ. Here, we do not normalize our histograms as the normalization merely adds an inconsequential shift. P_0 already provides an estimate of the location of the coexistence pressure. The conditional free energy shown in Fig. 3.9 (black curve) exhibits a global minimum at high density (HDT) and a metastable one at low density (liquid). The free energy barrier between the two states is characteristic of a first order transition. To more

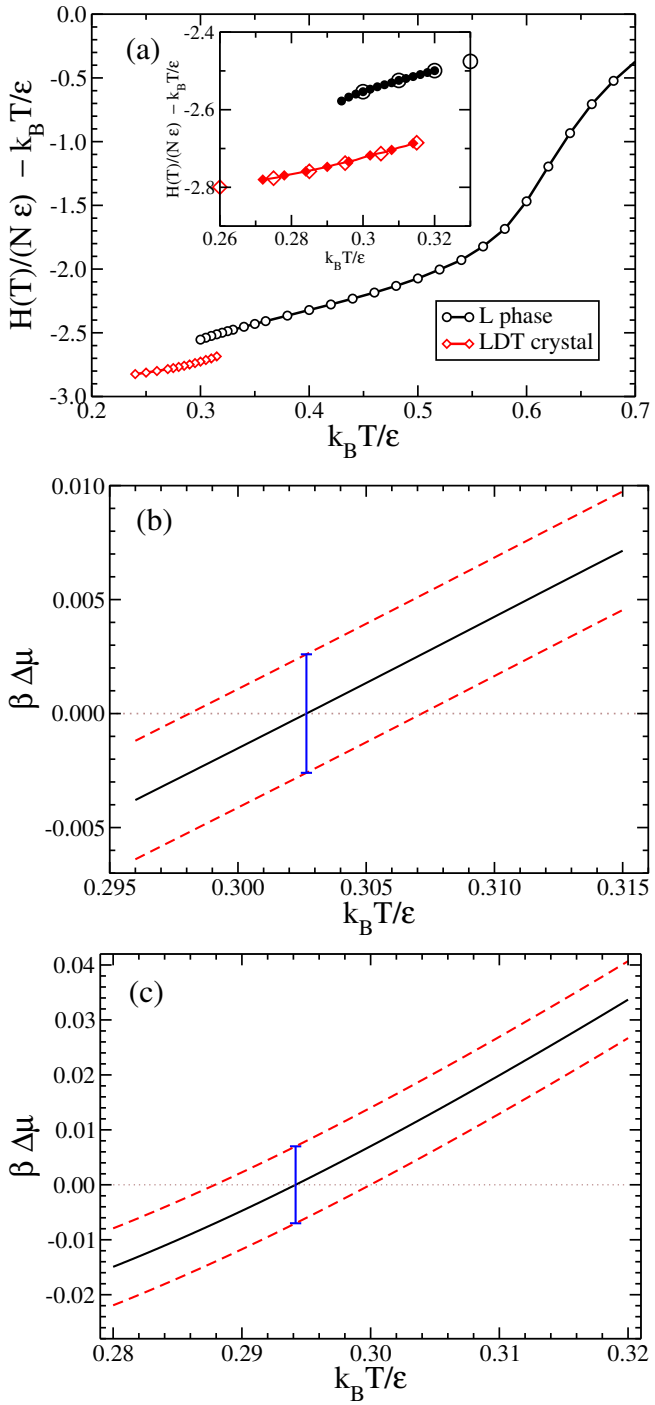

Figure 3.7: (a) Enthalpy per particle for the liquid (circles) and LDT crystal (diamonds) along $P\sigma^2/\epsilon = 0.05$. Here we have subtracted the ideal gas contribution to the energy. Inset shows data for a larger system of approximately 4000 particles (filled symbols). (b) The corresponding chemical potential difference between the L and LDT phases for the entire range in T of metastability. (c) The chemical potential difference between the L and S phases at $P\sigma^2/\epsilon = 0.15$.

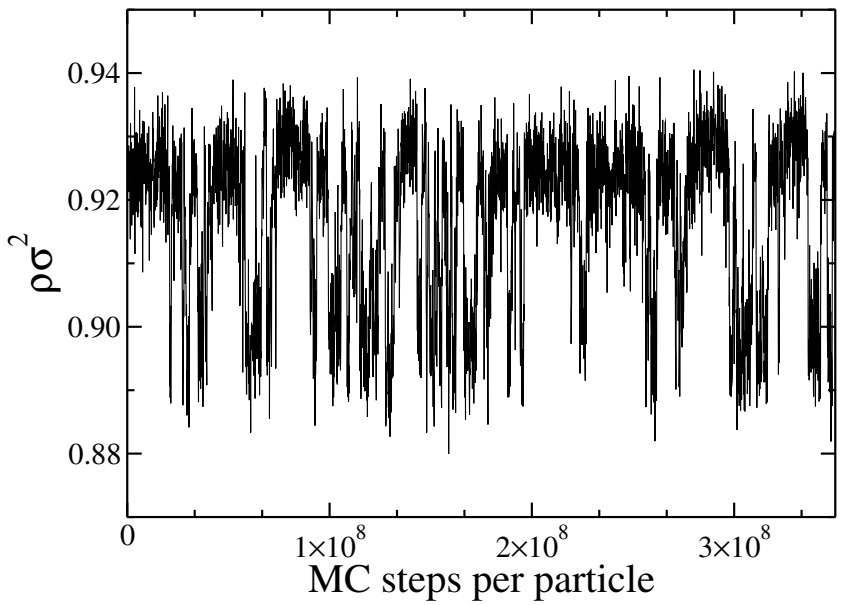

Figure 3.8: Sample time series of the number density near the L-HDT coexistence curve, with $N = 986$, $k_BT/\epsilon = 5.0$ and $P_0 = 50.0\epsilon/\sigma^2$. The system samples both the (lower density) liquid and the HDT crystal.

precisely locate the coexistence pressure, we reweight the histogram by applying a pressure shift,

$$\beta\Delta G(T, P'; \rho) = \beta\Delta G(T, P_0; \rho) + \frac{N\beta\Delta P}{\rho} + c, \tag{3.16}$$

where c is a constant related to normalization and ΔP is the pressure shift that brings the two minima to the same level, as in Fig. 3.9 (red curve). The coexistence pressure is then equal to $P' = P_0 + \Delta P$. In practice, the shift we obtain is hardly perceptible on the scale of our plots, e.g., for the $k_BT/\epsilon = 5.0$ case in Fig. 3.9, $P_0\sigma^2/\epsilon = 50.0$ and $\Delta P\sigma^2/\epsilon = -0.135$, and for $k_BT/\epsilon = 1.0$, $P_0\sigma^2/\epsilon = 14.350$ and $\Delta P\sigma^2/\epsilon = -0.004$. We note that the barrier does grow with decreasing T, and below $k_BT/\epsilon \approx 0.5$, both phases can stably exist for sufficiently long times in order to perform Gibbs-Duhem integration. Indeed below this T, it is not feasible to continue with histogram reweighting without using some biasing potential within the MC simulations.

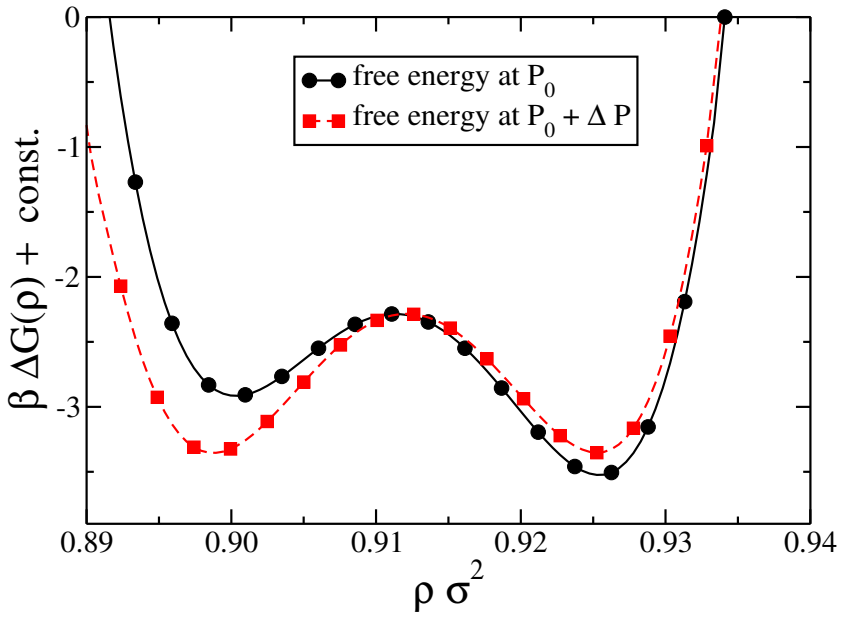

Figure 3.9: Conditional Gibbs free energy as a function of ρ. At $k_BT/\epsilon = 5.0$ and a pressure $P_0 = 50.0\epsilon/\sigma^2$ slightly above coexistence (solid curve, circles), the high density basin (HDT crystal) has a lower free energy than the low density (liquid) basin. Through Eq. 3.16, an appropriate shift in the pressure locates the coexistence pressure, i.e., transforms the P_0 curve so that the liquid and HDT minima are at the same level to within precision of the data (dashed line, squares).

3.3.4 G-L coexistence

The G-L coexistence line can be determined by using the Gibbs ensemble MC method developed by Panagiotopoulos [54]. The Gibbs ensemble employs two separated subsystems (without the presence of an interface), where the total number of particles is fixed and the total volume (in this case, area) of the two subsystems is also fixed; the total system as a whole evolves according to the canonical ensemble. The thermodynamic requirements for phase coexistence are that the temperature, pressure, and chemical potential of the two coexisting phases must be equal and these requirements can be achieved by performing three different kinds of trial MC moves. First, particle displacement within each subsystem, second, volume fluctuations of the two subsystems, and third, transferring particles between the two subsystems. The advantage

of using the Gibbs ensemble is that the system finds the densities of the coexistence phases without computing either the pressure or the chemical potential.

Having obtained the coexistence densities at a series of T, the corresponding coexistence pressures can be estimated by applying the virtual volume change method of Haresmiadis *et al* [55]. In this method, we perform separate NVT MC simulations of both the liquid and the gas at their respective coexistence densities (at a given T), and obtain the pressure via,

$$P = \frac{k_B T}{\Delta V} \ln \left[\left\langle \left(\frac{V'}{V} \right)^N \exp\left(-\beta \Delta U\right) \right\rangle \right], \tag{3.17}$$

where ΔU is the potential energy difference between a configuration with particle coordinates isotropically rescaled to accommodate a smaller virtual area V' and the unaltered configuration with original area V, where $V' = V - \Delta V$ and $\Delta V = 0.1\sigma^2$. Both phases give the same pressure to within error.

However, as the temperature approaches the critical temperature T_C, G-L coexistence can no longer be discerned in the Gibbs ensemble simulation. Our data for the G-L coexistence curve from the Gibbs ensemble extend only to $k_B T/\epsilon = 0.50$. Beyond this T, we extrapolate according to the following procedure. We estimate T_C by fitting the density difference of the two coexisting phases to a scaling law [40, 46, 56],

$$\rho_l - \rho_g = A|T - T_C|^{\beta_c}, \tag{3.18}$$

where β_c is the critical exponent, which is equal to 0.125 for a two-dimensional system, and A is a constant determined from the fit. To estimate the critical density ρ_C, we fit our results to the law of rectilinear diameters [40, 46, 56],

$$\frac{\rho_l + \rho_g}{2} = \rho_C + B|T - T_C|, \tag{3.19}$$

where B is a constant determined in the fit, and T_C is used from the fit in Eq. 3.18. The critical pressure P_C is estimated by fitting the vapor pressure curve to the Clausius-Clapeyron equation [56],

$$\ln P = C + \frac{D}{T}, \tag{3.20}$$

where C and D are constants determined in the fit. P_C is then calculated by substituting T_C obtained from Eq. 3.18 in Eq. 3.20. From the fits, we obtain $\rho_C\sigma^2 = 0.263 \pm 0.002$, $k_BT_C/\epsilon = 0.533 \pm 0.002$ and $P_C\sigma^2/\epsilon = 0.019 \pm 0.001$. The uncertainties quoted here are based on uncertainties in the fit parameters and do not reflect any systematic error associated with the fact that we are extrapolating above $k_BT/\epsilon = 0.50$, the highest T at which we have reliable Gibbs ensemble data.

3.4 Results

Having assembled all of the individual coexistence curves, we present the phase diagram in the P-T plane in Fig. 3.10 and in the ρ-T plane in Fig. 3.11. The three panels of Fig. 3.10 show progressively smaller ranges of P. In Fig. 3.10(b), dashed lines indicate metastable extensions of coexistence lines into the gas stability field (i.e., showing the phase diagram in the absence of the gas when there is a metastable condensed phase). As an aid to interpreting Fig. 3.11, we recall that under conditions of constant volume, the thermodynamic ground state is not necessarily a single phase, but is generally composed of two coexisting phases. The bottom panel of Fig. 3.11 shows the phase diagram in the absence of the gas phase.

Fig. 3.10(a) shows a prominent S-L melting line temperature maximum at $P\sigma^2/\epsilon = 5.24 \pm 0.05$ and $k_BT_{\max}/\epsilon = 0.655 \pm 0.005$. At this point, according to Eq. 3.1, the molar volumes of the S crystal and liquid are equal. At higher P, the melt is more dense than the crystal, as in the familiar case of water and hexagonal ice.

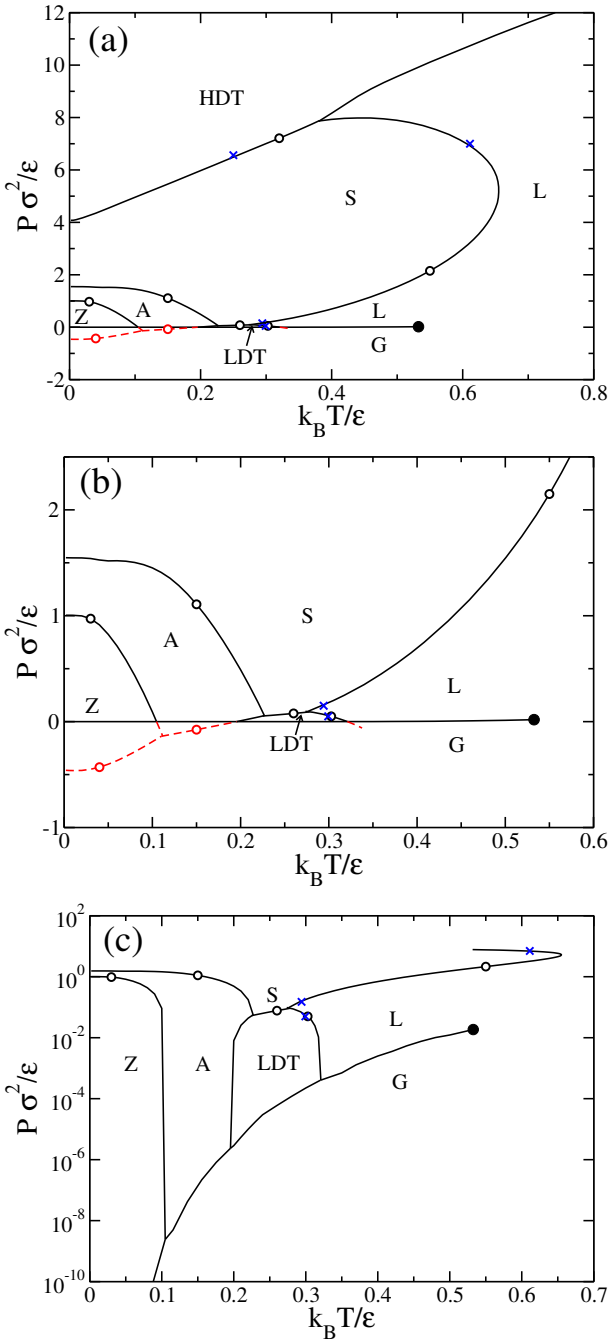

Figure 3.10: Phase diagram of the 2D model in the P-T plane, showing the liquid (L), gas (G) and crystal phases HDT, S, LDT, A and Z (see Fig. 3.2). The panels show portions of the phase diagram at (a) high, (b) medium and (c) low P. The liquid-gas coexistence line terminates at a critical point at $k_B T_c/\epsilon = 0.533$ and $P_C\sigma^2/\epsilon = 0.0185$ (filled circle). Dashed lines in (b) are metastable coexistence lines assuming the absence of the gas phase. Initial coexistence points, i.e., starting points for Gibbs-Duhem integration, are indicated by circles, while $\times$'s show repeated coexistence calculations done as checks on the Gibbs-Duhem integration.

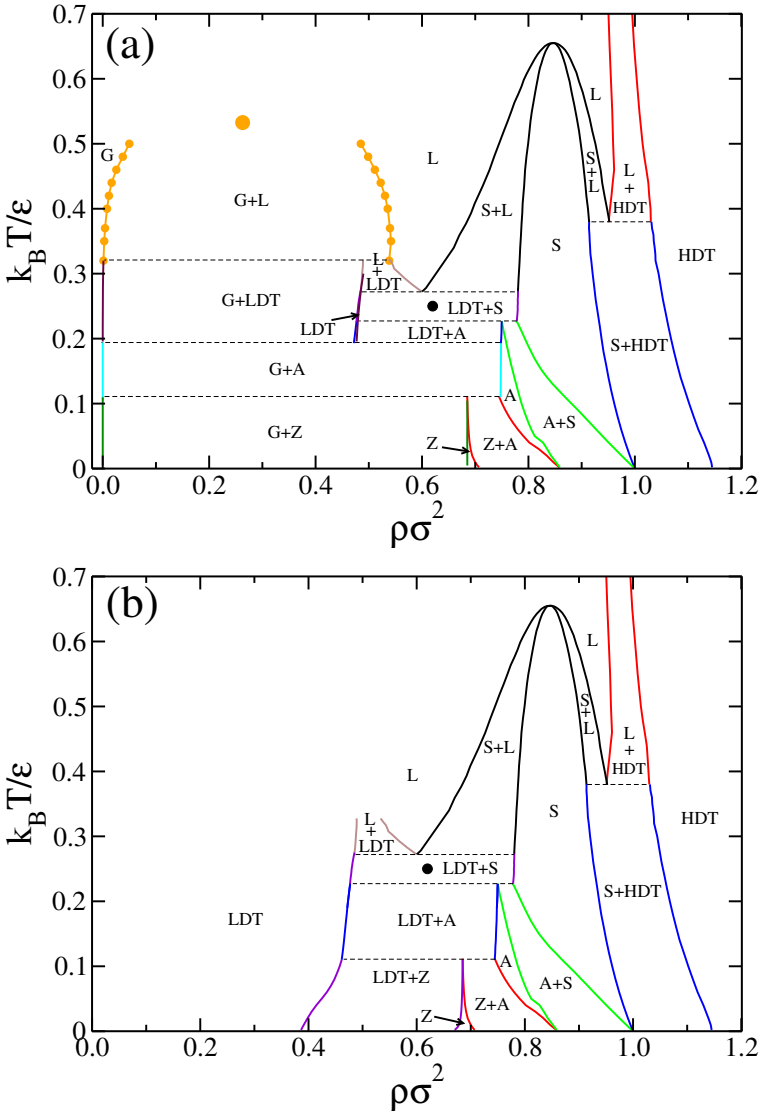

Figure 3.11: Phase diagram in the ρ-T plane. (a) The points along the G-L coexistence lines indicate results from Gibbs ensemble simulations and the large filled orange circle shows our estimate of the G-L critical point based on an extrapolation described in the text. Panel (b) shows the phase diagram in the absence of the gas phase. The filled black circle shows the location of the obscured L-L critical point discussed in Ref. [39].

An even more exotic feature of the S-L melting line is the pressure maximum occurring near the HDT-S-L triple point at $P_{\max}\sigma^2/\epsilon = 7.98 \pm 0.08$ and $k_BT/\epsilon = 0.450 \pm 0.003$. A close-up of this feature is shown in Fig. 3.12. At this point, according to Eq. 3.1, the entropy of the S crystal and the liquid are equal, and for lower T along

the curve, the melt has a *lower* entropy than the crystal. The presence of the pressure maximum in the melting curve allows for "inverse melting" [57] in the narrow range of P between the triple point and the maximum, i.e. isobaric heating of the liquid results in crystallization.

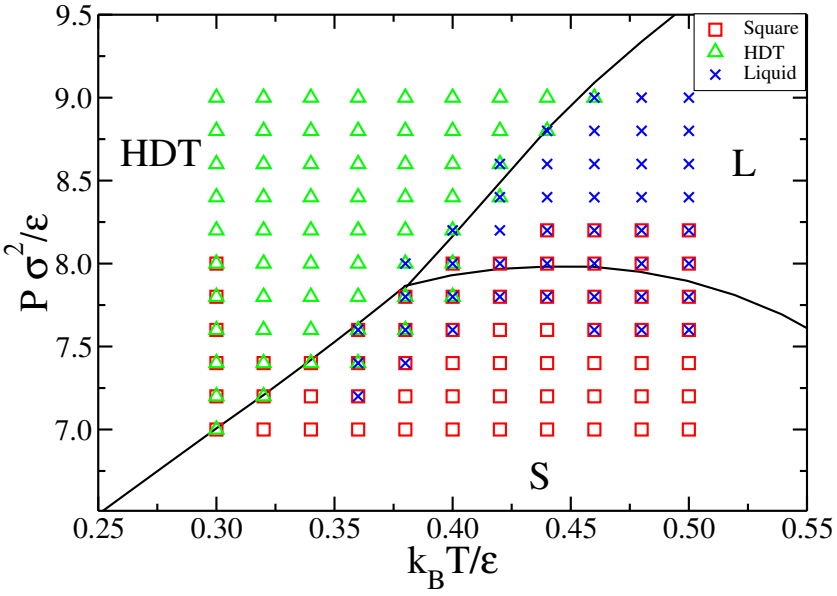

Figure 3.12: P-T phase diagram obtained at high pressure, near the L-S-HDT triple point. The grid of points is obtained from three sets of simulations. Each of L, S and HDT is used to initialize a simulation set with $N = 986$, 992 and 986, respectively. The final phase adopted from each set at each state point is indicated by a symbol: S, square; HDT, triangle; L, $\times$. E.g., at low P and high T, both L and HDT transform to S, while near the triple point, each phase retains metastability.

Given the numerical uncertainties in determining coexistence conditions and tracing out coexistence lines, we carry out a rough check by performing three sets of simulations in the vicinity of the HDT-S-L triple point. Each set is a grid of 121 simulations for state points marked in Fig. 3.12. For one set, the particles are initially positioned on the S lattice; for the second set, points are initially on the HDT lattice; high T liquid state configurations seed the third set of simulations. We run each simulation for 5×10^7 MC steps per particle, and then indicate with the appropriate symbol in Fig. 3.12 the phase which the system spontaneously adopts. Potentially, since there

are three simulations per state point, three symbols may appear, indicating stability or metastability of all three phases. Near the triple point, the simulations retain the starting phase, as expected, while deep within a stability field, all sets transform to the same phase. In this way, we crudely map out the extent of metastability. At $k_BT/\epsilon = 0.30$, metastability of S is enhanced as the dynamics become slow.

It is difficult to directly confirm inverse melting on typical simulation time scales, as the metastable phase is never far from the coexistence line. We aim to address this in future work. However, and while this is not a definitive check on the existence of inverse melting, the tendency for points exhibiting liquid metastability within the S stability field to track the curvature of the S-L melting line is supportive of the existence of this phenomenon in the system, i.e., the lowest P point for each T for which the $\times$ and $\circ$ simultaneously occur roughly form a curve with a maximum in P that tracks the shape of the S-L coexistence line.

At lower P, we confirm the negative slope of the LDT-L melting line as reported already in Ref. [39]. Below the LDT-S-L triple point, we find that the new crystal phases A and Z both have reasonably large stability fields, as shown in Fig. 3.10(b), and that the LDT crystal, having the lowest density of the crystal phases studied, occupies a rather small portion of the phase diagram. The A-S transition line is also negatively sloped, which together with the fact that the A phase has a lower density than S (see Fig. 3.11), implies through Eq. 3.1 that the entropy of S is larger than that of A. Indeed, the bonding distances required to form A are rather restrictive compared to the geometry of S, and this is reflected in the smaller range in ρ for which A is the single stable phase (again, compared to S). A similar argument holds when comparing Z to A.

The nature of phases A and Z is somewhat reminiscent of the low density phases appearing in soft shoulder models [33, 34], in that in both cases the system sacrifices

entropy in favor of lower energy at low T by effectively increasing the particle size to the soft diameter. Here, however, the particular low energy bond length allows the system to form particle geometries that progressively lower the energy. That there are several low density crystals is also reminiscent of water and silica.

In Ref. [39], the authors locate lines in the P-T plane that demarcate a limit to observing the liquid, i.e., where crystallization is practically unavoidable. Although their investigation into this aspect of the model was not exhaustive, the character of crystallization was possibly suggestive of continuous crystallization seen in other two dimensional systems. We plot these lines within the appropriate portion of our calculated phase diagram in Fig. 3.13. We see that the crystallization lines occur below our calculated first-order melting lines, and therefore occur at conditions for which there is a gap in crystal and liquid chemical potential. However, this does merit a closer look at the crystallization process, especially near the apparent limit of liquid metastability. Also in Fig. 3.13, we plot the location of what might be termed the obscured L-L critical point at low T that appears to be responsible for the liquid anomalies reported in Ref. [39], but which is unobservable owing to unavoidable nucleation. Within uncertainty, this obscured critical point falls on the S-LDT coexistence line.

We estimate the density of the obscured critical point from the pressure isochores reported in Ref. [39], and plot the location in the ρ-T plane in Fig. 3.11. We see that it falls within the coexistence region of two crystals of significantly different ρ, S and LDT. This is similar to the case of, e.g., the TIP4P2005 model of water [58,59] and is consistent with the idea that L-L phase separation is possible when there is a strong coupling between energy and density [60].

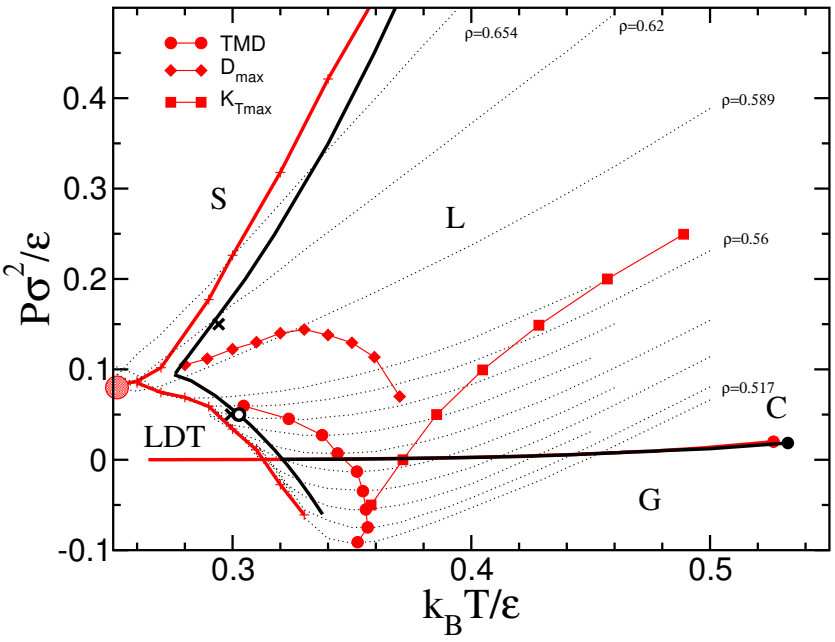

Figure 3.13: Comparison of our phase diagram with previously reported system properties. Red curves are taken from Ref. [39] and represent crystallization lines (+), locus of temperatures of maximum density along isobars (TMD, circles), pressures of maximum diffusivity along isotherms ($D_{\max}$, diamonds), maxima of isothermal compressibility (K_{Tmax}, squares) and G-L coexistence. Also shown are the G-L critical point (filled red circle) and the obscured L-L critical point (large hashed circle). Dotted lines show pressure along isochores. All other symbols as in Fig. 3.10. We note that we determine the location of the G-L critical point from an extrapolation of data above $k_BT/\epsilon = 0.50$, while the one reported in Ref. [39] is based on inflection points of pressure isotherms. The previously reported crystallization lines fall within the presently calculated crystal stability fields.

3.5 Discussion

We calculate the coexistence temperature (along an isobar) or pressure (along an isotherm) of two phases by determining the point at which the chemical potential of those two phases cross, and estimate the uncertainty by accounting for the numerical error, typically arising from an integration, in evaluating the various terms in, e.g., Eq. 3.2, 3.12 and 4.4. The errors mostly result in a constant shift in the curves that, given the small difference in slopes of $\mu(P)$ or $\mu(T)$ between the liquid and crystal phases, can lead to a large uncertainty in the crossing. As a check, after calculating the

coexistence curve through Gibbs-Duhem integration, for the L-S case for example, we determine two additional chemical potential crossings along different thermodynamic paths and the results show good consistency with the Gibbs-Duhem curve. Another indicator of the quality of the results is the degree to which coexistence lines cross at the L-S-HDT and L-S-LDT triple points.

Having said this, shifts in the $\mu(P)$ or $\mu(T)$ curves do not affect the slopes, which show in general the first-order character of the L-S or L-LDT transitions. For a given phase, we determine μ to the point where it is simple to determine the equilibrium properties of that phase, i.e., to the point where spontaneous transformation does not readily occur on the timescale of simulation. We note that for the liquid to crystal transitions, the chemical potential difference between the liquid and crystal at which metastability is no longer easily attainable is rather small in comparison to other studies [61]. Perhaps this is a feature of two-dimensional systems, but nonetheless implies a very small surface tension if the classical description of nucleation is valid.

The L-LDT and L-S crystallization lines in Ref. [39], as noted earlier, were dynamically determined as maximal extents of the liquid's ability to exist, and we show here that they indeed occur in the metastable liquid. The loss of liquid metastability prevents observing any low and high density liquids that would exist below the proposed L-L critical point because these limit lines radiate from the critical point towards higher T. We would like to explore the process of crystallization in this vicinity. If indeed the L-L critical point proposed for this system is obscured by nucleation induced through critical fluctuations, studying nucleation in the present model may help better understanding what may be occurring in water [62].

Notably, for the model at higher P, we provide evidence for inverse melting, arising from a maximum in P in the L-S coexistence line. This phenomenon is rare, and seeing evidence for it in such a simple system will allow for deeper exploration

into the basic physics surrounding it.

The freezing of the liquid to the close-packed solid, i.e., the L-HDT transition, appears to be first-order for all T that we have explored. For our system size, the free energy barrier between the L and HDT basins with ρ as the order parameter at $k_BT/\epsilon = 5.0$ and $P = 50.0\epsilon/\sigma^2$ is just above $1k_BT$. In the high T limit when the system should behave as hard disks, Mak [63] and Bernard and Krauth [64] have provided evidence that the transition should be also first-order. Lowering T, the barrier grows and reaches a value of $\sim 2.4k_BT$ at a simulation conducted on our coexistence line at $k_BT/\epsilon = 0.50$ and $P\sigma^2/\epsilon = 9.5649$ with $N = 986$, thus becoming more strongly first-order. A careful search for the hexatic phase near the HDT melting line is very much warranted, particularly at high T, as Bernard and Krauth's rather impressive work appears to establish a first-order transition between the liquid and hexatic (not crystal) phase in hard disks, and that the hexatic phase exists only for a very narrow range of densities. Our initial search for the hexatic phase through discrete molecular dynamics simulations at constant P of 65536 particles for $k_BT/\epsilon \leq 5.0$ along the HDT melting line, as well as at points near the L-S and L-LDT transition lines has not yet yielded evidence for the hexatic phase, namely an orientational correlation function that decays with distance as a power-law with a sufficiently small exponent [65]. It would seem then, that if it exists, the presence of the hexatic phase would not affect our phase diagram in a significant way. Interestingly, Bernard and Krauth did not establish a power-law decay of the orientational correlation function within the hexatic phase. We hope to report on this more thoroughly in the future.

3.6 Conclusions

We compute a phase diagram using various free energy techniques of a two-dimensional SSSW model that has been previously shown to exhibit liquid-state anomalies often associated with the presence of a metastable L-L critical point [18]. We find two low-T crystal phases not previously reported. All transitions, including melting lines, appear to be first-order for our system size of ~ 1000 particles. Thus, it appears that the liquid anomalies present in the system do not arise as a result of quasi-continuous freezing, as has been previously suggested [66]. Previously reported crystallization lines fall within respective phase stability regions reported here. Interestingly, the difference in chemical potential between liquid and crystal phases at the limit where the metastable phase can be readily observed is rather small, $\beta\Delta\mu \sim 0.01$.

The L-S coexistence curve exhibits both a maximum temperature, indicating that at higher pressure the crystal is less dense than the melt, and a pressure maximum, which means that inverse melting should occur in a specific pressure range. Given the scarcity of systems exhibiting inverse melting, the present model presents the opportunity to study this rare phenomenon in more detail.

Acknowledgments

AMA and IS-V thank NSERC for funding, ACEnet for funding and computational support and CFI for funding of computing infrastructure. SVB acknowledges the partial support of this research through the Dr. Bernard W. Gamson Computational Science Center at Yeshiva College.

Bibliography

[1] P. C. Hemmer and G. Stell, Phys. Rev. Lett. **24**, 1284 (1970).

[2] G. Stell and P. C. Hemmer, J. Chem. Phys. **56**, 4274 (1972).

[3] J. S. Hoye and P. C. Hemmer, Physica Norvegica **7**, 1 (1973).

[4] K. K. Mon, N. W. Ashcroft, and G. V. Chester, Phys. Rev. B **19**, 5103 (1979).

[5] M. Selbert and W. H. Young, Phys. Lett. **58** A, 469 (1976).

[6] D. Levesque and J. J. Weis, Phys. Lett. **60** A, 473 (1977).

[7] J. M. Kincaid and G. Stell, Phys. Lett. **65** A, 131 (1978).

[8] P. T. Cummings and G. Stell, Mol. Phys. **43**, 1267 (1981).

[9] A. Voronel, I. Paperno, S. Rabinovich, and E. Lapina, Phys. Rev. Lett. **50**, 247 (1983).

[10] K. K. Mon, N. W. Ashcroft, and G. V. Chester, J. Phys. F **15**, 1215 (1985).

[11] E. Velasco, L. Mederos, G. Navascues, P. C. Hemmer, and G. Stell, Phys. Rev. Lett. **85**, 122 (2000).

[12] C. H. Cho, S. Singh, and G. W. Robinson, Phys. Rev. Lett. **76**, 1651 (1996).

[13] M. R. Sadr-Lahijany, A. Scala, S. V. Buldyrev, and H. E. Stanley, Phys. Rev. Lett. **81**, 4895 (1998).

[14] M. R. Sadr-Lahijany, A. Scala, S. V. Buldyrev, and H. E. Stanley, Phys. Rev. E **60**, 6714 (1999).

[15] E. A. Jagla, J. Chem. Phys. **111**, 8980 (1999).

[16] E. A. Jagla, Phys. Rev. E **63**, 061501 (2001).

[17] E. A. Jagla, Phys. Rev. E **63**, 061509 (2001).

[18] A. Scala, M. R. Sadr-Lahijany, N. Giovambattista, S. V. Buldyrev, and H. E. Stanley, Phys. Rev. E **63**, 041202 (2001).

[19] T. Head-Gordon and F. H. Stillinger, J. Chem. Phys. **98**, 3313 (1993).

[20] F. H. Stillinger and T. Head-Gordon, Phys. Rev. E **47**, 2484 (1993).

[21] P. H. Poole, F. Sciortino, U. Essmann, and H. E. Stanley, Nature **360**, 324 (1992).

[22] E. Rapoport, J. Chem. Phys. **46**, 2891 (1967).

[23] V. V. Brazhkin, S. V. Popova, and R. N. Voloshin, High Pressure Res. **15**, 267 (1997).

[24] M. J. Cuthbertson and P. H. Poole, Phys. Rev. Lett. **106**, 115706 (2011).

[25] V. V. Vasisht, S. Saw, and S. Sastry, Nat. Phys. **7**, 549 (2011).

[26] J. N. Glosli and F. H. Ree, Phys. Rev. Lett. **82**, 4659 (1999).

[27] G. Franzese, G. Malescio, A. Skibinsky, S. V. Buldyrev, and H. E. Stanley, Nature **409**, 692 (2001).

[28] S. V. Buldyrev, G. Malescio, C. A. Angell, N. Giovambattista, S. Prestipino, F. Saija, H. E. Stanley, and L. Xu, J. Phys.: Condens Matter, **21**, 504106 (2009).

[29] U. Gasser, J. Phys.: Condens. Matter **21**, 203101 (2003).

[30] P. J. Camp, Phys. Rev. E **68**, 061506 (2003).

[31] H. M. Gibson and N. B. Wilding, Phys. Rev. E **73**, 061507 (2006).

[32] V. N. Ryzhov and S. M. Stishov, Phys. Rev. E **67**, 010201 (R) (2003).

[33] Y. D. Fomin, N. V. Gribova, V. N. Ryzhov, S. M. Stishov, and D. Frenkel, J. Chem. Phys. **129**, 064512 (2008).

[34] N. V. Gribova, Y. D. Fomin, D. Frenkel, and V. N. Ryzhov, Phys. Rev. E **79**, 051202 (2009).

[35] C. J. Roberts and Pablo G. Debenedetti, J. Chem. Phys. **105**, 658 (1996).

[36] C. Buzano and M. Pretti, J. Chem. Phys. **119**, 3791 (2003).

[37] C. Buzano, E. De Stefanis, and M. Pretti J. Chem. Phys. **129**, 024506 (2008).

[38] N. G. Almarza, J. A. Capitán, J. A. Cuesta, and E. Lomba J. Chem. Phys. **131**, 124506 (2009).

[39] S. V. Buldyrev, G. Franzese, N. Giovambattista, G. Malescio, M. R. Sadr-Lahijany, A. Scala, A. Skibinsky, and H. E. Stanley, Physica A **304**, 23 (2002).

[40] D. Frenkel and B. Smit, *Understanding Molecular Simulation: From algorithms to Applications*, San Diego, Academic Press, 2002.

[41] D. A. Kofke, Mol. Phys. **78**, 1331 (1993).

[42] D. A. Kofke, J. Chem. Phys. **98**, 4149 (1993).

[43] M. H. Lamm and C. K. Hall, AIChE J. **50**, 215 (2004).

[44] The algorithm used is $P_{i+1} = P_i + \Delta T(f_i + f_{i+1})/2$, where f_i is the right hand side of Eq. 3.1, the evaluation of which requires one NPT MC simulation for each phase at temperature T_i and pressure P_i. Alternatively, we iterate $T_{i+1} = T_i + \Delta P(1/f_i + 1/f_{i+1})/2$. This is especially useful in the vicinity of the melting temperature maximum of the S-L coexistence curve.

[45] C. Vega and E. G. Noya, J. Chem. Phys. **127**, 154113 (2007).

[46] Massimo G. Noro, and D. Frenkel, J. Chem. Phys. **114**, 2477 (2001).

[47] D. L. Pagan and J. D. Gunton, J. Chem. Phys. **122**, 184515 (2005).

[48] D. Frenkel and A. J. C. Ladd, J. Chem. Phys. **81**, 3188 (1984).

[49] C. Vega, E. Sanz, J. L. F. Abascal, and E. G. Noya, J. Phys.: Condens Matter, **20**, 153101 (2008).

[50] P. R. ten Wolde, M. J. Ruiz-Montero, and D. Frenkel, J. Chem. Phys. **104**, 9932 (1996).

[51] A. M. Almudallal and I. Saika-Voivod, Phys. Rev. E **84**, 011402 (2011).

[52] I. Saika-Voivod, P. H. Poole, and R. K. Bowles, J. Chem. Phys. **124**, 224709 (2006).

[53] The solid particles have been identified using the method developed by Frenkel and co-workers [50]. For each particle we define the quantity $q_{lm}(i) = 1/N_b(i) \sum_{j=1}^{N_b(i)} Y_{lm}(\hat{r}_{ij})$, where the sum is carried out over all neighboring particles $N_b(i)$ that are within a distance $\sqrt{2}/a$, and $Y_{lm}(\hat{r}_{ij})$ are the spherical

harmonics calculated for the normalized direction vector $\hat{r}_{ij}$ between the neighbors. The unit vector $\hat{r}_{ij}$ is determined by the polar and azimuthal angles $\theta_{ij} \equiv \pi/2$ and ϕ_{ij}. Since our crystallites possess square symmetry, we use $l = 4$. For each pair of neighboring particles i and j, we calculate the correlation $\sum_{m=-4}^{4} \hat{q}_{4m}(i)\hat{q}^{*}_{4m}(j)$, where $\hat{q}_{4m} = q_{4m}(i)/[\sum_{m=-4}^{4} |q_{4m}(i)|^2]^{1/2}$ and q^* is the complex conjugate of q. If the correlation between two neighboring particles is greater than 0.9, then particles i and j are considered to be connected. If a particle has at least three connected neighbors, then it is considered a solid particle.

[54] A. Z. Panagiotopoulos, Mol. Phys. **61**, 813 (1987).

[55] V. I. Harismiadis, J. Vorholz, and A. Z. Panagiotopoulos, J. Chem. Phys. **105**, 8469 (1996).

[56] L. Vega, E. de Miguel, L. F. Rull, G. Jackson, and I. A. Mclure, J. Chem. Phys. **96**, 2296 (1992).

[57] F. H. Stillinger and P. G. Debenedetti, Biophys. Chem. **105**, 211 (2003).

[58] J. L. F. Abascal, E. Sanz, and C. Vega, Phys. Chem. Chem. Phys, **11**, 556 (2009).

[59] J. L. F. Abascal and C. Vega, J. Chem. Phys, **133**, 234502 (2010).

[60] F. Sciortino, I. Saika-Voivod, and P. H. Poole, Phys. Chem. Chem. Phys. **13**, 19759 (2011).

[61] I. Saika-Voivod, F. Romano, and F. Sciortino, J. Chem. Phys. **135**, 124506 (2011).

[62] E. B. Moore and V. Molinero, Nature **479**, 506 (2011).

[63] C. H. Mak, Phys. Rev. E **73**, 065104(R) (2006).

[64] E. P. Bernard and W. Krauth, Phys. Rev. Lett. **107**, 155704 (2011).

[65] P. Keim, G. Maret, and H. H. von Grünberg, Phys. Rev. E **75**, 031402 (2007).

[66] N. B. Wilding and J. E. Magee, Phys. Rev. E **66**, 031509 (2002).

Chapter 4

Inverse melting in a two-dimensional off-lattice model

4.1 Abstract

We carry out computer simulations of a simple, two-dimensional off-lattice model that exhibits inverse melting. The monodisperse system comprises core-softened disks interacting through a repulsive square shoulder located inside an attractive square well. By systematically varying the potential parameters, we increase the pressure range over which the liquid freezes to a crystal upon isobaric heating. The effect is largely controlled by the extent of the shoulder. Despite occurring in two dimensions, the melting transition is first order and to a liquid, rather than to a hexatic or quasicrystal phase. We also provide comment on a commonly employed correlation function used

to determine the degree of translational ordering in a system.

4.2 Introduction

Inverse melting is the curious phenomenon in which a crystal melts upon isobaric cooling, or equivalently, a liquid freezes upon heating. Only a handful of systems exhibit this rare behavior [1]. While the effect is inherently fascinating, recent theoretical work on DNA-coated colloids points to inverse melting as a way to overcome kinetic trapping at low temperature T, thus providing alternate pathways in the synthesis of novel materials [2, 3].

Notable examples of materials exhibiting inverse melting are ^{3}He [4] and ^{4}He [5,6], for which the liquid is stabilized at low T by quantum mechanical effects, and polymers poly(4-methylpentene-1) [7–10] and syndiotactic polystyrene [11]. Motivated by He and polymers, Feeney and coworkers devised a model that successfully recovers inverse melting by coupling internal degrees of freedom of a particle with interparticle interactions [12]. A lattice model for which the ferromagnetic phase receives an energetic penalty but is given a higher degeneracy also recovers inverse melting [13]. Other cases of inverse melting and behavior similar to it are the nematic to smectic-A transition achieved upon heating the liquid crystal 4-cyano-4′-octyloxybiphenyl [14]; crystallization of micelles of triblock copolymer PEO-PPO-PEO upon heating, brought about by an increase in effective packing fraction as T increases [15]; the multicomponent solution of a-cyclodextrine, water, and 4-methylpyridine [16–18] in which hydrogen bond rearrangements play a role; Nb-Cr alloys, which again are multicomponent solutions; and the melting of the ordered vortex phase in a high-temperature superconductor [19, 20].

The idea of inverse melting is also linked conceptually to the glass transition. It

was pointed out by Kauzmann [21] that in many cases, the behaviour of a liquid cooled progressively below its freezing T extrapolates to the thermodynamically exotic case of the liquid's entropy becoming lower than that of the crystal. Before this point is reached, the glass transition, a kinetic phenomenon, intervenes, implicating entropy as a controlling factor in liquid dynamics. Inverse melting, however, requires that the crystal have a higher entropy than the liquid's over a range of thermodynamic conditions, a conclusion reached upon considering slopes of melting lines in the pressure (P)-T plane [1]. So while systems exhibiting inverse melting provide a counter-example to the importance of excess entropy to dynamics, they do provide the intriguing case in which a crystal may be quenched into a kinetically trapped metastable state, an ordered version of a glass [22]. Further, one may wish to explore the possible connection between inverse melting and glassy dynamics achieved upon heating [23].

What would enhance the current body of work on inverse melting is a simple off-lattice model that exhibits the phenomenon and is amenable to simulation. Recently, we reported inverse melting for a double-step potential consisting of a square shoulder within a square well (SSSW), shown in Fig. 4.1, while calculating the phase diagram for the model in two dimensions [Fig. 4.2(a)] [24]. The difficulty is that the effect is very weak, and we did not provide direct evidence for the existence of the phenomenon to confirm the Monte Carlo-based free energy calculations used to determine phase boundaries.

In our present study, we tune the parameters of the model in a systematic way in order to greatly expand the region in the P-T plane over which inverse melting takes place. Having enlarged the effect, we probe it with complementary techniques, including event-driven molecular dynamics (EDMD) simulations, to confirm its existence. EDMD is suitable for simulating step potentials, for which particles experience

no forces between impulsive collisions or "events". Since in two dimensions there is the possibility of continuous melting through a hexatic-type phase we further provide evidence that the transition is first order between a liquid and crystal. Further, a quasicrystal phase for a similar potential has been reported [25], but we do not see such a phase.

The SSSW potential we study here falls into the category of core-softend potentials introduced by Stell and Hemmer [26,27] as model systems exhibiting multiple fluid or iso-structural solid transitions and critical points [28, 29]. Such potentials were used to study liquid metals [30–35], for which experimental evidence exists for novel critical behaviour [36]. Research into explaining the many anomalous properties of water [37–40], particularly through a hypothesized second critical point in the deeply metastable state [41], has also drawn benefit from studies of core-softened potentials [42–56].

The particular model (in two dimensions) we use here was introduced in Ref. [48] and further studied in Ref. [49]. The model parameters were originally chosen so that a low density triangular crystal (LDT) and a higher density square crystal (S) would have the same energy. The competition between these two structures within the liquid gives rise to anomalous properties, e.g., a line of density maxima. A liquid-liquid critical point is not observed in this 2D system, perhaps because of lack of strong metastability of the liquid below the LDT and S melting lines near the triple point [24]. Given that the model exhibits several anomalies, including two crystals that are less dense than the melt [24], it is perhaps fitting that it also exhibits inverse melting.

This paper is organized as follows. In Section II, we discuss the model and the free energy and computer simulation techniques used in carrying out this work. In Section III, we give our results, including how potential parameters affect the melting line of the S crystal, an estimate of the surface tension between liquid and crystal at

low T coexistence, direct MD simulations showing both metastablity and nucleation of S and the liquid, as well as structural measures that provide evidence against the existence of a hexatic-type phase or quasicrystals near the point of inverse melting. In Section IV we provide a discussion and our conclusions.

4.3 Methods

4.3.1 Model and simulations

The SSSW interaction potential $U(r)$ that we consider in this study is a double-step potential consisting of a square shoulder and a square well as shown in Fig. 4.1. We study the potential in two dimensions, in which it describes disks with a hard-core diameter σ followed by a square shoulder of interaction energy $-\epsilon_1$ for $\sigma < r < b$. The shoulder is followed by a square well of energy $-\epsilon$ for $b < r < c$. As in Ref. [48], we start with potential parameters $\epsilon_1 = \epsilon/2$, $b = \sqrt{2}\sigma$, and $c = \sqrt{3}\sigma$. The three parameters were originally assigned these values in order to bestow two crystals of different density, LDT and S, the same potential energy per particle of -3ϵ, i.e., to create two energetically degenerate phases of well separated densities [49]. The idea behind this is to allow for distinct liquid states, one based on square packing and the other on the more open triangular lattice, in analogy to what is thought to be the case for water.

In Ref [24], we used various Monte Carlo simulation techniques to calculate the phase diagram for the same interaction potential over a wide range of temperature and pressure, as shown in Fig. 4.2(a), for the liquid (L), gas (G) and five crystal phases: the close-packed high-density triangular (HDT) crystal, LDT, S, and two low-T crystals A and Z. Apart from the case of the L-HDT transition at high T, the methods used to calculate phase boundaries required metastability of the phases

concerned, and therefore provided evidence that the transitions are first order.

We also found that the S-L melting line exhibits a maximum temperature, as well as a maximum pressure that implied inverse melting over a very small range in pressure. We did not, however, provide any strong direct evidence that the model exhibits inverse melting. Our goal in the present study is to find potential parameters ϵ_1, b and c that significantly increase the range of pressure over which inverse melting occurs, so that it can be observed more easily.

In this study, our calculations are based on free energy techniques that employ standard Metropolis MC simulations performed at constant number of particles N, P, and T, i.e., in the NPT ensemble [57]. We simulate 1024 particles in a square box with periodic boundary conditions and we change the box size isotropically to maintain its square shape. To observe the liquid freeze after increasing T and the crystal melt upon decreasing T with an independent method, we carry out EDMD simulations [58–61] of up to 65536 particles.

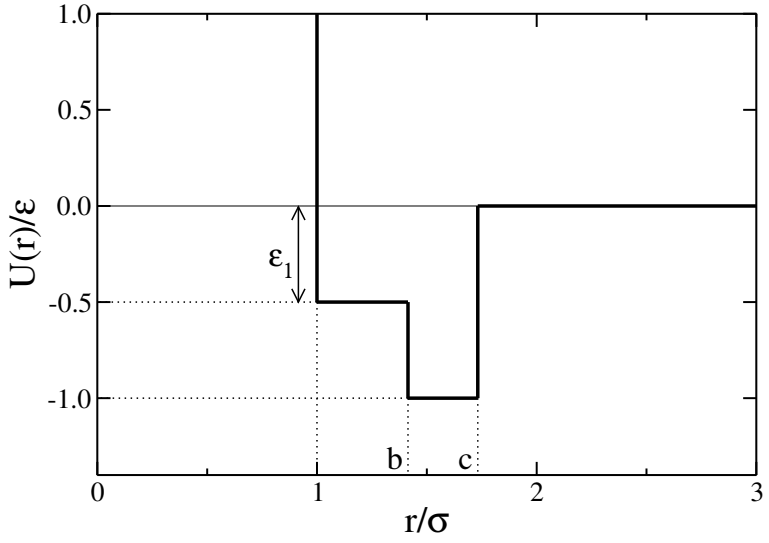

Figure 4.1: Square-shoulder square-well potential with hard-core diameter σ and bond energy ϵ as a function of particle separation r. The original model parameters [48] are soft-core distance $b = \sqrt{2}\sigma$, shoulder depth $\epsilon_1 = \epsilon/2$ and limit of attraction $c = \sqrt{3}\sigma$.

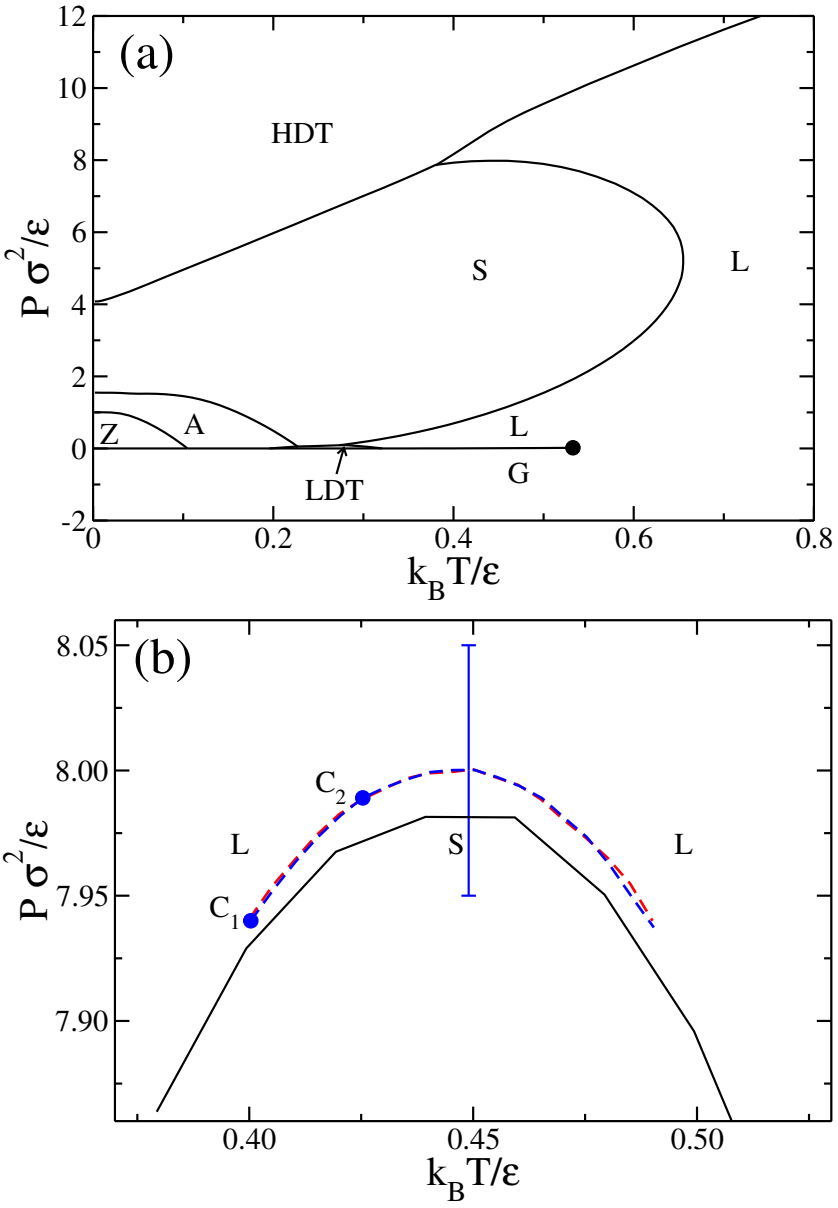

Figure 4.2: Panel (a) shows the phase diagram of the SSSW potential model with potential parameters $\epsilon_1 = \epsilon/2$, $b = \sqrt{2}\sigma$ and $c = \sqrt{3}\sigma$ (adapted from Ref. [24]). Panel (b) is a close-up of the maximum pressure of the L-S line. C_1 is the lower melting point along $P\sigma^2/\epsilon = 7.94$, from which Gibbs-Duhem integration is carried out to determine the coexistence line to the higher melting point at the same pressure (blue dashed curve). The red dashed coexistence curve results from integrating from the higher melting T back to C_1. The error bar indicates shifting of coexistence conditions arising chiefly from uncertainty in μ_{L}. Both C_1 and C_2 are points on the coexistence line from which Hamiltonian Gibbs-Duhem integration is carried out to explore the effect of changing model parameters.

4.3.2 Square crystal-liquid coexistence

Although we calculated the S melting line for the SSSW model with its original parameters in Ref. [24] and found good consistency between traces of the coexistence curve starting at independent initial coexistence points, we wish to recalculate the curve since the inverse melting effect is so small. Our present approach is to calculate the chemical potential for both S ($\mu_{\rm S}$) and L ($\mu_{\rm L}$) as a function of T along $P\sigma^2/\epsilon = 7.94$, a pressure at which $\mu_{\rm L}(T)$ and $\mu_{\rm S}(T)$ should cross twice, since this pressure should be in the middle of the narrow inverse melting pressure range, as shown in Fig. 4.2(b), and there should be two melting temperatures.

For the S crystal, we calculate a reference excess chemical potential to be $\beta\mu_{\rm S}^{\rm ex} = 7.3699 \pm 0.0005$ at $P\sigma^2/\epsilon = 7.94$ and $k_BT/\epsilon = 0.45$ [and where $\beta = (k_BT)^{-1}$], a T which should fall between the two melting temperatures, using the Frenkel-Ladd method [24, 62]. This method requires simulations at constant N and ρ, which we find to be $\rho\,\sigma^2 = 0.907$ at this state point, with an uncertainty of ± 0.002. The ideal gas contribution to the chemical potential is $\beta\mu_{\rm id} = \ln \Lambda^2\rho$, where Λ is the de Broglie wavelength.

For the liquid, we determine $\mu_{\rm L}$ at $P\sigma^2/\epsilon = 7.94$ and $k_BT/\epsilon = 0.7$ using two thermodynamic paths. First, as in Ref. [24], we integrate the equation of state along the $k_BT/\epsilon = 0.7$ supercritical isotherm after fitting it to a phenomenological fitting model [63, 64]. Second, as a check and to have a more independent estimate of the uncertainty, we determine the enthalpy difference between our system and the hard disk system as modeled by the equation of state [65, 66],

$$\frac{P}{\rho kT} = \frac{1 + \eta^2/8}{(1-\eta)^2}, \tag{4.1}$$

where $\eta = \rho\pi\sigma^2/4$ is the area packing fraction. It is somewhat straightforward to

obtain at arbitrary state points both the hard-disk enthalpy $H_{\rm HD} = NP/\rho + Nk_BT$ and chemical potential,

$$\mu_{\rm HD}(\rho) = f_{\rm id} + P/\rho + k_BT \int_0^\rho \left(\frac{P}{\rho k_BT} - 1 \right) \frac{d\rho}{\rho}, \tag{4.2}$$

where $f_{\rm id} = k_BT(\ln \Lambda^2\rho - 1)$ is the ideal gas Helmholtz free energy per particle.

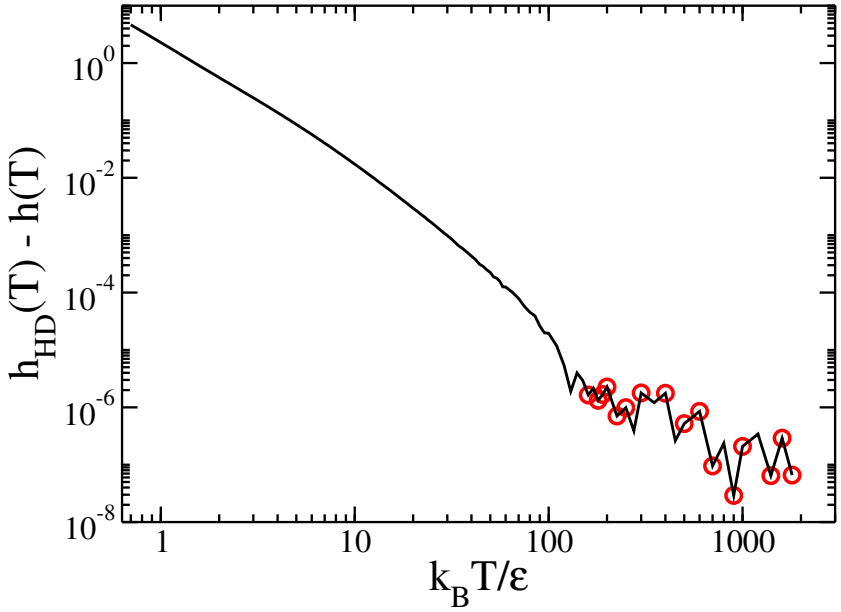

Figure 4.3: The absolute value of the integrand of Eq. 4.3, where the quantity $h(T) = H(T)/(Nk_BT^2) \times \epsilon/k_B$ at $P\sigma^2/\epsilon = 7.94$, and $h_{\rm HD}(T)$ is the analogous quantity for the hard disk model. Circles indicate points for which the calculated enthalpy difference is negative, and indicate the T at which the integrand is essentially noise.

The chemical potential for our system can then be written as,

$$\frac{\mu_{\rm L}(T_0)}{k_BT_0} = \frac{\mu_{\rm HD}(T_0)}{k_BT_0} + \int_{T_0}^{T_\infty} \frac{(H_{\rm HD}(T) - H(T))}{Nk_BT^2} dT, \tag{4.3}$$

where we have assumed that $H_{\rm HD}(T_\infty) = H(T_\infty)$ and used the relation,

$$\frac{\mu(T_2, P)}{k_BT_2} = \frac{\mu(T_1, P)}{k_BT_1} - \int_{T_1}^{T_2} \frac{H(P,T)}{Nk_BT^2} dT. \tag{4.4}$$

The integrand in Eq. 4.3 is plotted in Fig. 4.3 and we see that beyond $k_BT/\epsilon \approx 200$, the integrand is essentially noise. We evaluate the integral both directly and with a change in variable of $\tau = \ln T$ using different interpolation orders to values of k_BT_∞/ϵ ranging from 200 to 2000. For the hard disks at $k_BT_0/\epsilon = 0.7$ and $P_0\sigma^2/\epsilon = 7.94$, $\beta\mu_{\rm HD}^{\rm ex} = 12.855287$ (excess chemical potential).

Combining results from the two different thermodynamic routes, we obtain the excess chemical potential for our liquid at T_0 and P_0, where the liquid density is $\rho\sigma^2 = 0.893 \pm 0.003$, to be $\beta\mu_{\rm L}^{\rm ex} = 13.323 \pm 0.006$. The uncertainty arises chiefly from integrations such as the one in Eq. 4.3.

Having obtained a value of the chemical potential at reference temperatures at $P\sigma^2/\epsilon = 7.94$ for both L and S, we use Eq. 4.4 to determine the difference in chemical potential, $\beta\Delta\mu \equiv \beta\mu_{\rm L}(T) - \beta\mu_{\rm S}(T)$ as a function of T, which we plot in Fig. 4.4(a). The figure shows two T at which crossing of zero occurs, which is required for inverse melting to occur. However, given the uncertainties in calculating the chemical potential and the small value of $\beta\Delta\mu$, it is entirely possible that the liquid does not crystallize along this pressure at all. Therefore, when we amplify the inverse melting effect below, it is necessary to check the effect by complementary methods.

Fig. 4.4(b) shows the entropy of the crystal becoming increasingly larger than that of the liquid for T decreasing below $k_BT/\epsilon \approx 0.45$, which is required for crystallization upon heating past the lower of the two coexistence T. Fig. 4.4(c) shows that the volume contribution to the enthalpy of the crystal in this range also becomes increasingly larger than the liquid's as T decreases, which tends to destabilize the crystal with respect to the liquid. Fig. 4.4(d) shows that the energetic driving force for phase transformation does not change with T.

Having obtained at P_0 two coexistence temperatures $T_{m1} = 0.400345\epsilon/k_B$ and $T_{mHigh} = 0.490054\epsilon/k_B$, we carry out a Gibbs-Duhem integration [67, 68], as in

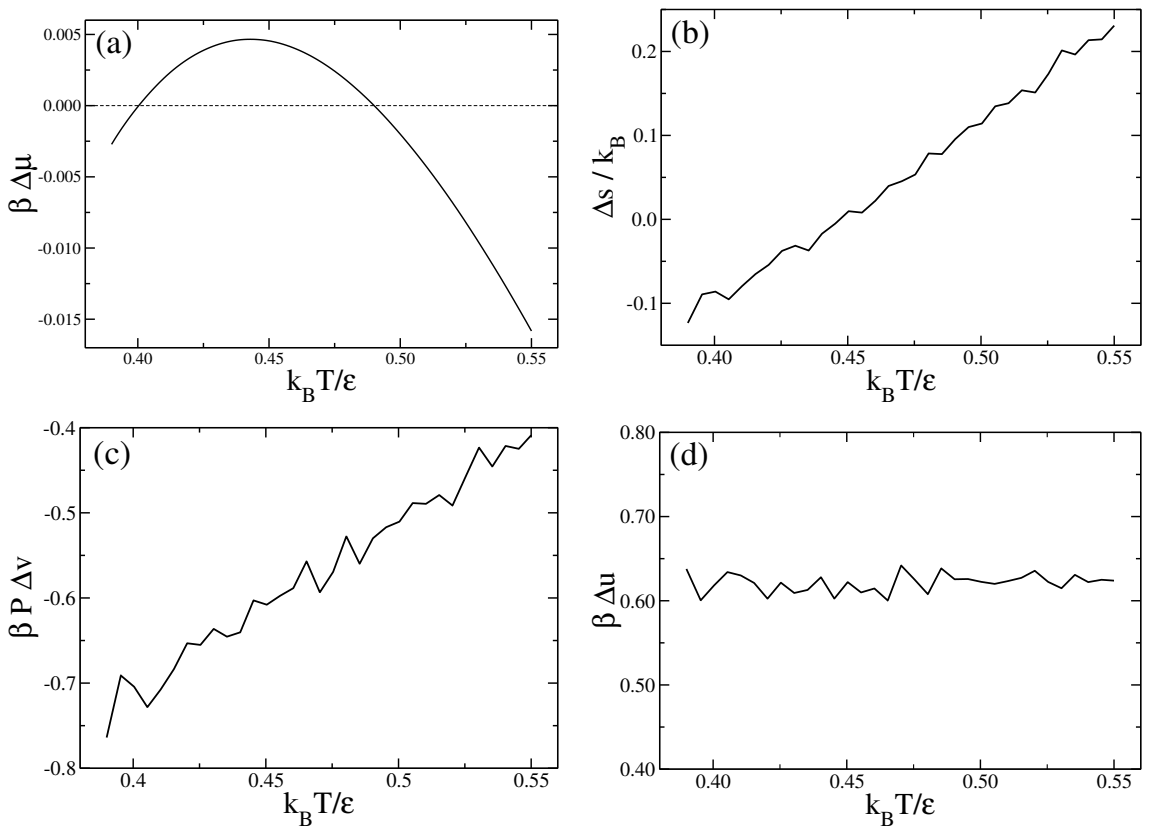

Figure 4.4: Differences in thermodynamic quantities between the L and S phases as a function of T at $P\sigma^2/\epsilon = 7.94$, where $\Delta q \equiv q_L - q_S$ for a per particle quantity q. Quantities considered are (a) chemical potential $\Delta\mu$, where a negative value indicates that the liquid is the stable phase, (b) entropy Δs, (c) the mechanical contribution to the enthalpy $P\,\Delta v$ and (d) potential energy Δu. Below $T \approx 0.39$, the S phase no longer shows appreciable metastability.

Ref. [24], of the Clausius-Clapeyron equation that describes the slope in the P-T plane of the coexistence line,

$$\frac{dP}{dT} = \frac{\Delta s}{\Delta v} = \frac{\Delta h}{T\Delta v}, \tag{4.5}$$

where Δs is the molar entropy difference, Δh is the molar enthalpy difference, and Δv is the molar volume (area in 2D) difference between the two coexisting phases. To test the accuracy of the integration, we carry it out twice, starting from the state point (P_0, T_{m1}), labelled C_1 in Fig. 4.2(b), and increasing T until T_{mHigh}, and again from

(P_0, T_{mHigh}) down in temperature. The overlapping results for the coexistence line are shown in Fig. 4.2(b). The uncertainty in the position of the line is predominantly due to the uncertainty in calculating the reference entropy of the liquid. An upward shift of 0.006 (the uncertainty in $\beta\mu_{\rm L}$) in the $\beta\Delta\mu$ curve shown in Fig. 4.4(a) results in a certain shift in the melting temperatures along P_0. This in turn produces a shift in the coexistence curve, the extent of which is indicated by the error bar in Fig. 4.2(b). It is not surprising that there is a small discrepancy between the present results and those of Ref. [24], given that different thermodynamic paths are used to calculate initial coexistence conditions and that small values of $\beta\Delta\mu$ make the calculations quite sensitive.

4.3.3 Hamiltonian Gibbs-Duhem integration

After determining the coexistence curve that exhibits inverse melting, we use Hamiltonian Gibbs-Duhem integration to find the potential parameters (ϵ_1, b, c) that increase the range of inverse melting. This technique allows one to find a coexistence point for a system governed by a potential energy U_B starting from a known coexistence point for the system defined by potential energy U_A. The starting point is to introduce a potential that depends on a coupling parameter λ, which we choose to be [69, 70],

$$U(\lambda) = \lambda U_B + (1 - \lambda)U_A. \tag{4.6}$$

As λ changes from zero to one, the potential continuously transforms from U_A to U_B. In our case, U_A is determined by the SSSW pair potential using the original parameters, while U_B is given by the SSSW potential with a different set of parameters.

Ref [71] has shown that the generalized Clapeyron equations for two coexisting phases I and II at constant pressure and temperature can be written as, respectively,

$$\left.\frac{dT}{d\lambda}\right|_P = T\frac{\langle \partial u_{II}/\partial\lambda\rangle_{NPT\lambda} - \langle \partial u_I/\partial\lambda\rangle_{NPT\lambda}}{h_{II} - h_I} \tag{4.7}$$

$$\left.\frac{dP}{d\lambda}\right|_T = -\frac{\langle \partial u_{II}/\partial\lambda\rangle_{NPT\lambda} - \langle \partial u_I/\partial\lambda\rangle_{NPT\lambda}}{v_{II} - v_I} \tag{4.8}$$

where $\partial u_I/\partial\lambda$, given Eq. 4.6, is the quantity $U_B - U_A$ per particle for phase I, h_I is its per particle enthalpy and v_I its per particle volume. Similarly for phase II. $\langle . \rangle_{NPT\lambda}$ indicates an average in the NPT ensemble when the system is governed by $U(\lambda)$. In principle, by applying this technique to many coexistence points, one can obtain the phase diagram of a new model potential starting from a known phase diagram of another model.

To simplify finding the optimized parameters that can increase the inverse melting, we implement the Hamiltonian Gibbs-Duhem integration at constant temperature, given in Eq. 4.8, first for only two coexistence points on the inverse melting curve, labelled C_1 and C_2 in Fig. 4.2(b). As a convenient measure of the effectiveness with which a change in the pair potential increases the region in the P-T plane over which inverse melting occurs, we use the slope $M = (P_{C_2} - P_{C_1})/(T_{C_2} - T_{C_1})$. For example, if changing the potential causes M to increase, then the pressure range of inverse melting increases. We vary ϵ_1, b and c independently to determine which parameter most effectively increases M. The two original coexistence points that we use to study M as a function of potential parameters are $C_1 = \{k_B T_{m1}/\epsilon = 0.400345, P_0\,\sigma^2/\epsilon = 7.94\}$ and $C_2 = \{k_B T_{m2}/\epsilon = 0.425345, P_{m2}\,\sigma^2/\epsilon = 7.98906\}$. As a potential parameter is varied, the coexistence P will change, causing M to increase or decrease.

4.3.4 Biased Monte Carlo simulations

Once the coexistence line has been recalculated for a new set of model parameters, we choose a P-T state point on the coexistence line to evaluate the distribution of density fluctuations. This calculation is necessary to compute the free energy barrier between L and S, and to verify a coexistence point by a different method. The probability distribution function for the density, determined at conditions of constant T and P, defines the conditional (or Landau) Gibbs free energy,

$$\Delta G(T, P; \rho) = G(T, P; \rho) - G_0 = -k_B T \ln[P_r(\rho)], \tag{4.9}$$

where $P_r(\rho)\, d\rho$ is the probability of finding the system with density between ρ and $\rho + d\rho$ and G_0 is a constant that ensures that the average of $G(T, P; \rho)$ gives the equilibrium Gibbs free energy $G(T, P)$. For a finite system at a first order coexistence point, there should be two peaks of equal areas in $P_r(\rho)$. If the shapes of the peaks are similar, the two resulting minima in $\Delta G(T, P; \rho)$ will have the same value. The barrier between these minima arises from the work required to form the transition state, which for a large enough periodic system amounts to creating two interfaces that span the width of the simulation box.

To ensure good sampling of ρ, we use the umbrella sampling MC simulation [57] carried out by NPT simulations to calculate $G(T, P; \rho)$. To implement umbrella sampling, we add the following constraint potential U_c,

$$U_c(\rho) = \frac{k}{2}(\rho - \rho_0)^2, \tag{4.10}$$

to the system potential energy. The biasing potential will force a given simulation to sample densities in the vicinity of ρ_0. k is a constant that controls the range

of sampled densities. We use simulation windows with equally spaced values of ρ_0, and perform two sets of simulations with $N = 2082$ in a rectangular (two squares) simulation box (using isotropic scaling to maintain P), one with $k = 640000\epsilon/\sigma^4$ and again with $k = 1280000\epsilon/\sigma^4$. We convert the probability distribution from the constrained ensemble $P_{rc}(\rho)$ to the NPT ensemble via $P_r(\rho) \propto \exp[\beta U_c(\rho)]P_{rc}(\rho)$. The pieces of $\Delta G(T, P; \rho)$ determined near each ρ_0 can be combined by essentially shifting each to produce a smooth $\Delta G(T, P; \rho)$ for the entire density range. We use MBAR [72] to accomplish this.

There will necessarily be some error in calculating coexistence conditions at which we perform umbrella sampling. To more precisely locate the coexistence pressure, we reweight the $\Delta G(T, P; \rho)$ curve by applying a pressure shift,

$$\beta G(T, P'; \rho) = \beta G(T, P_0; \rho) + \frac{N\beta\Delta P}{\rho} + c, \tag{4.11}$$

where c is a constant related to normalization. The corrected coexistence pressure is then $P' = P_0 + \Delta P$, where P_0 is the original coexistence pressure at which the constrained simulations are performed and ΔP is the pressure shift that brings the two minima in $\Delta G(T, P_0; \rho)$ to the same level.

To distinguish the S and L phases in a visualization of the configurations produced, we make used of the Steinhardt bond order parameters based on spherical harmonics [73] as was done in Ref. [24].

4.3.5 Analysis of long range correlations

In order to distinguish the liquid, crystal and hexatic phases in two dimensions, one typically measures or calculates translational and orientational correlation functions [74]. For translations, in addition to the radial distribution function $g(r)$, we

calculate,

$$G_{\vec{g}}(r) = \langle \exp\left(i\vec{g}\cdot\vec{r}_j\right)\rangle\,, \tag{4.12}$$

where we average the result over reciprocal lattice vectors $\vec{g} = \hat{x}\,2\pi/a$ and $\vec{g} = \hat{y}\,2\pi/a$, a is the expected lattice spacing in the S phase for the density studied, $\vec{r}_j$ with magnitude r is the position of particle j relative to an origin taken to be one of the particle positions, and $\langle . \rangle$ indicates an ensemble average over configurations, origins and particles j. For orientational order, we use,

$$G_4(r) = \left\langle q_4(\vec{r})\, q_4^*(\vec{0})\right\rangle, \tag{4.13}$$

$$q_4(\vec{r}_j) = \frac{1}{N_j}\sum_{k=1}^{N_j} \exp\left(4i\theta_{jk}\right), \tag{4.14}$$

where q_4^* is the complex conjugate of q_4, θ_{jk} is the angle made by the bond with respect to an arbitrary but fixed axis between particle j and neighbor k, neighbors being those particles that are closer together than a distance of 1.24σ, and the sum is over the N_j neighbors of particle j.

The expectation based on the KTHNY theory of melting [50, 74, 75] in two dimensions for these functions is that both $G_4(r)$ and $G_{\vec{g}}(r)$ decay exponentially in the liquid phase, that $G_4(r)$ decays as a power law with a small exponent ($\leq 1/4$) and $G_{\vec{g}}(r)$ decays exponentially in the hexatic phase, and that $G_4(r)$ tends to a constant and $G_{\vec{g}}(r)$ decays slowly as a power law with a small exponent ($\leq 1/3$) in the crystal.

To detect the presence of a quasicrystal phase, we calculate the structure factor,

$$S(\vec{q}) = \frac{1}{N}\left\langle \rho_{\vec{q}}\, \rho_{\vec{q}}^*\right\rangle, \tag{4.15}$$

where,

$$\rho_{\vec{q}} = \sum_{i=1}^{N} \exp\left(-i\,\vec{q}\cdot\vec{r}_i\right), \tag{4.16}$$

and $\langle . \rangle$ indicates an ensemble average and ρ^* is the complex conjugate of ρ. In our periodic system, the allowed reciprocal vectors are $\vec{q} = 2\pi(n_x, n_y)/L$, where L is the length of the simulation box and $n_{x,y}$ are integers.

4.4 Results

4.4.1 Expanding the range in inverse melting

Each panel in Fig. 4.5 shows how the slope M between two selected points on the original S-L coexistence curve, C_1 and C_2 [Fig. 4.2(b)] changes when each of ϵ_1, b and c is varied with the other two parameters held fixed. A larger value of M compared with the original parameters indicates an expanded range of pressures over which inverse melting should be observed. The filled red circle in each panel represents the value of M when using the original potential parameters: $\epsilon_1 = \epsilon/2$, $b = \sqrt{2}\sigma$ and $c = \sqrt{3}\sigma$. From Fig. 4.5(a), we conclude that M is already near the maximum for the original value of ϵ_1, and therefore changing this parameter will not help increase the range of inverse melting. On the other hand, Fig. 4.5(b) shows that M increases by a factor of three when b is increased, greatly expanding the range of inverse melting. Increasing the parameter c beyond the values shown in Fig. 4.5(c) results in losing the L phase in favor of HDT. Thus it appears that in this case, L-S inverse melting becomes metastable with respect to HDT.

Given that b alone is the important parameter in increasing the range of inverse melting, we proceed with a more detailed look at how the S-L coexistence curve changes with b. To begin, we perform a Gibbs-Duhem integration for the origi-

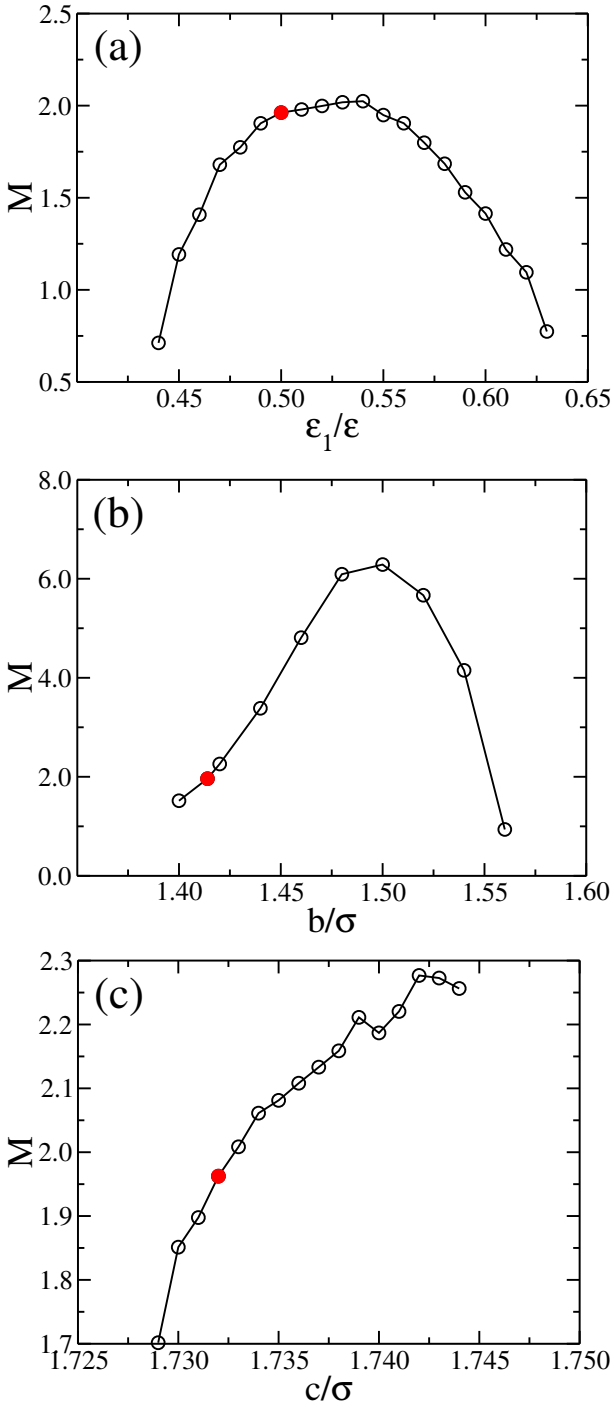

Figure 4.5: The slope M between two S-L coexistence points, labelled C_1 and C_2 for the original parameters in Fig. 4.2(b), changes as a function of (a) ϵ_1, (b) b and (c) c. A larger value of M implies inverse melting occurring over a larger range of P. Filled (red) circles indicate M for the original parameter values.

nal interaction parameters starting from the coexistence point ($k_BT/\epsilon = 0.490345$, $P\sigma^2/\epsilon = 7.94$) to obtain the full curve. For roughly 20 points on this curve, we carry out Hamiltonian Gibbs-Duhem integration for $b/\sigma = 1.40, 1.42, 1.44, 1.46, 1.48$ and 1.50. The results are represented by open symbols in Fig. 4.6(a). To check the accuracy of determining these points, we perform Gibbs-Duhem integration for each value of b, starting from T_{mHigh}, as represented by the solid lines in Fig. 4.6(a). The results obtained by the two integration methods shows a high degree of agreement. From Fig. 4.6(a), it becomes obvious that as the potential parameter b increases, the range of pressure of the inverse melting increases. Concurrent with this change is the reduction of the S stability field.

Fig. 4.6(b) shows the S-L melting line projected on to the ρ-T plane for a selection of b values. The curves demarcate boundaries between regions of single phase stability and of phase coexistence. These regions are labelled for $b/\sigma = 1.50$. For $b/\sigma = 1.42$, inverse melting is observed weakly in the P-T plane but not at all in the ρ-T plane. For larger b, only partial melting on isochoric cooling is indicated in the phase diagram. Even for $b/\sigma = 1.50$, at least for the T studied, there is no density at which cooling a completely crystalline system results in a system that is completely liquid. Thus, although inverse melting is present in the ρ-T plane, it is a weaker effect.

For the analysis that follows, we focus on the SSSW potential for which $b/\sigma = 1.46$ while ϵ_1 and c are kept at their original values. Already at this value of b, the range in P over which the coexistence line exhibits inverse melting is considerable. This allows more direct methods to confirm the phenomenon.

4.4.2 Interfacial tension between S and L

To confirm inverse melting, we report the $G(T, P; \rho)$ from a histogram of the densities sampled by a series of biased NPT simulations with 2082 particles at the coexistence

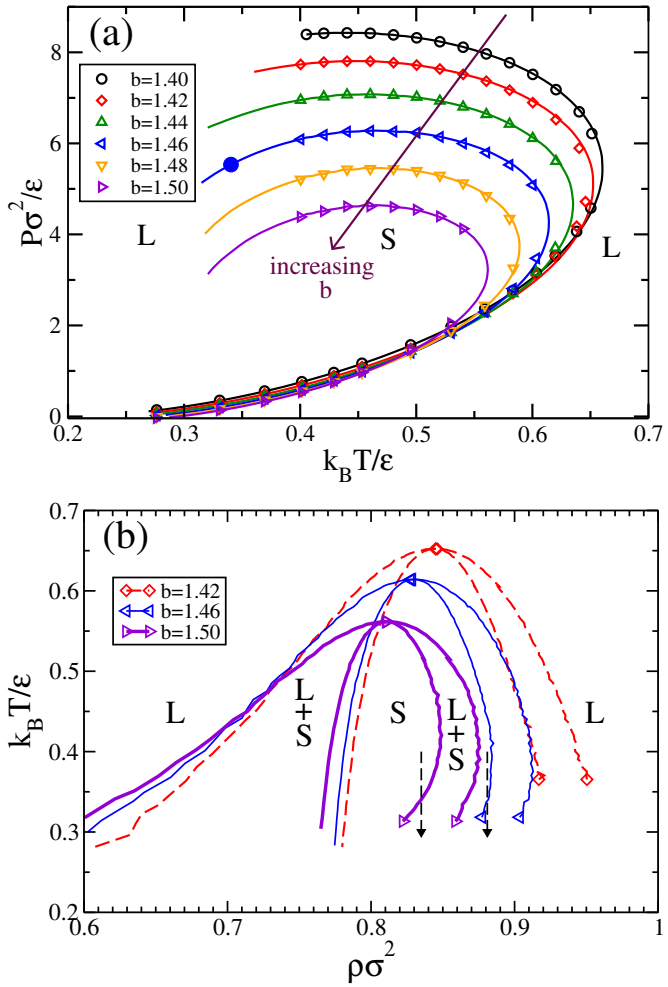

Figure 4.6: Panel (a) shows the S-L coexistence curve in the P-T plane for b/σ ranging from 1.40 to 1.50, calculated by Gibbs-Duhem (curves) and Hamiltonian Gibbs-Duhem (symbols) integration. The large filled circle indicates the coexistence point at which biased Monte Carlo simulations explicitly show a free energy barrier between the S and L phases. Panel (b) shows Gibbs-Duhem results in the ρ-T plane. The curves reach their maximum at the point when the phase boundary in the P-T plane has a vertical slope. To the left of the maximum the liquid is less dense than the solid, corresponding to a positive slope of the melting line at lower P in the P-T plane. To the right of the maximum, the solid is less dense than the liquid; in the P-T plane this corresponds to the portion of the melting line with negative slope and the high-P-low-T inverse melting portion. Partial inverse melting at constant volume corresponds to decreasing T from within the region of S phase stability along a vertical line into the L+S region, for which liquid and solid coexist. Such paths are possible for $b = 1.46\sigma$ and $b = 1.50\sigma$ and are indicated by dashed arrows; for $b = 1.42\sigma$, such a path is not possible. Complete inverse melting at constant volume, corresponding to a vertical line descending from region S to region L (stable liquid), is not possible for our range of data even for $b = 1.50\sigma$.

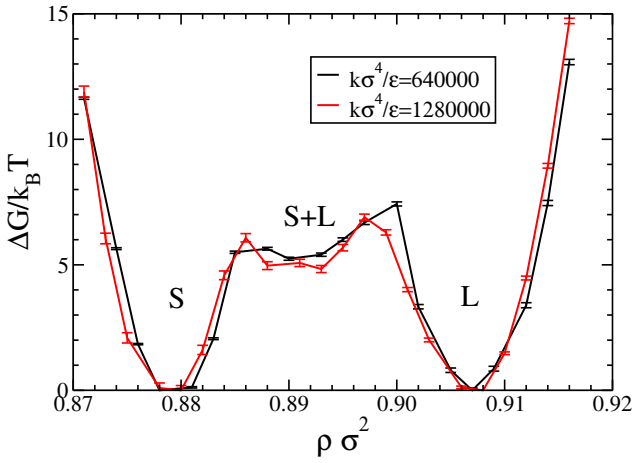

Figure 4.7: Conditional Gibbs free energy as a function of ρ calculated at temperature $k_BT/\epsilon = 0.340345$ and reweighted by Eq. 4.11. The black curve is calculated for $k\sigma^4/\epsilon = 640000$ and red for 1280000.

point ($k_BT/\epsilon = 0.340345$, $P\sigma^2/\epsilon = 5.5331$) for the SSSW model for which $b/\sigma = 1.46$. This coexistence point is indicated by the large filled circle in Fig. 4.6(a).

The results are shown in Fig. 4.7, where we use Eq. 4.11 to bring the free energy minima to the same level. The pressure shifts required in this reweighting are small, $\Delta P\sigma^2/\epsilon = -0.0261$ for the simulations with $k\sigma^4/\epsilon = 6.4\times10^5$ and $\Delta P\sigma^2/\epsilon = -0.0295$ for the simulations with $k\sigma^4/\epsilon = 12.8\times10^5$, indicating that the errors built up during the several steps in determining the coexistence line is indeed small. The curves show a barrier of approximately 5 k_BT separating the lower density S phase from the higher density liquid.

The shape of the barrier, generally flat with overshoots at either end, is consistent with the morphology of the separated phases. Despite the rather diffuse interface between S and L, as noted in Ref. [24], the system is large enough to accommodate an isolated liquid droplet within the S phase. This we show in Fig. 4.8(a), which shows a snapshot from the biased NPT simulation with $\rho_0\sigma^2 = 0.8862$, i.e., near the overshoot occurring as the density of the system is constrained to the high density side of the S basin in $G(T, P; \rho)$. At higher density, Fig. 4.8(b), the L phase spans the

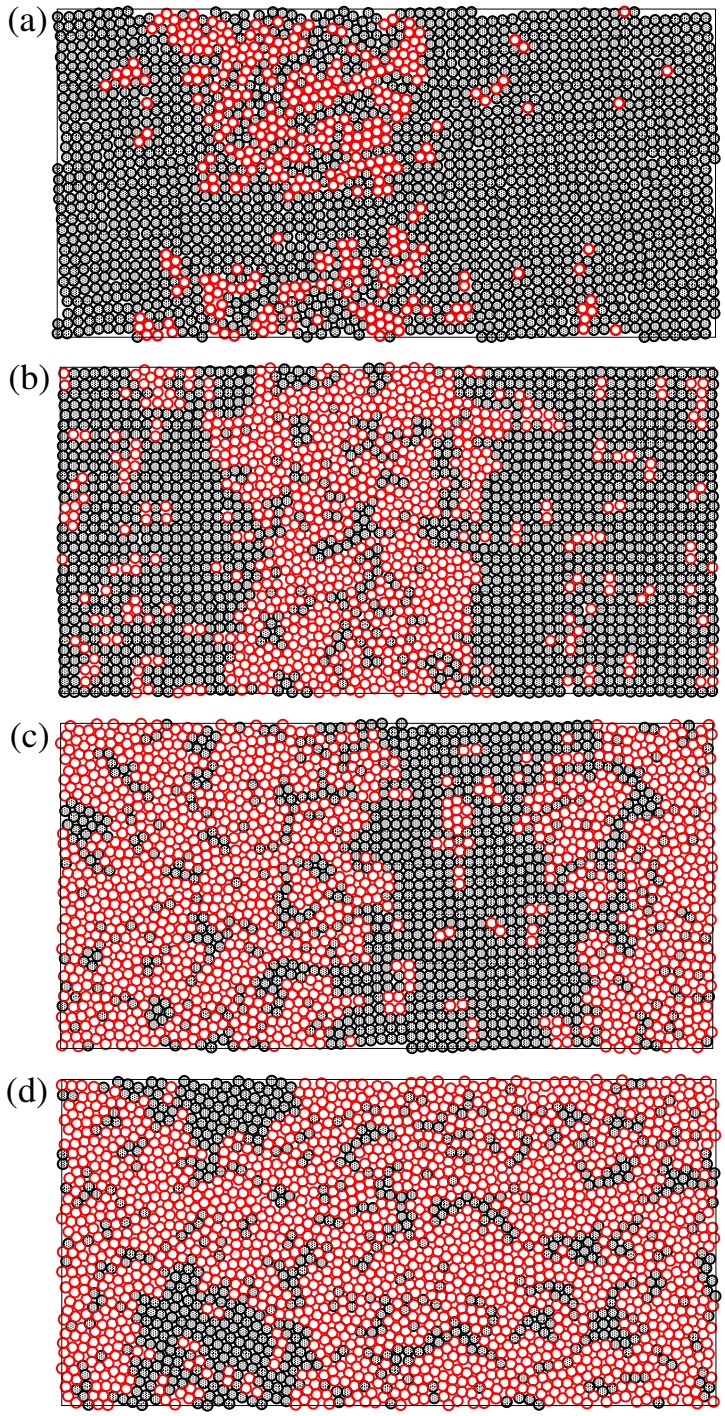

Figure 4.8: Snapshot of configurations taken from different windows of umbrella sampling for $N = 2082$ particles. Fig. 4.8(a) shows a liquid bubble at $\rho_0\sigma^2 = 0.8862$, Fig. 4.8(b) shows a liquid strip at $\rho_0\sigma^2 = 0.8887$, Fig. 4.8(c) shows a square-crystal strip at $\rho_0\sigma^2 = 0.8975$ and Fig. 4.8(d) shows a square-crystal bubble at $\rho_0\sigma^2 = 0.9000$.

width of the periodic simulation cell. If the width of the strip is sufficiently wide to accommodate two well formed S-L interfaces, then increasing the density further will not change the free energy, as both phases are at the same chemical potential. In our case, the system may not be large enough to accomplish this, as we can only claim a broad minimum near $\rho\sigma^2 = 0.89$ and not a truly flat region in the barrier, and so we can only estimate an upper bound on the interfacial tension. Taking the minimum of the barrier to be $\beta\Delta G(T, P; \rho^*) = 5.1 \pm 0.2$, we determine the interfacial tension to be $\gamma\sigma/\epsilon = \Delta G(T, P; \rho^*)/(2w) = 0.025 \pm 0.001$, where $w/\sigma = 34.160$ is the box width and $\beta\epsilon = 0.340345^{-1}$, or $\beta\gamma\sigma = 0.075 \pm 0.003$. Increasing the density further results first in a strip of the S phase within the liquid [Fig. 4.8(c)] and then a bubble of S [Fig. 4.8(d)] before reaching the homogeneous liquid.

4.4.3 Direct simulation of freezing and melting

As a rough check on the portion of the S-L coexistence curve that exhibits inverse melting and to determine the extent of metastability, we perform a set of NPT simulations for the potential parameters $\epsilon_1 = 0.5$, $b = 1.46\sigma$ and $c = \sqrt{3}\sigma$ to map out the range of metastability of L and S. For both phases, we use 1024 particles in a square box, scaling the box size isotropically to maintain P. We initialize the L simulations with a liquid configuration and the S simulations with a square crystal, and we run each state point for 4×10^8 MC steps per particle. We indicate with a blue x sign in Fig. 4.9 the state points for which simulations either retain the L phase or melt to the L phase, and with a red open square symbol the state points for which simulations either retain the S phase or crystallize to S.

From Fig. 4.9, we see that the L phase is obtained well above the coexistence curve and the S crystal is obtained for state points well within its predicted stability field. At and near the coexistence curve, we see both phases at every state point, indicating

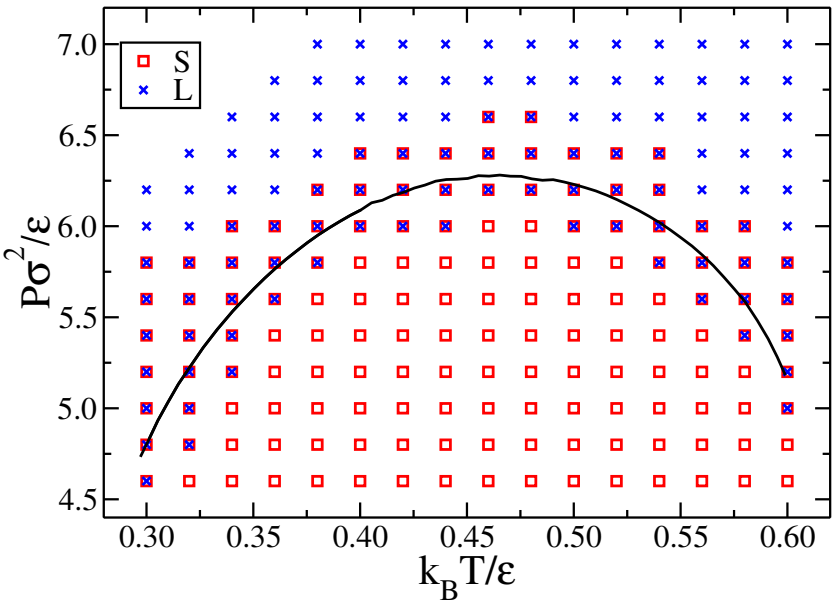

Figure 4.9: The solid line is the S-L coexistence curve for the potential parameters $\epsilon_1 = 0.5$, $b = 1.46\sigma$ and $c = \sqrt{3}\sigma$ and the grid of points is obtained from two sets of NPT MC simulations, one beginning from a perfect S configuration and the other from a liquid. A blue x symbol represents a simulation that ended in the L phase, while a red open square represents a simulation that ended in the S phase. A state point with both symbols indicates that each simulation retained its starting phase.

the stability or metastability of the two phases. We also see the tendency for points exhibiting either liquid or S metastability to track the curvature of the S-L melting line. For this system size, inverse melting is directly confirmed at $P\sigma^2/\epsilon = 6.0$: at low T, only the liquid survives; at $k_BT/\epsilon \approx 0.46$ only S survives; and by $k_BT/\epsilon \approx 0.60$, only the liquid is stable.

To independently confirm these findings, we carry out EDMD simulations of 1024 and 65536 particles along the $P\sigma^2/\epsilon = 5.6$ isobar. In Fig. 4.10 we plot the density as a function of time for a few T, chosen to illustrate the behavior of both phases when they are stable, metastable and undergoing a phase transformation. The most dramatic and direct illustration of melting of S at low T is for the $N = 1024$ simulation at $k_BT/\epsilon = 0.30$, which started from a perfect S crystal, where the density exhibits a sudden increase as the system transforms from S to L. Such a jump is typical of first

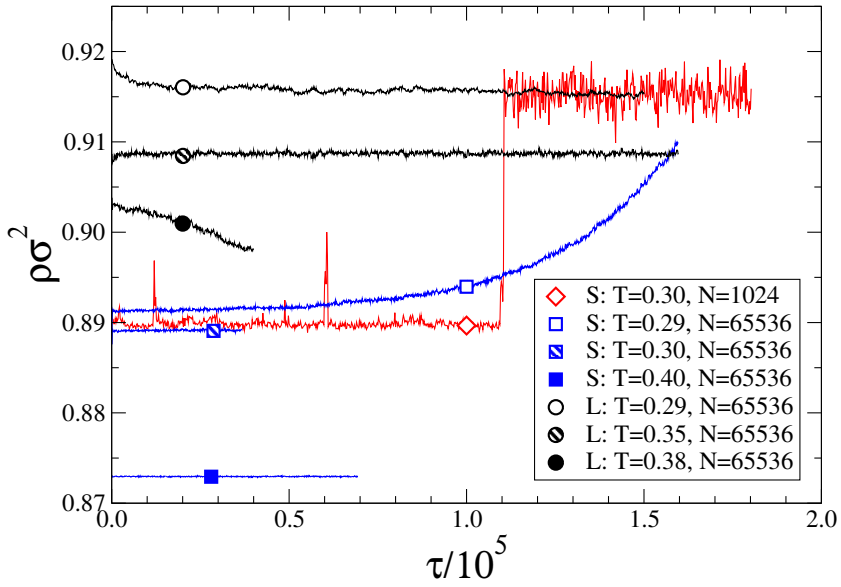

Figure 4.10: Density as a function of time from EDMD simulations at $P\sigma^2/\epsilon = 5.6$. Here reduced time $\tau = t\sqrt{\epsilon/(\sigma^2 m)}$. Legend gives initial phase, T and system size. For the $N = 1024$ simulation, time is reduced by a factor of 50 for ease of comparison (i.e., its simulation time is roughly 50 times longer than the longest simulation for $N = 65536$).

order transitions when the crystallization of the system is dominated by nucleation. Note that time for this smaller system is reduced by a factor of 50 for plotting purposes in order to compare with the time scales of the $N = 65536$ simulations.

To observe melting of S for the larger system on a reasonable time scale, we reduce the temperature to $k_BT/\epsilon = 0.29$. Here, the slow, rather continuous increase in ρ arises from crystallization being dominated by growth. In Fig. 4.11(a) we plot dots representing the rather uniformly distributed locations of L-like particles within the metastable S phase for a snapshot configuration at $k_BT/\epsilon = 0.30$ and reduced time $\tau = t\sqrt{\epsilon/(\sigma^2 m)} = 36741$. Fig. 4.11(b) shows distinct domains of the L phase appearing as S melts at $k_BT/\epsilon = 0.29$ (snapshot taken at $\tau = 74732$), which is consistent with the first order nature of the transition. The time series for S at $k_BT/\epsilon = 0.40$ is representative of the stable S phase.

Addressing the liquid, we show in Fig. 4.10 density time series for three state points: $k_BT/\epsilon = 0.29$, where L is thermodynamically stable; $k_BT/\epsilon = 0.38$, where L is unstable and the time series decays to lower ρ as the S phase forms; and $k_BT/\epsilon = 0.35$, where the time series is stable and, according to our calculated phase boundaries, L is metastable. Snapshots from the $k_BT/\epsilon = 0.35$ ($\tau = 46459$) and $k_BT/\epsilon = 0.38$ ($\tau = 40000$) simulations showing only S-like particles are plotted in Figs. 4.11(c) and 4.11(d), respectively. Similarly to the case of crystal melting, we see distinct domains of the stable phase surrounded by the metastable phase in Fig. 4.11(d).

Encouraged by these EDMD results, we perform additional EDMD simulations of $N = 65536$ particles for the model with $b = 1.46\sigma$ (which exhibits strong inverse melting) and the original model with $b = \sqrt{2}\sigma$ (where inverse melting is at best very weak), and report the following. For $b = 1.46\sigma$, and $P\sigma^2/\epsilon = 5.6$ starting from the L phase, simulations for $k_BT/\epsilon \geq 0.56$ remain as L, for $0.40 \leq k_BT/\epsilon \leq 0.55$ transform to S, and for $k_BT/\epsilon \leq 0.38$ remain as L. Again for $b = 1.46\sigma$, and $P\sigma^2/\epsilon = 5.6$ but starting from the S phase, simulations for $k_BT/\epsilon \geq 0.58$ transform to L, for $0.36 \leq k_BT/\epsilon \leq 0.56$ remain as S, and for $k_BT/\epsilon \leq 0.34$ transform to L. We also note that for $k_BT/\epsilon \leq 0.31$ the energy of the liquid is lower than that of S. These results are consistent with the phase diagram calculations and also point to the role of a lower potential energy of L with respect to S as a contributing factor in enhancing inverse melting in the $b = 1.46\sigma$ model.

For the original $b = \sqrt{2}\sigma$ model (again with $N = 65536$), it is more difficult for direct EDMD simulations to confirm inverse melting and we thus start simulations with a system that is half S and half L to make confirmation possible. At $P\sigma^2/\epsilon = 7.7$, the system transforms to HDT for $k_BT/\epsilon \leq 0.37$, appears to contain S, HDT and L at $k_BT/\epsilon = 0.38$ (which is close to the triple point), converts to S for $0.39 \leq k_BT/\epsilon \leq 0.51$ and converts to L for $k_BT/\epsilon \geq 0.52$. At $P\sigma^2/\epsilon = 7.8$ inverse melting is also confirmed.

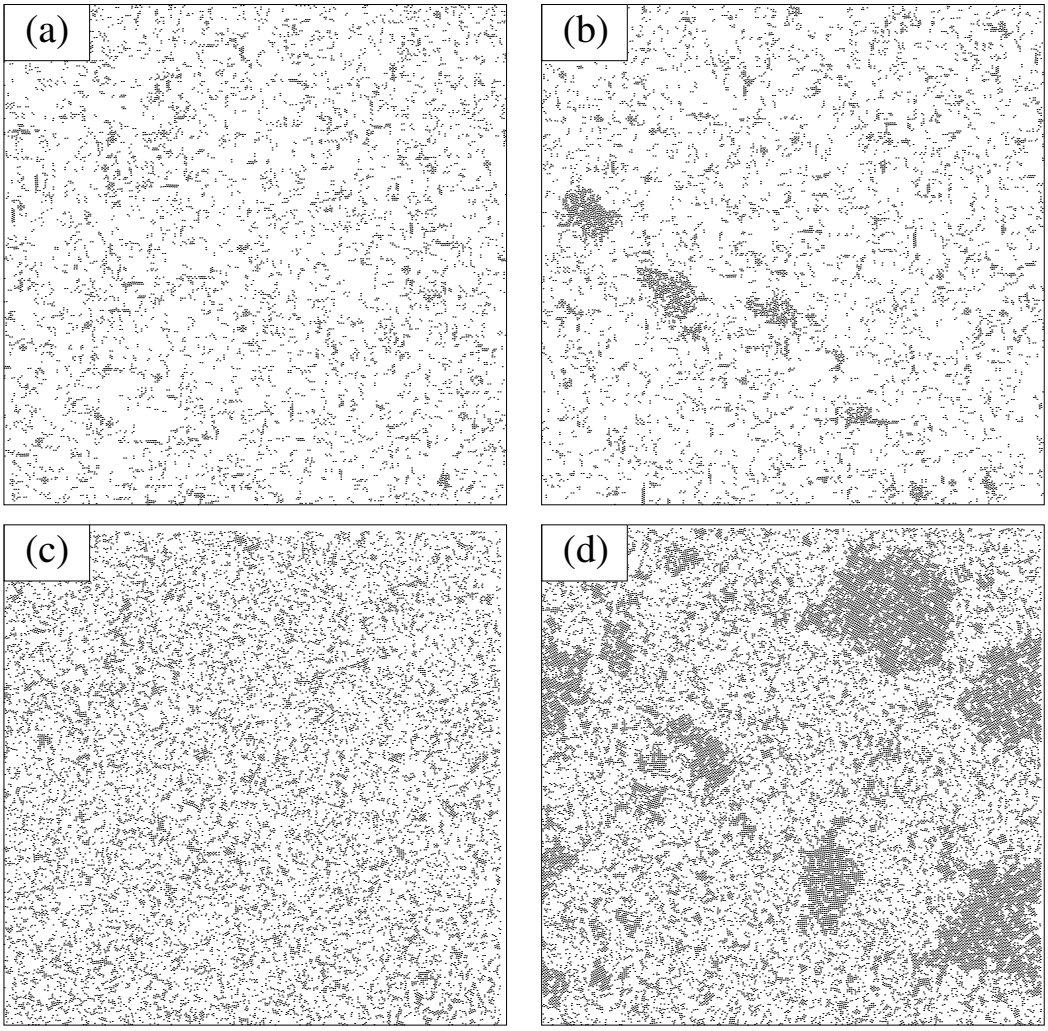

Figure 4.11: Snapshot configurations from EDMD simulations showing liquid-like particles for (a) the metastable S phase at $k_BT/\epsilon = 0.30$ at $\tau = 36741$, and (b) the S phase melting at $k_BT/\epsilon = 0.29$ at $\tau = 74732$ and showing several distinct liquid domains; and configurations showing S-like particles for (c) the metastable L phase at $k_BT/\epsilon = 0.35$ at $\tau = 46459$ and (d) crystallizing L at $k_BT/\epsilon = 0.38$ at $\tau = 40000$. Density time series for these state points are shown in Fig. 4.10.

The system transforms to HDT for $k_BT/\epsilon \leq 0.38$, converts to L for $0.39 \leq k_BT/\epsilon \leq 0.41$, converts to S for $0.42 \leq k_BT/\epsilon \leq 0.48$ and converts to L for $k_BT/\epsilon \geq 0.50$. We note that at $k_BT/\epsilon = 0.39$, interestingly, we observe the appearance of the HDT phase prior to full melting. At $P\sigma^2/\epsilon = 7.9$, the S phase is lost. The system transforms to HDT for $k_BT/\epsilon \leq 0.38$ and to L for $k_BT/\epsilon \geq 0.39$. Similarly, at $P\sigma^2/\epsilon = 8.0$, the

system transforms to HDT for $k_BT/\epsilon \leq 0.39$ and to L for $k_BT/\epsilon \geq 0.40$. For all these state points for the original $b = \sqrt{2}\sigma$, the potential energy of the liquid is higher than that of S.

4.4.4 Ruling out hexatic and quasicrystal phases

In two dimensions, a crystal possesses medium-range translational order and long-range orientational order. Furthermore, there is the possibility that a crystal melts in two dimensions via a hexatic phase, which retains medium-range orientational order before encountering the liquid, at which point orientational order is only short-range. Additionally, in Figs. 4.8 and 4.11 we see that, based on our bond-order parameter criteria for identifying crystal-like and liquid-like particles, there are a large number of defects within each phase, i.e., many S-like particles in the L phase and vice versa.

To clarify the range of order, we focus on two state points for each phase near the low T melting point along $P\sigma^2/\epsilon = 5.6$: one for which the phase is thermodynamically stable and the other for which it is metastable, given our calculated phase boundaries. We choose S at $k_BT/\epsilon = 0.30$ (metastable), S at $k_BT/\epsilon = 0.40$ (stable), L at $k_BT/\epsilon = 0.29$ (stable) and L at $k_BT/\epsilon = 0.35$ (metastable), all for the $N = 65536$ for which the time series are plotted in Fig. 4.10. It is true that we have not quantified the effect of system size on the location of the phase boundaries, but the EDMD simulations themselves confirm that what we deem as metastable is not far from being unstable. For each state point we calculate $G_4(r)$, $G_{\vec{g}}(r)$, $g(r)$ and also $S(\vec{q})$, which is calculated from a single configuration taken from the time series. In Fig. 4.12(a), we plot the orientational correlation function $G_4(r)$ and see the expected behavior: the L phase decorrelates within ten particle diameters while S remains correlated at long range as $G_4(r)$ approaches a constant close to unity. Neither S nor L exhibit behavior in $G_4(r)$ that can be interpreted as hexatic-like.

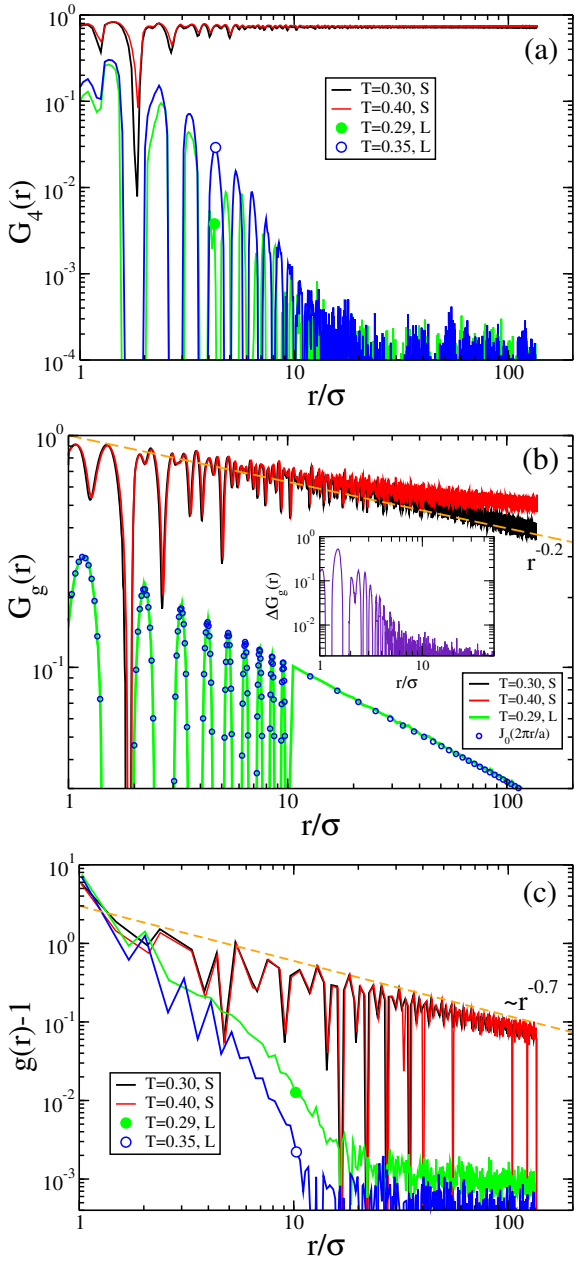

Figure 4.12: Orientational (a) and translational (b) correlation functions as well as (c) the peaks of $g(r) - 1$ for the $N = 65536$ system at $P\sigma^2/\epsilon = 5.6$ for the S phase at $k_BT/\epsilon = 0.30$, S at $k_BT/\epsilon = 0.40$, L at $k_BT/\epsilon = 0.29$ and L at $k_BT/\epsilon = 0.35$. In panel (a) $G_4(r)$ reaches a constant for S, while decaying exponentially for L. In panel (b) $G_{\vec{g}}(r)$ decays as a power law for S. For L, $G_{\vec{g}}(r)$ is described by a Bessel function $J_0(2\pi r/a)$, which is the analytic result for a random system. For L and $J_0(2\pi r/a)$, we plot only the peaks for $r > 10\sigma$. The inset shows exponential decay in $G_{\vec{g}}(r)$ for L once the vector $\vec{g}$ is chosen to align with local environments and after $J_0(2\pi r/a)$ is subtracted. In (c), $g(r)$ decays exponentially in the liquid, and as a power law with exponent ~ 0.7 for the S phase.

From the translational correlation functions plotted in Fig. 4.12(b) we see that for the S phase, $G_{\vec{g}}(r)$ decays as a power law with an exponent of roughly $\sim 0.1-0.2$, which is smaller in magnitude than 1/3, the value expected for triangular 2D crystals near the transition to the hexatic phase. For the liquid, $G_{\vec{g}}(r)$ is smaller in magnitude than for S and oscillates about zero, and the peaks decay as a power law with an exponent equal to 1/2. While this power-law decay is perhaps at first surprising, and indeed the same behavior has been observed in experiments on colloids [76], it is not an indication of quasi-long-range order. Rather, if one calculates $G_{\vec{g}}(r)$ by averaging over uniformly distributed orientational environments, then one obtains,

$$G_{\vec{g}}(r) = \frac{1}{\pi}\int_0^{\pi} \cos\left(\frac{2\pi r}{a}\cos(\phi)\right) d\phi = J_0\left(\frac{2\pi r}{a}\right), \tag{4.17}$$

where ϕ is the angle between $\vec{g}$ and $\vec{r}_j$ in Eq. 4.12, and $J_0(r)$ is the Bessel function of the first kind. The blue open circles in Fig. 4.12(b) represent $J_0(2\pi r/a)$ averaged over the a values of the liquid configurations at $T = 0.29 k_B/\epsilon$ used to calculate $G_{\vec{g}}(r)$. The result shows a complete agreement with the $G_{\vec{g}}(r)$ of the liquid phase. We note that for the liquid curves in Fig. 4.12(b), for clarity, we only plot for $r > 10\sigma$ points corresponding to local peaks in $G_{\vec{g}}(r)$ and $J_0(r)$. $J_0(r)$ decays as $1/\sqrt{r}$, which accounts for the observed power law. Subtracting $J_0(2\pi r/a)$ from $G_{\vec{g}}(r)$ gives essentially noise and a correlation length of zero.

In calculating $G_{\vec{g}}(r)$ so far, $\vec{g}$ is constant, i.e., the reference system is that of the simulation box. This makes sense for a crystal, but choosing a lattice vector for the liquid must take into account local ordering. We therefore employ the method whereby every time we select a particle to be an origin, we use each of its closest four neighbors in turn to define the x direction, and then average over the four $\vec{g} = 2\pi/a\,\hat{x}$ reciprocal lattice vectors for that origin. Doing so catches local translational ordering

in the absence of a global orientation. The result is a larger correlation at small r for L, but nonetheless $G_{\vec{g}}(r)$ rapidly approaches the Bessel function result. To more clearly see the decay in correlation, we plot in the inset of Fig. 4.12(b) the quantity $\Delta G_{\vec{g}}(r) \equiv G_{\vec{g}}(r) - J_0(2\pi r/a)$, where $G_{\vec{g}}(r)$ now takes into account local orientation. The exponential decay in this case has a somewhat smaller length scale than what is seen in the orientational correlations for L, but at least the exponential decay is observed.

By contrast, a plot of the peaks of $g(r)$ in Fig. 4.12(c) distinguishes in a more straightforward way between the liquid and crystal in terms of the range of order. For the liquid, $g(r)$ shows an exponential decay with a similar length scale present in $G_4(r)$. For S, there is a power-law decay, with an exponent of approximately 0.7, significantly larger than the exponent for $G_{\vec{g}}(r)$.

As an additional measure of order we plot the structure factor in Fig. 4.13 for the same state points considered in Fig. 4.12. We use a single configuration for the calculation of $S(\vec{q})$, i.e., we do not average over many configurations, in order to avoid possible complications arising from rotations of crystal-like domains in time. The $S(\vec{q})$ for S [panels (a) and (b)] show peaks characteristic of a square crystal. While there are small hints of scattering for $\vec{q}$ in between the main points located at multiplies of $\sim 2\pi/\sigma$ in either q_x or q_y, the effect is rather weak compared to what is seen in other studies of the hexatic phase [76]. For the liquid, panels (c) and (d) show no hint of crystal-like peaks that might have appeared were there a hexatic phase. Neither do they show features consistent with a quasi-crystalline phase, for which the $S(\vec{q})$ plot exhibits ten equidistant peaks along circles of certain fixed $|\vec{q}|$, indicating the presence of five-fold symmetry [25].

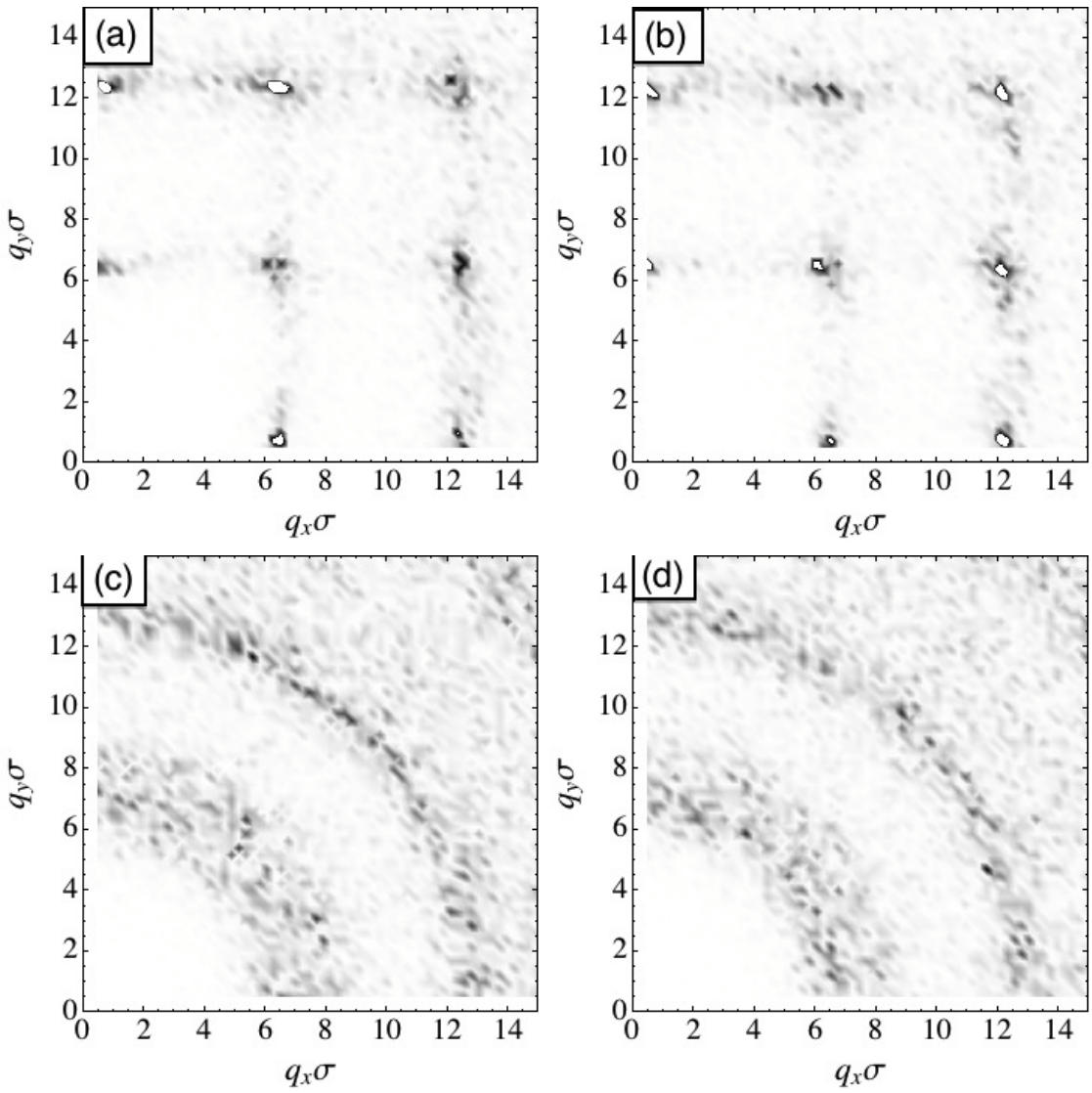

Figure 4.13: Structure factor for the $N = 65536$ system at $P\sigma^2/\epsilon = 5.6$ for the (a) S phase at $k_BT/\epsilon = 0.30$, (b) S at $k_BT/\epsilon = 0.40$, (c) L at $k_BT/\epsilon = 0.29$ and (d) L at $k_BT/\epsilon = 0.35$. The grey scale indicates the value of $S(\vec{q})$ and saturates at a value of 25, which is just above the largest value for the liquid (large peaks for the S phase appear as white spots with black edges).

4.5 Discussion and conclusions

In this study, we vary the parameters ϵ_1, b and c of the SSSW potential and find that increasing b (the extent of the shoulder) has the greatest impact on increasing the range of P over which inverse melting takes place. Recalculating the melting curve

for several values of b, we find that the stability field of the S phase shrinks as a whole while making the effect of inverse melting more pronounced.

For the $b = 1.46\sigma$ case, we confirm the melting line predicted by the combination of several MC free energy methods now becoming standard in the calculation of phase diagrams by carrying out biased simulations of a phase-separated system. From these simulations, we estimate the interfacial tension at the inverse melting line ($P\sigma^2/\epsilon = 5.6$, $k_BT/\epsilon = 0.340$) to be $\beta\gamma\sigma = 0.075$. This value is rather low compared to crystallization in three dimensions, e.g., $\beta\gamma\sigma^2 = 0.5$ for hard spheres [77], but is consistent with the rather diffuse interface at coexistence. A small surface tension is also consistent with our earlier observations of a small range of metastability of the liquid with respect to crystallization in general for this model despite only a small difference in chemical potential at the edge of metastability [24].

The large region of inverse melting for $b = 1.46\sigma$ facilitates direct testing by EDMD simulations. For both large and small systems, we confirm the first-order nature of the transition as well as the general location of the transition.

Using the large systems, we test for the range of order. The orientational correlation function as well as $g(r)$ clearly find the S phase to be a crystal and L phase to be a liquid. No hexatic phase is apparent at the point along the melting line where we carry out our analyses. The structure factor likewise supports these findings. This is consistent with recent work on a simpler repulsive-shoulder model in 2D that has a similar phase diagram to ours, and finds a hexatic phase only at low density [78]. Additionally, the structure factor indicates the absence of a quasicrystal phase.

As for the translational correlation function [$G_{\vec{g}}(r)$], it decays as a power law with a small exponent for S as is expected. For the liquid, some care must be taken before exponential decay is made apparent. First, the orientation of the local environment of each origin used in averaging should be taken into consideration when defining lattice

vectors. Second, one should take into account that the analytical expression for $G_{\vec{g}}(r)$ in the case where orientations are uniformly distributed is a Bessel function, for which oscillations decay in amplitude as a power law. Thus a spurious power-law decay in translational correlation arises in a completely random system.

Inverse melting in this system, because of the simplicity of the radial pair potential, hopefully will lend itself to analytical treatment [79]. A more theoretical analysis might be beneficial to understanding the impact of other modifications to the potential on inverse melting, and may thus facilitate producing inverse melting in other 2D systems that are governed by similar potentials, such as lipid membranes [80].

Acknowledgments

AMA and IS-V thank NSERC for funding, ACEnet for funding and computational support and CFI for funding of computing infrastructure. SVB acknowledges the partial support of this research through the Dr. Bernard W. Gamson Computational Science Center at Yeshiva College.

Bibliography

[1] F. H. Stillinger and P. G. Debenedetti, Biophys. Chem. **105**, 211 (2003).

[2] S. Angioletti-Uberti, B. M. Mognetti, and D. Frenkel, Nat. Mater. **11**, 518 (2012).

[3] O. Gang, Nat. Mater. **11**, 487 (2012).

[4] E. R. Dobbs, Helium Three, Oxford University Press, Oxford, 2000.

[5] C. Le Pair, K. W. Taconis, R. De Bruyn Ouboter, and P. Das, Physica **29**, 755 (1963).

[6] J. Wilks, The Properties of Liquid and Solid Helium, Clarendon Press, Oxford, 1967.

[7] S. Rastogi, M. Newman, and A. Keller, Nature **353**, 55 (1991).

[8] S. Rastogi, M. Newman, and A. Keller, J. Polym. Sci. B **31**, 125 (1993).

[9] S. Rastogi, G. W. H. Höhne, and A. Keller, Macromolecules **32**, 8897 (1999).

[10] A. L. Greer, Nature **404**, 134 (2000).

[11] C. S. J. van Hooy-Corstjens, G. W. H. Höhne, and S. Rastogi, Macromolecules **38**, 1814 (2005).

[12] M. R. Feeney, P. G. Debenedetti, and F. H. Stillinger, J. Chem. Phys. **119**, 4582 (2003).

[13] N. Schupper and N. M. Shnerb, Phys. Rev. Lett. **93**, 037202 (2004).

[14] P. E. Cladis, D. Guillon, F. R. Bouchet, and P. L. Finn, Phys. Rev. A **23**, 2594 (1981).

[15] K. Mortensen, W. Brown, and B. Nordén, Phys. Rev. Lett. **68**, 2340 (1992).

[16] M. Plazanet, C. Floare, M. R. Johnson, R. Schweins, and H. P. Trommsdorff, J. Chem. Phys. **121**, 5031 (2004).

[17] R. Angelini and G. Ruocco, Philos. Mag. **87**, 553 (2007).

[18] R. Angelini, G. Ruocco, and S. De Panfilis, Phys. Rev. E **78**, 020502(R) (2008).

[19] N. Avraham, B. Khaykovich, Y. Myasoedov, M. Rappaport, H. Shtrickman, D. E. Feldman, T. Tamegai, P. H. Kes, M. Li, M. Konczykowski, K. van der Beek, and E. Zeldov, Nature **411**, 451 (2001).

[20] H. Beidenkopf, N. Avraham, Y. Myasoedov, H. Shtrikman, E. Zeldov, B. Rosenstein, E. H. Brandt, and T. Tamegai, Phys. Rev. Lett. **95**, 257004 (2005).

[21] W. Kauzmann, Chem. Rev. **43**, 219 (1948).

[22] E. Tombari, C. Ferrari, G. Salvetti, and G. P. Johari, J. Chem. Phys. **123**, 051104 (2005).

[23] S. Roldán-Vargas, F. Smallenburg, W. Kob, and F. Sciortino, Sci. Rep. **3**, 2451 (2013).

[24] A. M. Almudallal, S. V. Buldyrev, and I. Saika-Voivod, J. Chem. Phys. **137**, 034507 (2012).

[25] A. Skibinsky, S. V. Buldyrev, A. Scala, S. Havlin, and H. E. Stanley, Phys. Rev. E **60**, 2664 (1999).

[26] P. C. Hemmer and G. Stell, Phys. Rev. Lett. **24**, 1284 (1970).

[27] G. Stell and P. C. Hemmer, J. Chem. Phys. **56**, 4274 (1972).

[28] A. R. Denton and H. Löwen, J. Phys.: Condens. Matter **9**, L1 (1997).

[29] A. R. Denton and H. Löwen, J. Phys.: Condens. Matter **9**, 8907 (1997).

[30] K. K. Mon, N. W. Ashcroft, and G. V. Chester, Phys. Rev. B **19**, 5103 (1979).

[31] M. Selbert and W. H. Young, Phys. Lett. A **58**, 469 (1976).

[32] D. Levesque and J. J. Weis, Phys. Lett. A **60**, 473 (1977).

[33] J. M. Kincaid and G. Stell, Phys. Lett. A **65**, 131 (1978).

[34] P. T. Cummings and G. Stell, Mol. Phys. **43**, 1267 (1981).

[35] E. Velasco, L. Mederos, G. Navascués, P. C. Hemmer, and G. Stell, Phys. Rev. Lett. **85**, 122 (2000).

[36] A. Voronel, I. paperno, S. Rabinovich, and E. Lapina, Phys. Rev. Lett. **50**, 247 (1983).

[37] P. Kumar, S. Han, and H. E. Stanley, J. Phys.: Condens. Matter **21** 504108 (2009).

[38] P. G. Debenedetti and H. E. Stanley, Phys. Today **56**, 40 (2003).

[39] F. X. Prielmeier, E. W. Lang, R. J. Speedy, and H. D. Lüdemann, Phys. Rev. Lett. **59**, 1128 (1987).

[40] G. S. Kell, J. Chem. Eng. Data **20**, 97 (1975).

[41] P. H. Poole, F. Sciortino, U. Essmann, and H. E. Stanley, Nature **360**, 324 (1992).

[42] C. H. Cho, S. Singh, and G. W. Robinson, Phys. Rev. Lett. **76**, 1651 (1996).

[43] M. R. Sadr-Lahijany, A. Scala, S. V. Buldyrev, and H. E. Stanley, Phys. Rev. Lett. **81**, 4895 (1998).

[44] M. R. Sadr-Lahijany, A. Scala, S. V. Buldyrev, and H. E. Stanley, Phys. Rev. E **60**, 6714 (1999).

[45] E. A. Jagla, J. Chem. Phys. **111**, 8980 (1999).

[46] E. A. Jagla, Phys. Rev. E **63**, 061501 (2001).

[47] E. A. Jagla, Phys. Rev. E **63**, 061509 (2001).

[48] A. Scala, M. R. Sadr-Lahijany, N. Giovambattista, S. V. Buldyrev, and H. E. Stanley, Phys. Rev. E **63**, 041202 (2001).

[49] S. V. Buldyrev, G. Franzese, N. Giovambattista, G. Malescio, M. R. Sadr-Lahijany, A. Scala, A. Skibinsky, and H. E. Stanley, Physica A **304**, 23 (2002).

[50] S. Prestipino, F. Saija, and P. V. Giaquinta, J. Chem. Phys. **137**, 104503 (2012).

[51] G. Franzese, G. Malescio, A. Skibinsky, S. V. Buldyrev, and H. E. Stanley, Nature **409**, 692 (2001).

[52] P. Mausbacha and H. O. May, Fluid Phase Equilibr **214**, 1 (2003).

[53] D Quigley and M. I. J. Probert, Phys. Rev. E **71**, 065701(R) (2005).

[54] T. Head-Gordon and F. H. Stillinger, J. Chem. Phys. **98**, 3313 (1993).

[55] F. H. Stillinger and T. Head-Gordon, Phys. Rev. E **47**, 2484 (1993).

[56] M. Huš and T. Urbic, J. Chem. Phys. **139**, 114504 (2013).

[57] D. Frenkel and Berend Smit, *Understanding Molecular Simulation: From algorithms to Applications*, San Diego, Academic Press, 2002.

[58] M. P. Allen and D. J. Tildesley, Computer Simulation of Liquids, Oxford University Press, New York, 1989.

[59] D. C. Rapaport, The Art of Molecular Dynamic Simulation, Cambridge University Press, Cambridge, 1995.

[60] B. J. Adler and T. E. Wainwright, J. Chem. Phys. **31**, 459 (1959).

[61] B. D. Lubachevsky, J. Comput. Phys. **94**, 255 (1991).

[62] D. Frenkel and A. J. C. Ladd, J. Chem. Phys. **81**, 3188 (1984).

[63] B. Barboy and W. M. Gelbart, J. Chem. Phys. **71**, 3053 (1979).

[64] M. G. Noro and D. Frenkel, J. Chem. Phys. **114**, 2477 (2001).

[65] D. Henderson, Mol. Phys. **30**, 971 (1975).

[66] T. Boublík, Mol. Phys. **109**, 1575 (2011).

[67] D. A. Kofke, Mol. Phys. **78**, 1331 (1993).

[68] D. A. Kofke, J. Chem. Phys. **98**, 4149 (1993).

[69] C. Vega, E. Sanz, J. L. F. Abascal, and E. G. Noya, J. Phys.: Condens. Matter, **20**, 153101 (2008).

[70] F. Romano, E. Sanz, and F. Sciortino, J. Chem. Phys, **132**, 184501 (2010).

[71] S. J. Singer and R. Mumaugh, J. Chem. Phys. **93**, 1278 (1990).

[72] M. R. Shirts and J. D. Chodera, J. Chem. Phys. **129**, 124105 (2008). We use the "pymbar-2.0beta" implementation of the MBAR method available from https://simtk.org/home/pymbar.

[73] P. J. Steinhardt, D. R. Nelson, and M. Ronchetti, Phys. Rev. B **28**, 784 (1983).

[74] U. Gasser, J. Phys.: Condens. Matter **21** 203101 (2009).

[75] E. P. Bernard and W. Krauth, Phys. Rev. Lett. **107**, 155704 (2011).

[76] A. Brodin, A. Nych, U. Ognysta, B. Lev, V. Nazarenko, M. Skarabot, and I. Musevic, Condens. Matter Phys. **13**, 33601 (2010).

[77] S. Auer and D. Frenkel, J. Chem. Phys. **120**, 3015 (2004).

[78] D.E. Dudalov, Yu.D. Fomin, E.N. Tsiok, and V.N. Ryzhov, arXiv:1311.7534v1 (2013).

[79] T. Urbic, J. Chem. Phys. **139**, 164515 (2013).

[80] M. Nielsen, L. Miao, J. H. Ipsen, M. J. Zuckermann, and O. G. Mouritsen, Phys. Rev. E **59**, 5790 (1999).

Chapter 5

High-Pressure Phases in a System with Inverse Melting

5.1 Abstract

We perform NPT MC simulations to study the phase behaviour of the SSSW model, with $b = 1.46\sigma$, at high pressure. The triple point seen in the original model vanishes, leading to a "liquid corridor" of liquid stability. We find a new crystal phase that may thwart the liquid from achieving thermodynamic stability to very low temperature. A "funny point", where the free energy barrier between liquid and HDT phase vanishes, appears along the HDT melting line. While this funny point appears to be connected to a previously undiscovered transition between low and high temperature forms of HDT, its explanation remains a mystery. Through using scaling laws and Binder cumulants to help us determine the order of the transition between the two HDT forms, we find that using isotropic pressure scaling significantly impacts the transition despite having a candidate structure for the low-T phase that shares the same simulation box geometry of the high-T phase.

5.2 Introduction

Having calculated the phase diagram of the SSSW model and then found model parameters that greatly enhance the extent of inverse melting, we now turn our attention to the phase behaviour at high density of the model. We are interested specifically in the melting line of the high density triangular (HDT) crystal and its relation to the anomalous square (S) melting curve, i.e., near inverse melting in the case that inverse melting is a strong effect.

While completeness of the phase diagram provides sufficient justification for exploring the phase behaviour of the HDT crystal, the shape of the melting line of S sets up the following interesting scenario. As the parameter b is increased, as we have seen in the previous chapter, the slope of the S melting line near the HDT-S-L triple point becomes progressively more vertical. If the triple point is to remain at the low T side of the inverse melting part of the S melting curve, then the HDT melting line in this vicinity must also become progressively more vertical.

An HDT melting line that is significantly vertical is problematic. The HDT phase, a relatively high energy phase, forms because of its efficient packing; it is mechanically driven. A vertical melting line implies that the transition is driven by the presence of a lower energy phase at lower temperature, i.e., from the Clausius-Clapeyron equation we see that a vertical line implies no volume change and hence that the transition is not mechanically driven. Given that the HDT phase is rather high in energy compared to the liquid, this would be somewhat paradoxical.

Another scenario is that the HDT melting line remains horizontal. Then the question is at what pressure does HDT melting occur in relation to the pressure maximum in the S melting line that demarcates the beginning of inverse melting? If the pressure of the HDT-L line is significantly lower, then the HDT-S-L triple point will move to significantly higher T along the S-L curve, relegating the phenomenon

of inverse melting to the metastable liquid regime. If it (the HDT melting pressure) is significantly higher than the S-L pressure maximum, then the HDT-L and S-L will no longer intersect, resulting in the disappearance of the HDT-S-L triple point altogether.

The simulation techniques used to generate the results in this chapter are the same as those used previously, and as such we simply extend them to the model investigated in detail in Chapter 4, namely the SSSW with $N = 1024$ hard disks with diameter $a = \sigma$, shoulder of energy -0.5ϵ and extent $b = 1.46\sigma$ and a deeper well of energy $-\epsilon$ and extent $c = \sqrt{3}\sigma$. The model again provides a few surprises.

5.3 Results and Discussion

5.3.1 New phase diagram

Before presenting new results and to provide a reference, we reproduce in Fig. 5.1(a) the P-T phase diagram for the original model ($b = \sqrt{2}\sigma$). In Fig. 5.1(b), we plot the P-T phase diagram for the $b = 1.46\sigma$ model, obtaining the HDT-L line from density histograms wherever free energy barriers are sufficiently low for good histogram statistics to be obtained, and with Gibbs-Duhem integration otherwise. The S-L curve is from Chapter 4. We must note that during all these calculations, the simulation box shape does not change as we do not expect the HDT phase to change symmetry. That is to say, we maintain constant P through isotropic volume changes of the box.

The most striking feature, and the one we first point out, is the disappearance of the triple point. This, along with the inflection near $k_BT/\epsilon = 0.4$ that results in the HDT-L becoming more horizontal again at lower T, is consistent with HDT formation being driven by its more efficient packing upon compression as opposed to energetic considerations.

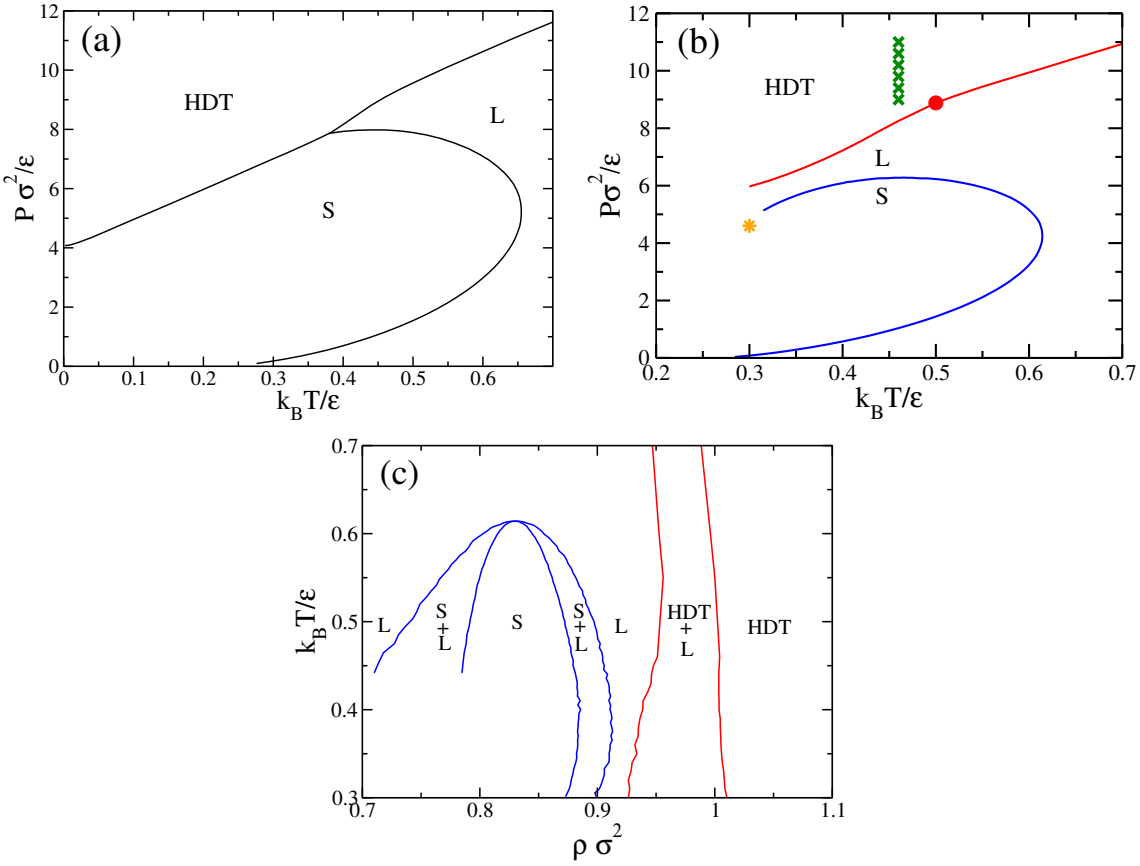

Figure 5.1: Panel (a) shows the P-T phase diagram for the original SSSW model with $b = \sqrt{2}\sigma$. Panels (b) and (c) show the phase diagram for the $b = 1.46\sigma$ model in the P-T and ρ-T planes, respectively. In (b), the green $\times$'s indicate a transition between high and low T forms of HDT, the filled red circle a "funny point" at which the free energy barrier between HDT and L seems to disappear, and the orange star marks the state point from which a snapshot configuration is shown in Fig. 5.2.

With the triple point removed and given the curvatures of the HDT-L and S-L lines, there is the tantalizing possibility that the "corridor" of stability of the liquid extends to very low T. This corridor is also quite evident in the ρ-T phase diagram in Fig. 5.1(c), where the system remains thermodynamically free of HDT and S crystal down to the lowest T studied along $\rho\sigma^2 \approx 0.92$. In a preliminary confirmation of this, EDMD simulations at $k_BT/\epsilon = 0.30$ and $\rho\sigma^2 = 0.92$ have so far not shown any evidence of crystallization. However, as we shall see later, our hopes for finding a liquid that is thermodynamically stable down to $T = 0$ liquid, as found in Ref. [1], are

likely short lived. It seems that nature abhors liquid corridors in addition to vacuums; the system does not appear to be content in allowing for a liquid stable at low T and instead conjures up new crystal phases.

The second feature we observe is an apparent transition line occurring within the HDT stability fields, which appears to separate low-T and a high-T forms of HDT. This line, indicated by green $\times$'s in Fig. 5.1(b), is quite vertical and therefore seems to imply a transition chiefly driven by energetic differences between the two forms with practically no density change.

The third feature, represented by a large filled red circle in Fig. 5.1(b), marks a point at which the free energy barrier separating L and HDT vanishes, or at least is indistinguishable from the noise in our calculations. This is quite surprising for us to see, and not being able to characterize currently, we call it the "funny point". At first glance, the funny point appears to be independent of the low-T to high-T HDT transition, as it occurs at a T significantly greater than that of the intra-HDT transition.

In what follows, we shall address each of these three oddities in turn.

5.3.2 The liquid corridor

The liquid corridor at $\rho = 0.92$ begs two immediate questions. One, is there anything obviously special about the liquid's structure that renders it more stable than the crystals present at both higher and lower ρ? Two, what new crystals might exist in this part of the phase diagram? Fortunately, the answer to the first question provides answers to the second as well.

In Fig. 5.2, we show a snapshot configuration taken from the liquid at $k_BT/\epsilon = 0.30$ and $P\sigma^2/\epsilon = 4.60$, the orange point indicated in Fig. 5.1(b). To help the eye distinguish patterns, we connect neighbouring particles with red lines, and also over-

lay colourful triangles, squares (or rhomboids) and pentagons over minimal rings of particles for two particular regions of the liquid. Additionally, in a few places we have highlighted regions of square (large squares) and triangular (large hexagons) local packing.

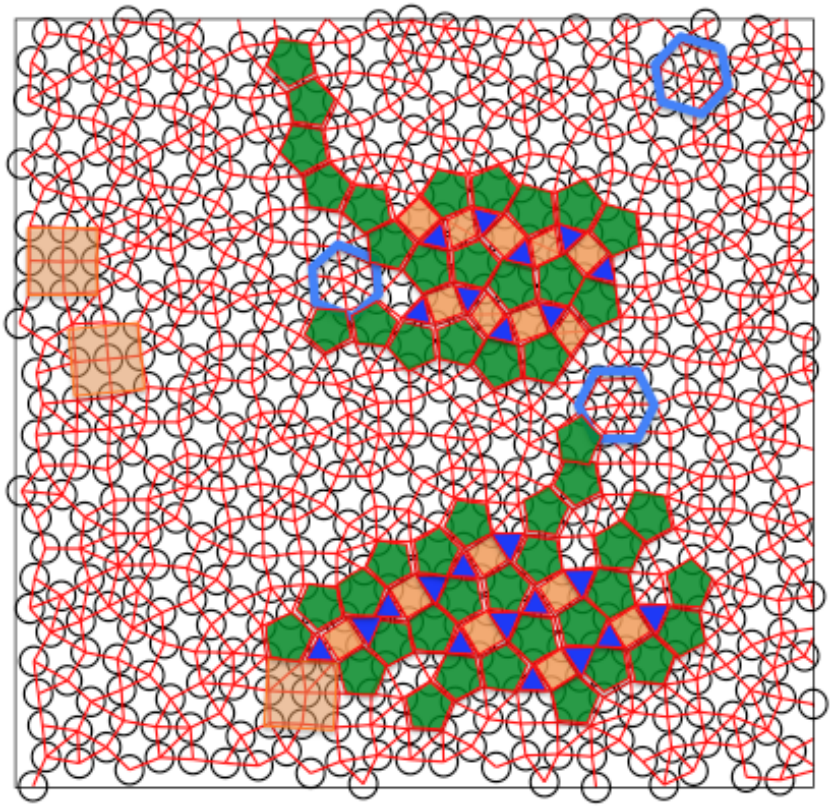

Figure 5.2: A snapshot configuration of the liquid phase taken at $k_BT/\epsilon = 0.30, P\sigma^2/\epsilon = 4.60$. Red lines connect neighbouring particles, while the overlaid geometrical figures are a guide to the eye in order to show different local environments. The upper colourful area shows a tiling of pentagons, triangles and squares forming the O crystal, while the lower one shows the I crystal.

While the large variety of local environment is immediately apparent, so are the two distinct tiling patterns present in the two chosen regions overlaid with triangles, squares and pentagons. While the tiled regions are rather large, the repeated patterns do not extend across the system; at some point "strings" of face-sharing pentagons end. However, the tilings are clearly crystalline and we extract two crystal structures,

I and O, shown in Fig. 5.3(a) and Fig. 5.3(b). These two crystals have been previously discovered and studied in a model similar to ours, except consisting of only a hard core and a square well of extent $\sqrt{3}\sigma$ [2]. For the model in that work, the tilings produced a quasi-crystal phase, as noted in Chapter 4. In principle, such a phase might still be found in the SSSW model.

As a first step in determining the range of thermodynamic stability of the I and O phases, we carry out NPT MC simulations over a range of P and T for 2×10^8 steps and note whether the phase persists for that state point (determined from a lack of change in the energy and density time series as well as a visual inspection of the final configuration). A sampling of such points for each phase is shown in the phase diagram in Fig. 5.3(c), along with data for the L, HDT and S phases as well. The lower energy I phase has a rather large field of stability (or metastability). Given that the O phase has a higher energy than the I phase, and that the region in P-T space where it persists is a subset of that for the I phase, we would expect that the O phase is completely metastable with respect to the I phase. Nonetheless, free energy calculations are needed to determine the true transition lines between the I phase and the others. It is certainly reasonable, however, that we have a good candidate crystal for plugging the liquid corridor.

5.3.3 The two HDT phases

The green $\times$'s plotted in Fig. 5.1(b) demarcate an apparent transition between two forms of HDT, evidence for which comes from the behaviour of the enthalpy per particle h as a function of T along a few isobars, which we plot in Fig. 5.4(a) for a few system sizes. As the system size increases, the inflection in $h(T)$ becomes sharper. These inflection points by definition correspond to maxima in the constant pressure

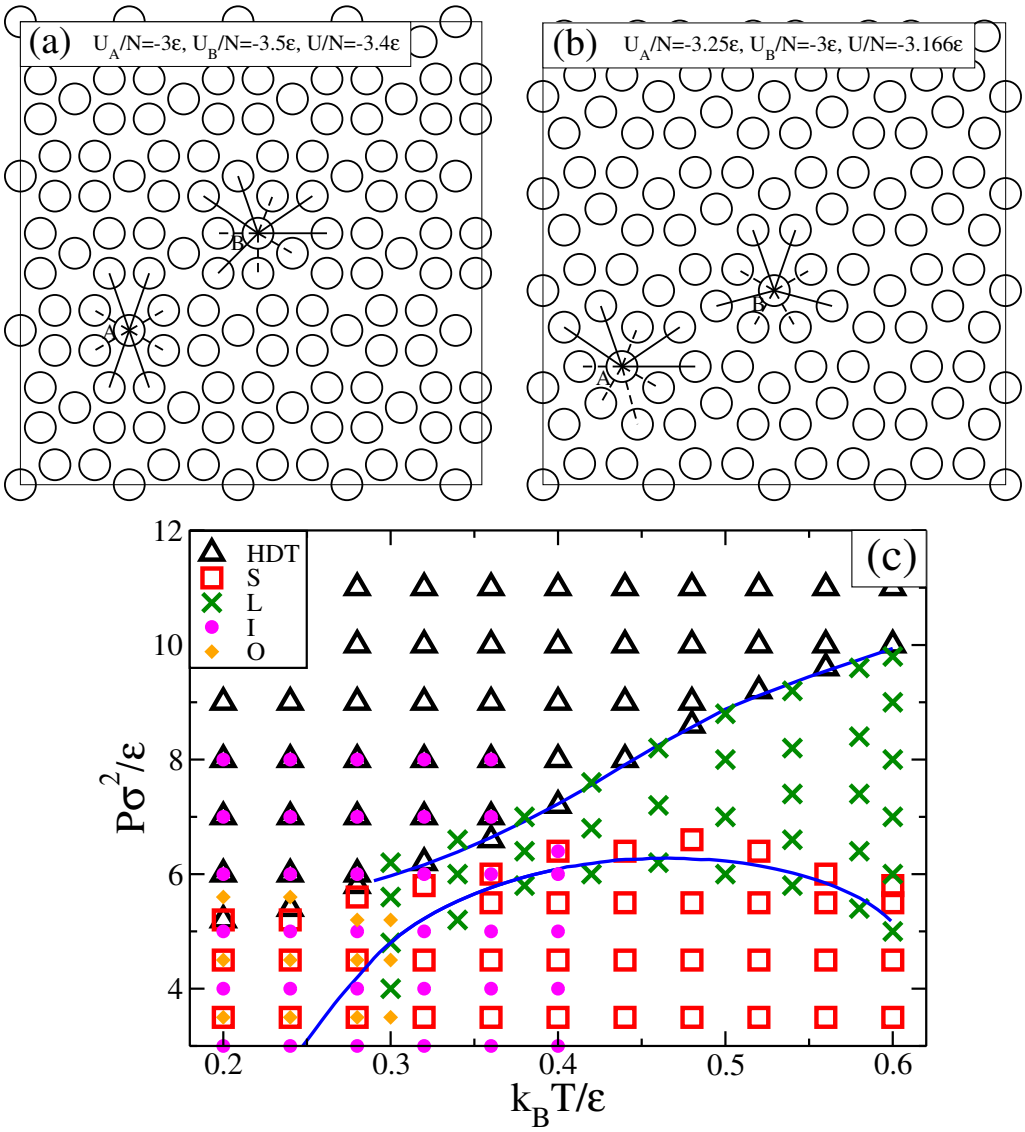

Figure 5.3: Panel (a) shows an ideal configuration of the I crystal with potential energy per particle -3.4ϵ, and panel (b) shows the O phase, with potential energy per particle -3.166ϵ. Line segments indicate a bond with energy $-\epsilon$ and a dashed line segment one with energy $-\epsilon/2$. Panel (c) shows the phase diagram presented in Fig. 5.1(b) with symbols indicating the extent of metastability of each phase (except that for L, simulations are only performed down to $k_BT/\epsilon = 0.3$).

heat capacity, which we define and calculate as a dimensionless per particle quantity,

$$C_P = \frac{\langle h^2 \rangle_{P,T} - \langle h \rangle_{P,T}^2}{N k_B^2 T^2}. \tag{5.1}$$

A plot of C_P in Fig. 5.4(b) shows these peaks growing in height and moving to higher T as N increases. The growth of the specific heat peak (of height $C_{P_{\max}}$) with system size is indicative of a transition, as opposed to something like a Schottky anomaly, which should not increase with N. The positions of the green $\times$'s in Fig. 5.1(b) are given by the T of the maxima in C_P for $N = 986$ (the size for which the other phases in the phase diagram are simulated).

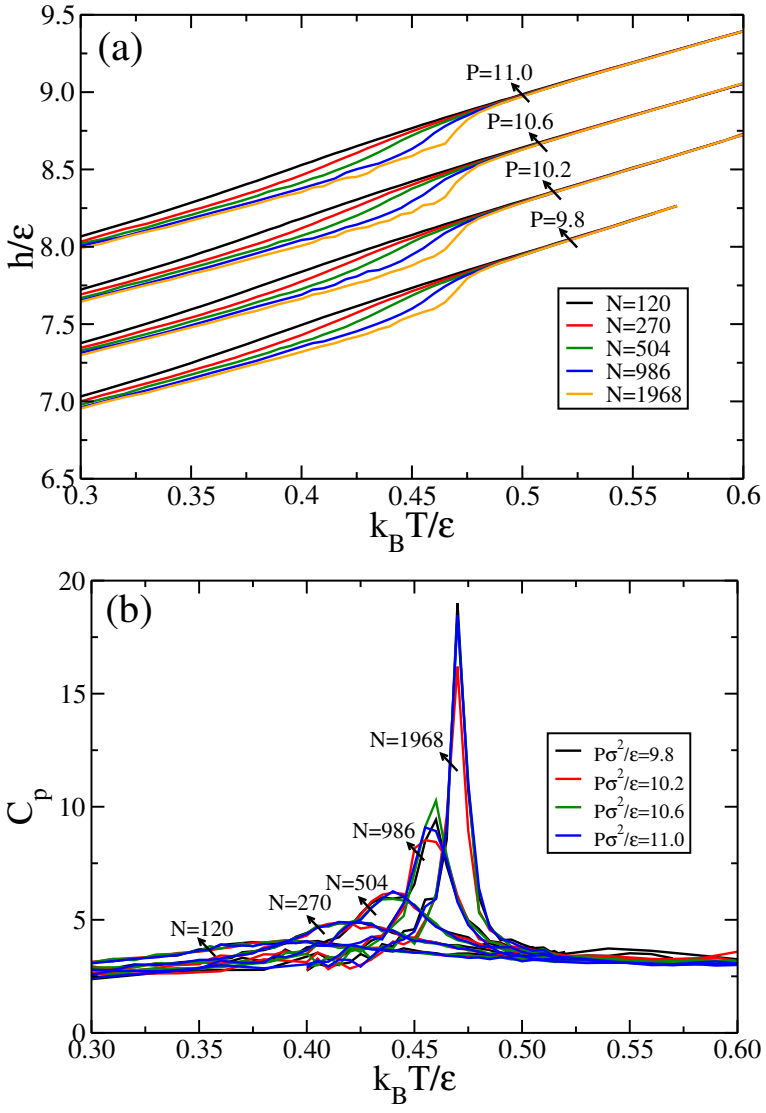

Figure 5.4: Evidence for a transition between high and low T forms of HDT: (a) enthalpy per particle as a function of T calculated along different isobars for different system sizes; (b) corresponding specific heat calculated according to Eq. 5.1.

To get a rough sense of what this transition might entail, we show snapshot configurations from simulations along the $P\sigma^2/\epsilon = 9.8$ isobar in Fig. 5.5 at T (a) near but below, (b) near but above the location of $C_{P_{\max}}$, as well as for (c) above the melting line. Below the transition [Fig. 5.5(a), $k_BT/\epsilon = 0.40$], there are large, well ordered domains. The boundaries between domains are somewhat subtle. If one looks closely within a domain, one can see that the local ordering is not as symmetric as it ought to be for a triangular crystal and is perhaps somewhat skewed. While this is imprecise and may arise from stresses due to domain walls and other defects, it is something perhaps to keep in mind. It is not obvious how this structure departs from the ideal triangular crystal. The configuration from above the transition in Fig. 5.5(b) ($k_BT/\epsilon = 0.50$), there is rather more disorder as one should expect (greater vibrational entropy in the higher T phase). For the configuration at $k_BT/\epsilon = 0.60$ in Fig. 5.5(c) (above melting), it is difficult to discern any long range order, as is expected.

To view these phases in a more quantitative way, we plot corresponding $g(r)$ in Fig. 5.6(a). The two HDT phases exhibit behaviour expected from crystals: sharp and slowly decaying peaks. The low-T phase shows peaks that are absent in the high-T phase, indicating a real structural difference between the two. For comparison, the $k_BT/\epsilon = 0.60$ curve shows typical liquid behaviour.

The orientational correlation functions plotted in Fig. 5.6(b), which plateau to a constant, are also consistent with the two forms of HDT being crystals. Above melting, $G_6(r)$ decays exponentially. Along with the $g(r)$ data, these findings confirm that we have not encountered a hexatic phase, and that both the low-T and high-T forms of HDT are crystal, at least near the transition at the values of P we explore.

We now wish to explore the nature of the transition by re-examining the heat capacity data more closely. Whether the transition is (weakly) first order or second order, $C_{P_{\max}}$ should scale as a power law with N [3–7]. The $C_{P_{\max}}$ data plotted in

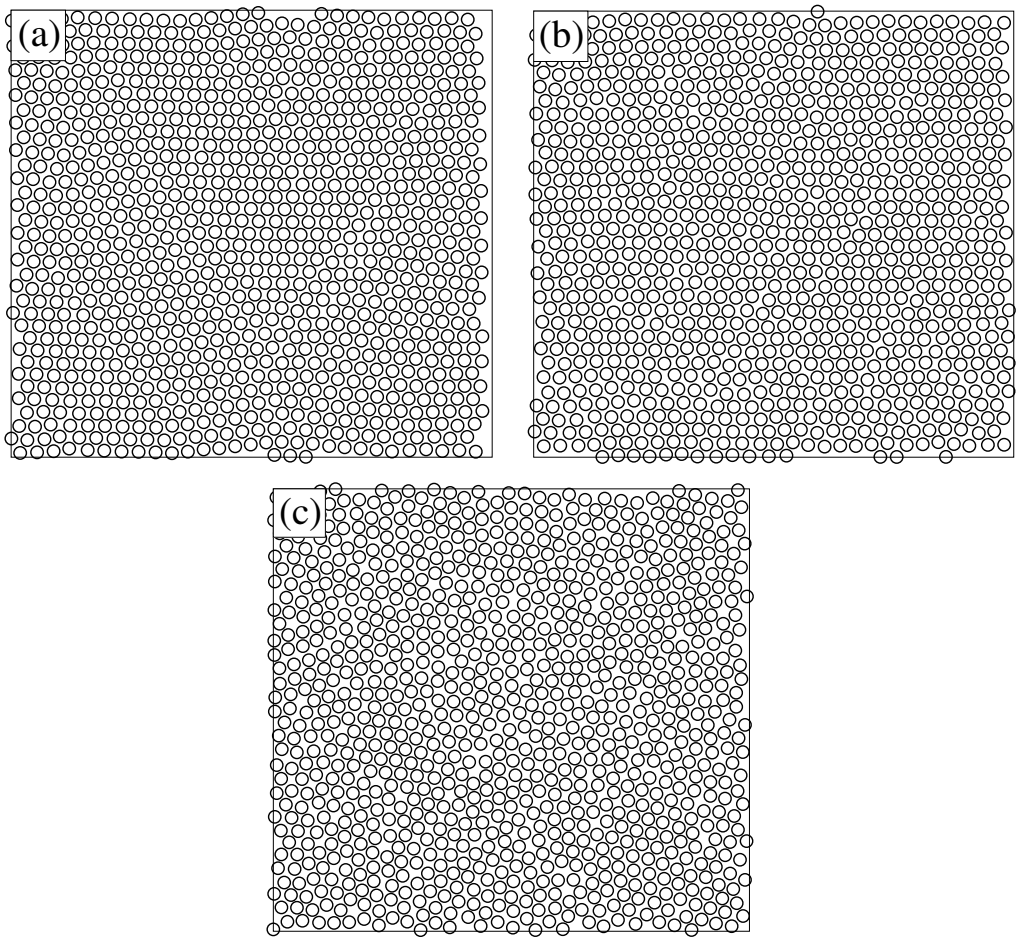

Figure 5.5: Snapshots configurations taken along the isobar $P\sigma^2/\epsilon = 9.8$, (a) low-T HDT at $k_BT/\epsilon = 0.40$, (b) high-T HDT at $k_BT/\epsilon = 0.50$, and (c) L at $k_BT/\epsilon = 0.60$.

Fig. 5.7(a) clearly show that this is not the case. Perhaps for the largest system sizes, we are entering the size regime where scaling holds.

In another attempt to observe scaling laws, we note that for second order transitions, $C_P(T)$ can be rescaled to collapse into a single scaling function that is independent of system size according to [5–7],

$$C_P(T) = L^{\alpha/\nu} f\left(\frac{T - T_c}{T_c} L^{1/\nu}\right), \tag{5.2}$$

where α is the critical exponent associated with the power-law divergence of $C_P(T)$

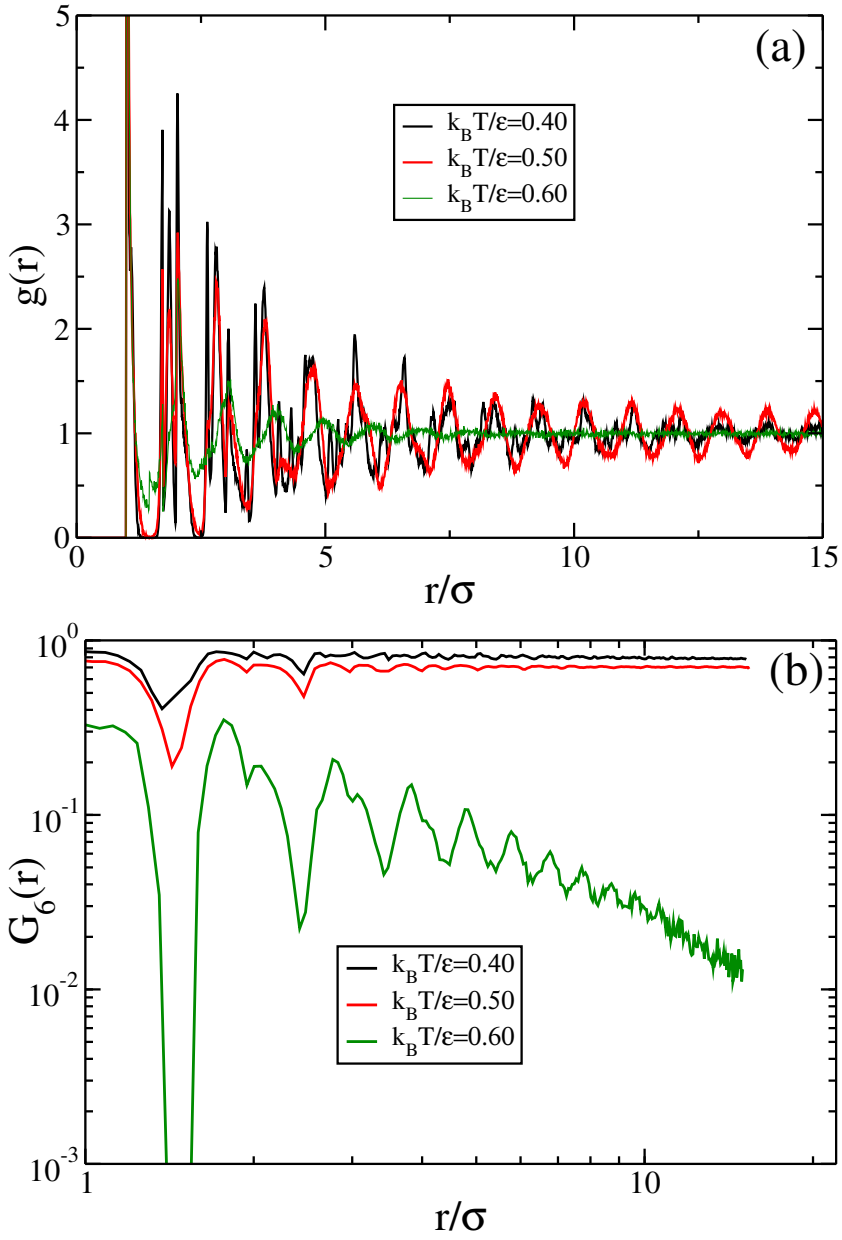

Figure 5.6: Pair distribution functions plotted in (a) show structural differences between low-T ($k_BT/\epsilon = 0.40$) and high-T ($k_BT/\epsilon = 0.50$) forms of HDT (there are missing peaks in the high-T form), and only short range correlations in L ($k_BT/\epsilon = 0.60$), as expected. Corresponding orientational correlation functions in (b) show that both HDT forms are crystalline [$G_6(r)$ reaches a plateau], while L is indeed a liquid [exponential decay in $G_6(r)$].

near the critical temperature T_c, ν is the critical exponent describing the divergence of the correlation length scale upon approach to T_c, L is the simulation box length

and f is a scaling function. The Josephson relation $2 - \alpha = d\nu$, where $d = 2$ is the dimensionality of the system, reduces the number of unknown parameters to two: α and T_c.

We rescale $C(P)$ data for our largest three system sizes according to Eq. 5.2 over a range of potential values of α and T_c, searching out the values that provide the best collapse of the data. The search is aided by the fact that changing T_c only shifts the curves along the temperature axis. So although our search is done "by hand", our estimates $k_B T_c/\epsilon = 0.484 \pm 0.001$ and $\alpha = 0.82 \pm 0.01$ are likely reasonable. The resulting near collapse of $C_P(T)$ is shown in Fig. 5.7(b). Assuming the collapse is sufficiently indicative of a second order transition, the behaviour of the specific heat should be $C_{P_{\max}}(N) \sim N^{\alpha/(2-\alpha)}$, where we use once again the Josephson scaling relation. This curve is plotted in Fig. 5.7(a) and provides what appears to be a reasonable scaling for larger N.

While the scaling of $C_P(T; N)$ and $C_{P_{\max}}(N)$ suggest that the transition is second order in nature, the results are not very convincing. To help us further in distinguishing between first and second order, we plot for the same T, P and N the Binder cumulant

$$V_N = 1 - \frac{\langle h^4 \rangle_N}{3 \langle h^2 \rangle_N^2}, \tag{5.3}$$

in Fig. 5.8(a). The locations of the minima in V_N are the same as those of $C_{P_{\max}}$, while the values of the minima $V_{N_{\min}}$ determine the order of the transition. For a first order transition $V_{N_{\min}} \to c$ as $N \to \infty$, where $c < 2/3$ is a constant. For a second order transition, $V_{N_{\min}} = 2/3 - 1/N$ for large N [8]. In Fig. 5.8(b) we plot $V_{N_{\min}}$ as a function of $1/N$. The orange line in the inset shows the expected behaviour for second order behaviour. From the plots, we must conclude that the transition is not continuous, but rather first order, despite a value of c that is quite close to 2/3.

Thus, we appear to be at a crossroads, where scaling (somewhat) supports a

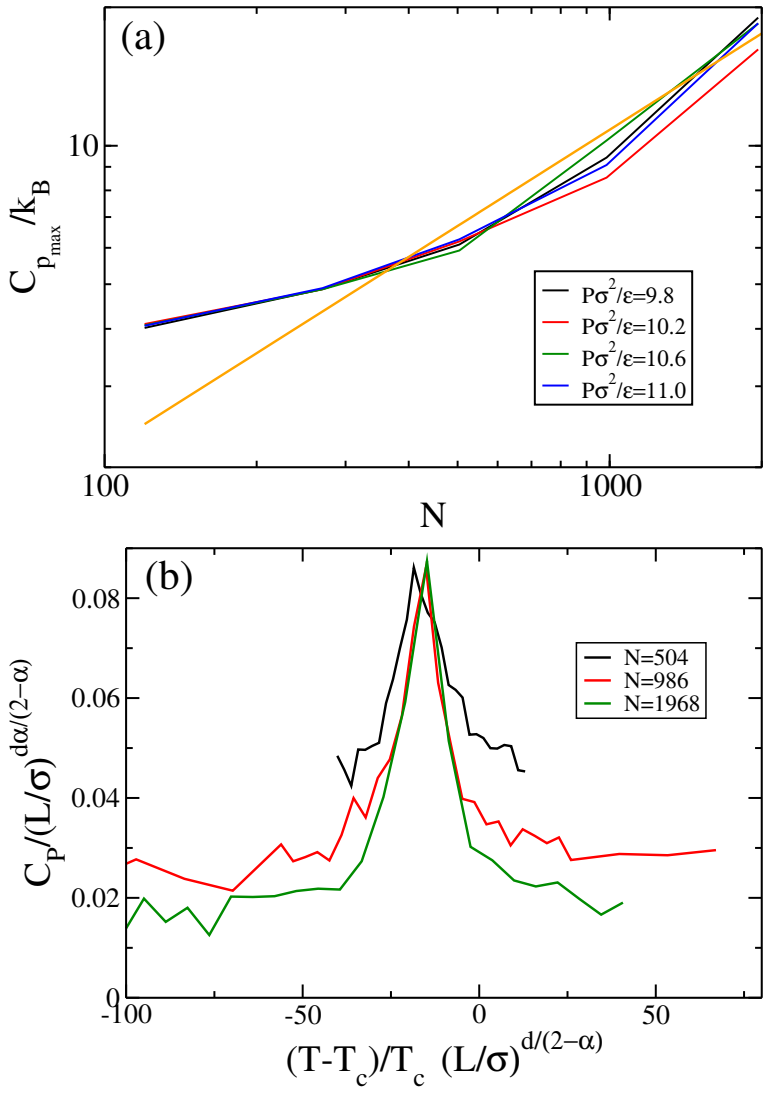

Figure 5.7: Tests for a second order transition. The heat capacity maxima $C_{P_{\max}}$ should scale with system size as a power law. Panel (a) shows that we have not entered into such a regime. However, panel (b) shows that C_P data for the largest systems collapse reasonably well onto a single scaling function, yielding a critical temperature of $T_c = 0.482$ and critical exponent $\alpha = 0.82$. The orange line in panel (a) shows the power-law behaviour of $C_{P_{\max}}$ expected from this value of α.

second-order transition and Binder cumulants point to a weakly first-order transition.

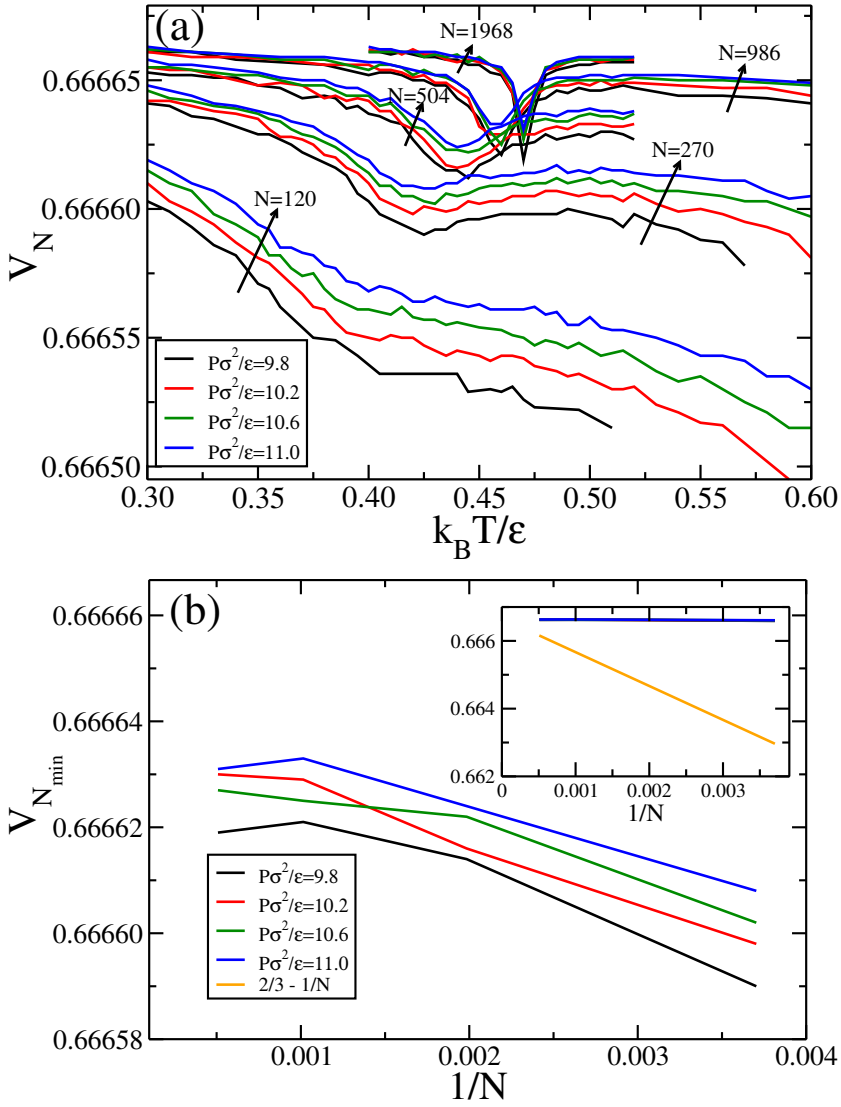

Figure 5.8: Binder cumulants. Panel (a) shows cumulants calculated according to Eq. 5.3 as a function of T along different isobars and for different system sizes, while in (b) we plot the minima of the cumulants. As system size increases, the minima approach a constant value close to, but significantly less than 2/3, thus indicating a first-order transition with a small latent heat. The orange line in the inset shows the behaviour expected of a continuous transition.

5.3.4 Solving the riddles partially

By simulating in the NPT ensemble with a fixed box geometry, we do not allow the box to accommodate changes in crystal symmetry very well. This may also suppress

fluctuations that would accompany a phase change to a different geometry. This enhances metastability of the phase matching the box geometry, and is responsible for the confounding behaviour we have just encountered. This, in fact, can be seen as a case of "clamping", where a first order transition in a crystal becomes second order once lattice deformations (long-wavelegth phonons) are removed from the Hamiltonian [9]. Here, by enforcing the symmetry of the high-T HDT phase on the simulation box, we suppress certain deformations.

In Fig. 5.9, we show potential energy "time" series of MC simulations at a set of T and P near the low-T to high-T transition, starting from the ideal HDT structure. We note that the system very quickly adjusts from an initial potential energy per particle of -1.5ϵ to the value $\approx -2.15\epsilon$ characteristic of high-T HDT, a change not even noticed in the time series. For these simulations, however, we implement anisotropic pressure control by allowing the box vectors to independently change length and also allowing the angle between box vectors to change. The abrupt jump in energy, in this case to a value just above -2.5ϵ, is the hallmark of a first order transition for our system size of $N = 986$ particles. Thus, we have clear evidence that the low-T to high-T transition is first order, and not particularly weak. This jump must occur in the region where the high-T phase is metastable, and so the actual transition temperature for this system size is quite reasonably near $k_BT/\epsilon = 0.5$, the temperature of the funny point.

While we have not confirmed the structure of the low-T form of HDT, we present a candidate structure in Fig. 5.10 that has potential energy per particle of -2.5ϵ. The new structure can be understood by considering a rectangular non-primitive unit cell containing two particles, as outlined in red in the figure. In the perfect HDT structure, both particles are equivalent, but in the low-T form, the central particle is shifted slightly to the left or right, parallel to the short side of the rectangle. The

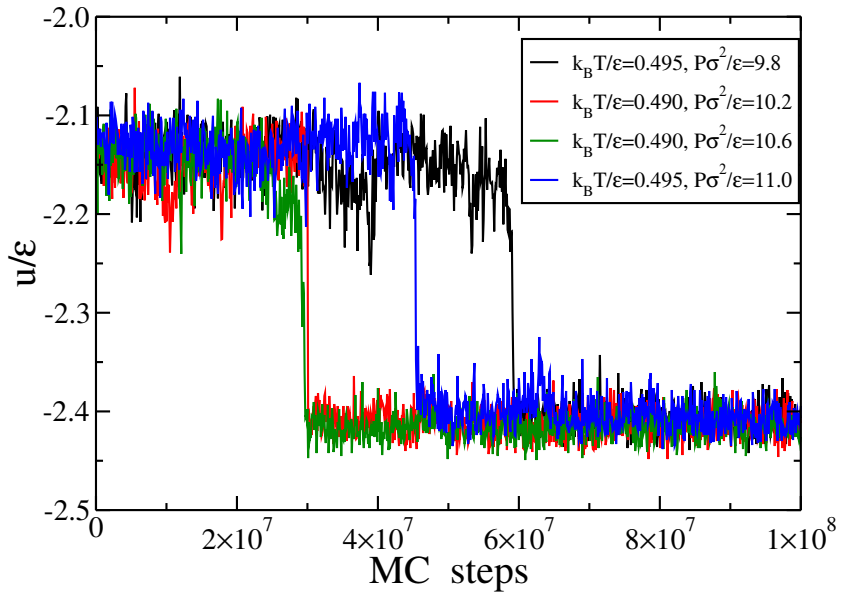

Figure 5.9: MC simulations with anisotropic pressure control showing potential energy per particle as a function of MC step. The abrupt change in the energy is a very clear indication of a first-order phase transition.

shift gains two bonds of energy $-\epsilon$, and also renders the two particles inequivalent. They both have the same bonding pattern, but "point" in opposite directions. The proposed structure fits in the same box as ideal HDT, so it is a bit perplexing that the transition is so affected by box flexibility. Perhaps for entropic reasons, the low-T form prefers a different ratio of box lengths, or a unit cell that is not rectangular. By simulating the proposed structure systematically at low T with a flexible box, we should be able to discern the geometry.

Simulating with a flexible box appears to solve the problem of determining the order of the low-T to high-T HDT transition, and moves the transition temperature to that of the funny point. However, we do not know why the low-T-high-T HDT transition line meeting or approaching the HDT-L line(s), presumably at a triple point, should result in the free energy barrier between either low-T HDT or high-T HDT and the liquid disappearing.

In Fig. 5.11 we plot the Gibbs free energy as a function of ρ for state points along

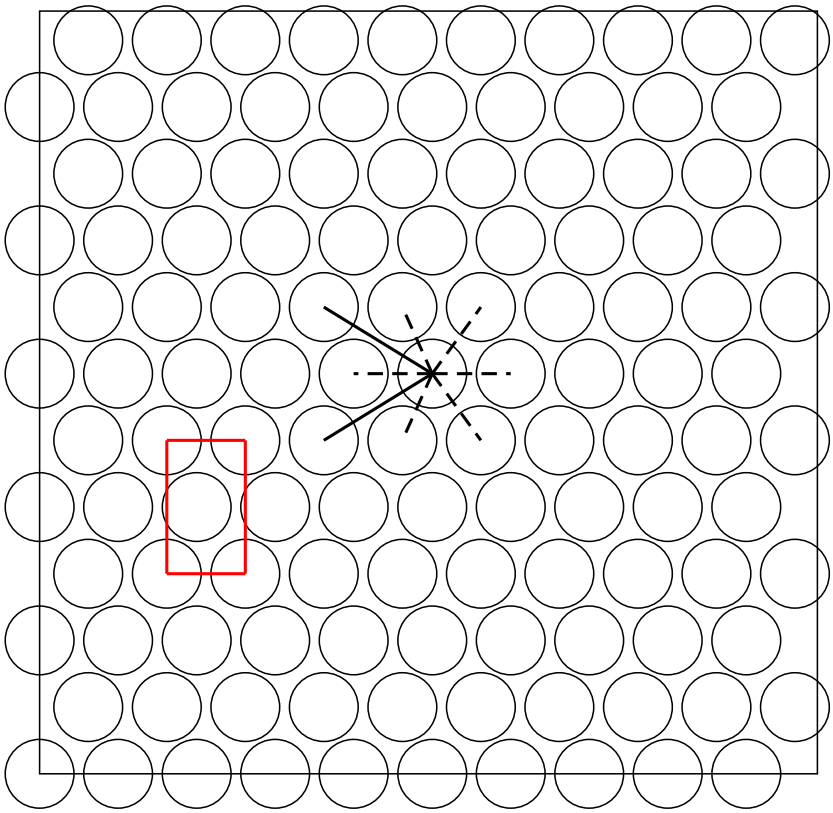

Figure 5.10: The candidate structure for the low-T HDT crystal that has potential energy per particle -2.5ϵ. A solid line indicates a bond with energy $-\epsilon$ and a dashed line a bond with energy $-\epsilon/2$. The red rectangle shows a non-primitive unit cell of this crystal, with the interior particle being shifted to one of the long edges. For the close-packed HDT structure, this interior particle is centred.

the HDT-L coexistence line. The coexistence condition we employ is that the free energy minima at high ρ (HDT) and low ρ (L) are the same. The inset shows that the height of the energy barrier separating the two minima practically vanishes at $k_BT/\epsilon = 0.50$. The free energy curves result from histograms of ρ obtained from umbrella sampling simulations, as described in Chapters 2 and 4, with $N = 986$. While the curves shown are for fixed box geometry NPT simulations, the results are robust to allowing box flexibility. For smaller system sizes (not shown), a small barrier is apparent, while for a larger system, $N = 2232$(not shown), the loss of the barrier is more clearly seen. The barrier vanishing implies that the interfacial tension between

L and (either) HDT vanishes.

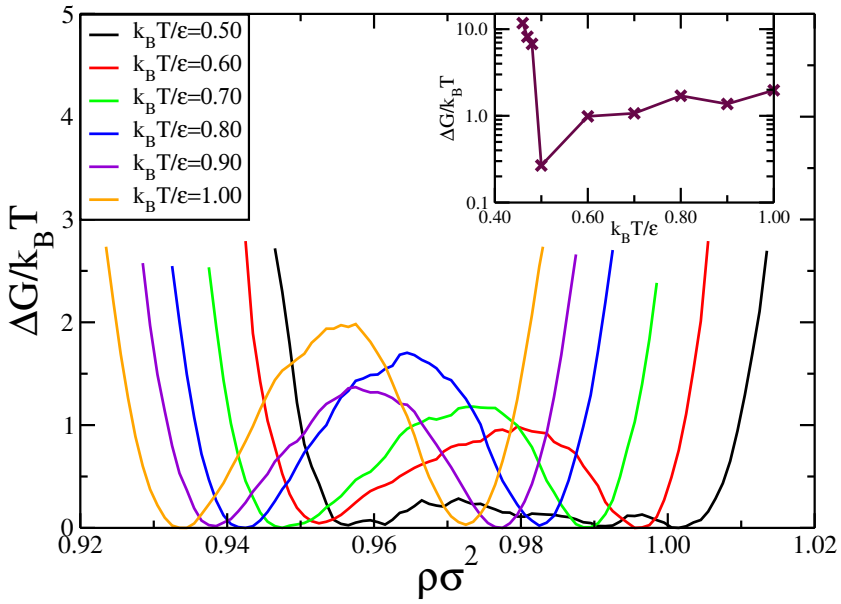

Figure 5.11: Conditional Gibbs free energy as a function of ρ obtained from umbrella sampling MC simulations for different temperatures along the HDT-L coexistence line. At $k_BT/\epsilon = 0.50$ a barrier is not distinguished from the noise; the barrier thus seems to vanish at this "funny point". The inset plots the barrier height for each temperature, showing a dramatic difference in behaviour above and below $k_BT/\epsilon = 0.50$.

As noted above, density is continuous across the low-T-high-T HDT transition. We see this directly and it also follows from the verticality of the transition line in the P-T plane. Thus, there seems to be no reason to assume large density fluctuations seen at the funny point on account of the two different HDT forms, assuming the low-T-high-T HDT transition remains first order on meeting the melting line. Perhaps the low-T-high-T HDT transition becomes second order prior to meeting the melting line.

Another possibility is that the hexatic phase appears in the vicinity of the funny point, allowing transitions to the liquid to not be first order. The riddle of the funny point is not solved.

5.4 Discussion and Conclusions

In Ch. 4 we vary the potential parameters ϵ_1, b and c and we find that b is the responsible parameter for increasing the range of P over which the inverse melting occurs. In particular, we focus on the model with ϵ_1 and c as in the original model and with $b = 1.46\sigma$. The bending of the inverse melting part of the S-L transition line has an impact on the topology of other coexistence lines, and as a result, the phase diagram in Fig. 5.1(b) for $b = 1.46\sigma$ is significantly different, at least at high P, from the original model (SSSW for $b = \sqrt{2}$) as shown in Fig. 5.1(a).

One novel feature in the $b = 1.46\sigma$ model is the disappearance of the HDT-S-L triple point. Instead of meeting, the HDT-L and S-L lines approach but then diverge from each other. This results in a "corridor" along $\rho\sigma^2 \approx 0.92$ for which, barring the appearance of other phases, the liquid appears to be the stable phase down to low T. Examining the structure of the liquid, we find two crystalline motifs. One of these crystals is a good candidate to occupy the low T portion of the phase diagram within this corridor. Free energy calculations remain to be done in order to determine coexistence conditions for this new phase.

In the course of calculating the new phase diagram, we noticed a "funny point" along the HDT-L line at which the free energy barrier separating the HDT crystal and the liquid disappears. This phenomenon is absent in the original model. This sort of behaviour is expected at a critical point, which is not expected to exist between a crystal and a liquid, at least in three dimensions. Further, we find no evidence of the expected increase in fluctuations within the liquid on approach to the funny point, as would be if it were a critical point.

Searching for an explanation within the HDT stability field, we find a transition between low and high T forms of HDT. We find that whether the NPT simulations are carried out with isotropic rescaling of particle coordinates or by allowing the

simulation box to change shape has a significant effect on the apparent order of the transition. Scaling relations and Binder cumulants are useful in pointing out the consequences arising from the additional constraints imposed on the system when using isotropic rescaling. We find a candidate structure for the low-T form of HDT, which can be obtained from the ideal HDT structure by slightly shifting alternate rows of particles in opposite directions in order to make energetic bonds with second neighbours. Further simulations are required to refine the structure of the low-T phase and to understand better why the pressure algorithm has a marked impact on the transition, given that the proposed structure also fits into the same simulation box as the high-T phase. Going back to the original model, we also find this transition within HDT.

The funny point remains a riddle to us. While both the original and $b = 1.46\sigma$ models possess the low-T to high-T HDT transition, only the $b = 1.46\sigma$ exhibits a vanishing of the free energy barrier along the HDT-L line. Possible explanations include the appearance of a hexatic phase (an examination of the orientational and translation correlation functions in the vicinity will help rule this out) and the changing of transition order from first to second along the low-T-high$T$ HDT transition prior to meeting the melting curve. A detailed examination of the compressibility, energy and/or density histograms at several system sizes are needed to help understand what is going on around the funny point.

Although the issue of isotropic versus anisotropic box scaling has an impact on studying the low-T to high-T HDT transition, generally speaking, for first order transitions where the symmetry of the coexisting phases is known, the pressure algorithm used for each phase should be such that it preserves the symmetry of that phase. It is more of a problem when encountering an unknown transition to an unknown phase, as in our case. Anisotropic scaling is useful in determining the symmetry of the new

phase. Once we have characterized the low-T HDT phase, we need to recalculate its melting curve and also its coexistence line with S (in the original model).

In principle, the inverse melting part of the S-L might be affected by an unknown transition that is obscured by enforcing a square simulation box. At the very least, we have calculated the S-L transition metastable to some unknown phase. However, the large EDMD simulations showing S melting and L crystallizing to S are large enough for new crystals to grow in a liquid environment unaffected by the box shape.

Bibliography

[1] F. Smallenburg and F. Sciortino, Nat. Phys. **9**, 1 (2013).

[2] A. Skibinsky, S. V. Buldyrev, A. Scala, S. Havlin, and H. E. Stanley, Phys. Rev. E **60**, 2664 (1999).

[3] Murty S. S. Challa, D. P. Landau, and K. Binder, Phys. Rev. B. **34**, 1841 (1986).

[4] K. Binder and D. W. Heermann, *Monte Carlo Simulation in Statistical Physics: An Introduction*, Springer-Verlag, Berlin, 1997.

[5] P. Pfeuty and G. Toulouse, *Introduction to the Renormalization Group and to Critical Phenomena*, Wiley, London, 1977.

[6] *Finite Size Scaling and Numerical Simulation of Statistical Systems* V. Privman ed., World Scientific, London, 1990.

[7] P. P. Chapagain and B. S. Gerstman, J. Chem. Phys. **119**, 1174 (2003).

[8] M. D. LeBlanc, M. L. Plumer, J. P. Whitehead, and B. W. Southern, Phys. Rev. B **88**, 094406 (2013).

[9] A. I. Larkin and S. A. Pikin, Zh. Eksp. Teor. Fiz. **56**, 1664 (1969).

Chapter 6

Summary and Future Work

In this thesis, I present the results of our exploration of the phase behaviour of a system of disks interacting through a potential that was previously shown to exhibit anomalous liquid properties at low density, and the construction of which was motivated by creating minimal models that exhibit single-component liquid-liquid phase separation. Given these origins of the potential, it is perhaps not surprising that its behaviour at higher pressures yields some surprises.

The S (square) crystal proves to be the most interesting of characters in the cast of phases that include the gas, the liquid, a low density triangular crystal, two high density triangular phases (although the low T phase does not seem to possess hexagonal symmetry), and four new crystals perfunctorily named A, Z, I and O. The rather open structure of S allows for a large vibrational entropy and hence we encounter a case where the entropy of the crystal is higher than that of the liquid, giving rise to the phenomenon of inverse melting.

In studying the numerous phase transitions in the system, we employ:

- NVT and NPT MC simulations for obtaining equations of state for use in thermodynamic integration required to obtain free energy changes between state

points and to test basic phase stability.

- umbrella sampling MC, particularly useful for determining histograms of fluctuations of thermodynamic quantities, in our case ρ.
- the Frenkel-Ladd method for determining absolute free energies of crystals.
- the Gibbs-ensemble method along with calculating the pressure using virtual volume changes to determine the L-G line and critical point.
- Gibbs-Duhem integration for tracing coexistence curves.
- Hamiltonian Gibbs-Duhem integration for obtaining changes in coexistence conditions given changes to a potential.
- EDMD simulations as an independent check on the MC-based results.
- various measures of order and its range including $g(r)$, $S(q)$, $G_{4,6}(r)$ and $G_{\vec{g}}(r)$, as well as Steinhardt bond order parameters to identify particles locally as being crystal-like or liquid-like.
- finite-size scaling including Binder cumulants to help discern the order of transitions.

The methods we use in calculating the phase diagram in Ch. 3 require a degree of metastability in order to be applicable. Indeed, with the exception of the HDT-L line above $k_BT/\epsilon = 0.46$, where the free energy barrier between crystal and liquid is low, all transitions are sufficiently strongly first order. Despite this, the degree of metastability is very small for some of the transitions, and the chemical potential difference between metastable and stable phases is very small compared to three dimensional systems. Given this, it would be straightforward to achieve a reasonably accurate phase diagram by simply carrying out many simple NPT simulations and

observing the end phase of each run (as we did in checking our free energy-based transition lines). However, it is worthwhile pointing out that with such an approach, we would have likely missed the initially very subtle effect of inverse melting. It was the precise and rigorous determination of coexistence conditions that allowed us to discern inverse melting of S.

In Ch. 4, we expand the range of inverse melting by first varying the three independent parameters of the potential and using Hamiltonian Gibbs-Duhem integration for a small portion of the S-L curve to see the effect of the variations on the extent of inverse melting. We find that the parameter b, the extent of the intrawell shoulder has the greatest impact on inverse melting and the effect seems to be maximized near $b = 1.5\sigma$. As a case study of a system with pronounced inverse melting, we focus on the model with $b = 1.46\sigma$.

For the $b = 1.46\sigma$ model, we recalculate the whole S-L melting curve and perform various tests. We determine the surface tension through density histogram methods between S and L at coexistence conditions despite the interface being rather diffuse. This surface tension calculation confirms both the accuracy of the determination of the coexistence conditions and the first-order nature of the transition. We carry out molecular dynamics simulations to directly see inverse melting, both by melting the S crystal upon lowering T and freezing the liquid upon raising T. We do not find evidence for a hexatic phase or a quasicrystal phase in the vicinity of the inverse melting line.

Having the surface tension, at least at one particular coexistence pressure, as well as the tools required for calculating the chemical potential difference between the S and L along the corresponding isobar, we are in an excellent position to carry out an assessment of how well Classical Nucleation Theory (CNT) fares in describing the crystallization process of our 2D system. CNT predicts the rate of nucleation given

the surface tension and the chemical potential difference (and diffusion coefficient). It would be interesting to see in what regime the predictions of CNT hold, given the diffuse nature of the interface between S and L.

In using the translational correlation function $G_{\vec{g}}(r)$ to identify phases as being crystalline, hexatic or liquid, we find that the previously reported power-law decay of peaks in this function, when there is no other indication of quasi-long-range order in the system, is an artefact of the mathematical definition of $G_{\vec{g}}(r)$: for a system with orientationally uncorrelated local environments, $G_{\vec{g}}(r)$ reduces to a Bessel function, the peaks of which decay as a power law. This Bessel-law contribution should be subtracted in order to reveal the true extent of translational correlation.

In pursuing the HDT-L line for the $b = 1.46\sigma$ model in Ch. 5, we find a narrow density range for which the liquid remains particularly stable at lower T as the HDT-S-L triple point vanishes. Examining the structure of the liquid reveals a potential crystal that is well suited to this density. We also find that the free energy barrier between HDT and L disappears at a point along the HDT-L coexistence curve. While this funny point is likely related to a transition we find between two subforms of HDT, we must use the various techniques at our disposal to very clearly show what precisely is occurring as the low-T-to-high-T HDT line meets the HDT-L melting line. We need to do this also for the original parameters of the SSSW model, for which there is also a low-T-to-high-T HDT transition, but where the free energy barrier between HDT and L remains finite and hence we expect a normal triple point.

We wonder to what extent the rich phase behaviour of the SSSW model can be reproduced in other model or experimental systems, and to what extent dimensionality plays a role. A step in this direction is to see whether inverse melting survives in a continuous version of the potential. There is some hope. Recently, it was shown that a continuous version of the SSSW potential retains the second (liquid-liquid) critical

point [1] that is obscured by crystallization near the LDT-S-L triple point in the original SSSW model. It would be interesting to see how the continuous model behaves at higher pressures and whether a similar optimization of the continuous model parameters can be accomplished to produce inverse melting. Conversely, perhaps the SSSW potential parameters can be adjusted to lower the LDT-S-L triple point so that, with crystallization sufficiently suppressed, the critical point emerges into the stable liquid regime.

Interactions within lipid membrane systems have been modelled with potentials similar to the SSSW model used in this thesis [2]. If inverse melting can indeed occur in continuous analogs of the SSSW potential, then it may be possible to find or synthesize lipids with the effective interaction required to produce inverse melting.

In summary, this thesis is another example of how a seemingly straightforward goal, in our case wishing to determine the phase diagram of a fairly innocuous model of interaction between disks, can yield unexpected results. We hope that you agree with us that the SSSW model is a simple potential full of complexities.

Bibliography

[1] T. Urbic, Phys. Rev. E **88**, 062303 (2013).

[2] M. Nielsen, L. Miao, J. H. Ipsen, M. J. Zuckermann, and O. G. Mouritsen, Phys. Rev. E **59**, 5790 (1999).